Layering transitions, disordered flat phases, reconstruction and roughening

Thesis by

Anoop Prasad

In Partial Fulfillment of the Requirements
for the Degree of
Doctor of Philosophy

California Institute of Technology
Pasadena, California

1997
(Submitted May 12, 1997)

Acknowledgements

Above all else I have valued my parents' love, support and guidance all these years. The most eloquent words would be completely inadequate to express my feelings for them and for my sister; I won't even try.

I owe a great debt of gratitude to my advisor, Peter Weichman. Peter's keen intuition coupled with his technical prowess made his advice invaluable. I have great respect for his unwavering enthusiasm and good humor even in the midst of trying circumstances.

Weekly meetings with David Goodstein, Bill Weber and Alexa Harter over the past two years have been enjoyable and instructive. Most of my knowledge of experimental surface and helium physics has been derived from discussions at these meetings.

Charlie Peck's marvelous abilities as a teacher transmuted an ordinarily leaden course on classical electrodynamics into something priceless—my best course at Caltech. Mike Cross helped me to wade through Fetter and Walecka during my first summer here; the material came in handy on several occasions.

I am grateful to Marcel den Nijs for helpful suggestions on a paper and for stimulating conversations during last year's March Meeting.

Pat Stevens' efficiency and good nature made life at (and travel away from) Sloan Annex very pleasant and completely trouble free.

I'd also like to thank several close friends: Ranjan (with whom I shared a similar background, an advisor, research interests, and one tiny office) for having suffered a severe overdose of my company for five years without complaining. Ravi for having suffered four times that length of time. Goutam and Sulekha for conjuring up delicious meals so often, even when I turned up unexpectedly (as I invariably did). Glenn and Kent for making the first two years of coursework and assignments more bearable, and the triumvirate consisting of Glenn, Sergey and Yuri for many pleasant evenings filled with food and conversation and for, among other things, demonstrating quite spectacularly how *not* to open a bottle of wine.

Many more people contributed in some small way to make life interesting: the hapless undergrads in Ph2 who had to listen to my views on every conceivable subject, numerous raquetball and table tennis opponents, an eccentric herbalist (who provoked more laughter than he would ever know), ... the list goes on. But since I don't think that any of these people are going to read my thesis, I'll stop here!

Abstract

We study in light of recent ellipsometry, vapor pressure isotherm and specific heat measurements on the thermodynamics of adsorbed films on graphite, the connection between the layering phase diagrams of thin films on periodic substrates and the thermodynamics of the solid-vapor interface of a semi-infinite crystal. The latter is the limit of the former when the film becomes infinitely thick, and we are interested in connecting this limiting behavior to the thermodynamics of films of finite thickness. We argue that the concepts of surface roughening, preroughening and reconstruction provide a quantitatively useful framework within which to discuss this connection. Through general renormalization group arguments and, in more detail, through a self-consistent mean field treatment that explicitly accounts for all relevant phases, we show that the same types of interactions that lead to these different surface phases lead also to the reentrant layering transitions seen in the recent experiments. By appropriate tuning of the mean-field parameters we can semi-quantitatively reconstruct all the observed experimental phase diagrams. It turns out that certain experimental phase diagrams with "zippers" require that the preroughening transition become first order. Our renormalization group arguments predict such behavior in certain parameter ranges. In addition, for different parameters we predict the existence of an, as yet unobserved, θDOF phase with spontaneously broken particle-hole symmetry and continuously varying surface height with an accompanying intermeshing layering phase diagram and we describe a microscopic model which shows such behavior. The underlying lattice in the experiments is triangular, and this actually *enhances* the stability of the disordered flat phase and the corresponding reentrant layering transitions in the films.

Contents

List of Figures

Chapter 1 Introduction

1.1 Surface critical phenomena

The study of interfaces between two different thermodynamic phases has yielded a remarkable variety of interesting phenomena. Some of the most fascinating behavior occurs at the interface between a bulk semi-infinite crystal and its vapor. When the temperature is below the bulk triple point, T_t (the temperature at which the crystal melts in the presence of the vapor), the thermodynamics of the bulk crystal is smooth and nonsingular. The crystal surface, on the other hand, can exist in many different phases. The simplest phase is the *flat phase* in which the surface looks essentially like a bulk crystalline plane. This phase is characterized by the existence of a positive surface step free energy, f_s, which discourages the formation of plateaux or depressions in the surface. Although a finite density of such imperfections will always be entropically favored, the probability of their occurrence will decrease exponentially with their size. Furthermore, if the number of particles is such that the surface layer is *incomplete*, phase separation will occur and a single one-dimensional interface will separate two macroscopic flat regions with unit height difference between them.

The flat phase is a special case of more general *reconstructed* phases. Here the surface layer, though only partially complete, nevertheless forms a periodic structure, commensurate with the underlying bulk crystal lattice plane, but with a larger unit cell, and a corresponding rational filling fraction, θ_R. There are analogous step free energies, $f_{s,R}$, which discourage configurations of particles which deviate from perfect periodicity. If the number of particles is such that the overall filling fraction, θ, of the surface layer deviates from θ_R, the surface will again phase separate with a single one-dimensional interface separating two (possibly different) reconstructed phases. In the event that the two phases are different, coexistence requires that the surface free energies must match.

Very different in character from the flat and reconstructed phases is the *rough phase*. At and above the *roughening temperature*, $T_r < T_t$, the flat phase step free energy vanishes and it becomes entropically favorable for the surface to wander. To describe this quantitatively, let $\mathbf{r} = n_1\mathbf{a} + n_2\mathbf{b}$, where n_1 and n_2 are integers, and $\mathbf{a}$ and $\mathbf{b}$ are primitive vectors, label the lattice points in the underlying crystal plane. Let $h(\mathbf{r})$ be the (integer) height of the surface above the lattice point $\mathbf{r}$. Then, at the roughening temperature, the variance of $h(\mathbf{r})$ diverges. More specifically, at and above T_r, the height-height correlation function,

$$G(\mathbf{r}-\mathbf{r}') \equiv \frac{1}{2}\langle[h(\mathbf{r}) - h(\mathbf{r}')]^2\rangle, \tag{1.1}$$

increases logarithmically with separation:

$$G(\mathbf{r}) \approx \frac{1}{4\pi K_R(T)} ln(r/a_0),\ r \equiv |\mathbf{r}| \to \infty,\ T_r < T < T_t, \tag{1.2}$$

where $a_0 = |\mathbf{a}|$, say, is a microscopic length scale, and $K_R(T)$ may be thought of as a renormalized surface tilt modulus. In the flat and reconstructed phases, the variance, $\langle[h(\mathbf{r}) - \langle h(\mathbf{r})\rangle]^2\rangle$, is finite and equal to the large r limit of $G(\mathbf{r})$.

A useful way to visualize surface structure is the following "directed line" representation (see Fig. 1.1): The presence of a difference in height between two neighboring sites on the surface is shown by a line running between the two sites (this corresponds to the presence of a step). An arrow is drawn on each line segment so that, looking along the arrow, the right side is a region with height one unit greater that the left side. There is a step energy cost J per unit length of the line. Here and henceforth we impose the restriction that nearest neighbor sites can differ in height by at most one atomic step; this condition is actually quite well obeyed in most experimental systems. With this representation in mind the reason for roughening is clear: At low temperatures the entropy is not very effective in reducing the free energy $f_s = j - Ts$ per unit length of the surface step. The free energy is dominated by the step energy J and consequently there are only a very small number of thermally activated steps

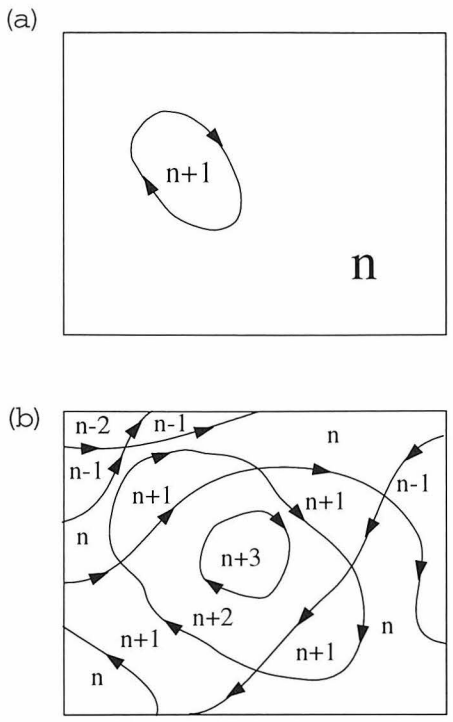

Figure 1.1: Sample surface configurations. (a) Flat phase with one thermally excited island. (b) Rough phase with a proliferation of steps.

and the surface is flat (Fig. 1.1(a)). At higher temperatures the step wandering entropy begins to play an important role. At and above the roughening temperature the entropy contribution drives f_s to zero and steps proliferate as shown Fig. 1.1(b).

The transition into the rough phase is in the universality class of the Kosterlitz-Thouless transition [22], which also describes the low temperature magnetic ordering in the two-dimensional XY-model and the superfluid ordering in thin ^4He films. A consequence of this is that *right at* the roughening temperature, $T = T_r$, the renormalized tilt modulus has the universal value $K_R(T_r) = \frac{\pi}{2}$. The value of K_R jumps discontinuously to infinity below T_r, and decreases monotonically with T above T_r. In the XY-model the heights, $h(\mathbf{r})$, appear in a dual representation of the original two-component spin model, and $1/k_B T K_R(T)$ is proportional to the spin stiffness (or superfluid density), Υ. There is an inverse relation, $T \propto 1/T_{XY}$, between the temperatures in the two models since the flat phase, with $K_R(T) \equiv \infty$, corresponds to the disordered phase of the magnet (or superfluid), with $\Upsilon \equiv 0$ [1].

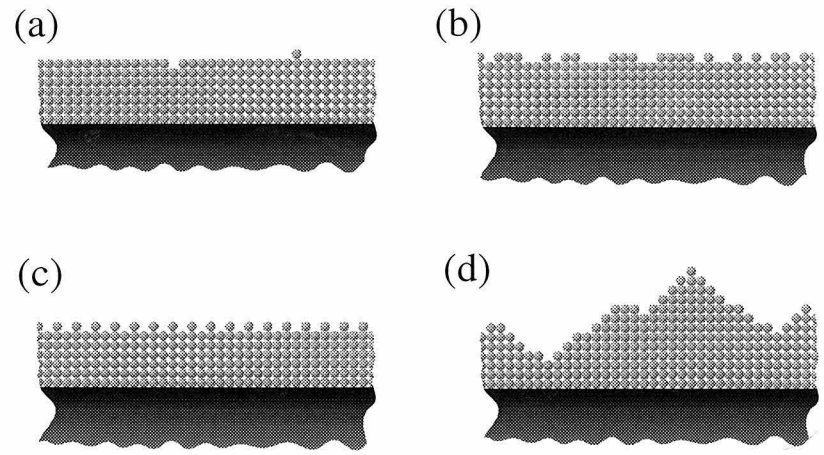

Figure 1.2: Caricatures of the surface phases discussed here: (a) Flat (b) DOF (c) Reconstructed (d) Rough.

It turns out that there is yet another class of possible surface phases that may occur. These are the *disordered flat* (DOF) *phases* [2, 3, 4, 5] which may be thought of as intermediate between the reconstructed and rough phases. As an example, consider the (100) surface of a cubic crystal, and suppose that the atomic interactions are such that at low temperatures a kind of antiferromagnetic reconstructed phase with a checkerboard pattern ($\theta_R = \frac{1}{2}$) is stabilized. Now, as the temperature rises, this phase may proceed *directly* through a roughening transition, analogous to that for the flat phase (but with a form of long ranged antiferromagnetic order persisting). However, it is also possible, if the checkerboard pattern is only weakly stable, for the system to undergo an Ising transition which destroys long range antiferromagnetic order *without* roughening the surface. The surface layer is then basically a two-dimensional lattice gas at half filling. This phase is called the *disordered flat phase*. Raising the temperature further finally roughens the surface completely. It is also possible to enter the DOF phase directly from the flat phase [2, 3, 4, 5]. The transition is driven by the entropy gain entailed by a disordered surface, and can occur even if the energetics favors the flat phase. Note that this transition causes a *discontinuous* change in the occupancy of the surface layer. If the total number of particles is fixed, this means that the surface must phase separate into two disordered flat phases, one with an extra half layer of atoms, the other with a half layer of "holes." The phase transition,

at a temperature $T_{pr} < T_r$, is called *preroughening* and lies in a different universality class from that of all the other transitions discussed so far. For example, the specific heat exponent, α, can take any value between the Kosterlitz-Thouless value, $\alpha = -\infty$, and the four-state Potts value, $\alpha = \frac{2}{3}$, depending upon the system parameters and, in particular, upon the precise strength of the tendency toward reconstruction [4] (the more nearly stable the reconstructed phase, the larger the value of α). It turns out [57] as discussed later in this thesis that the preroughening transition can even be driven first order, a possibility that was missed in earlier studies [2, 3, 4, 5].

The disordering of the checkerboard phase is only one example of a DOF phase. In principle, corresponding to any reconstructed phase is a disordered flat phase with the same coverage, θ_R, separated from it by an Ising- (or perhaps Potts-) type phase transition. However, we shall see that DOF phases may also exist even without a corresponding reconstructed phase ever being stable. This is crucial for the triangular lattice substrates relevant to the experiments, where the analogue of the $\theta_R = \frac{1}{2}$ "antiferromagnetic" checkerboard reconstructed phase is frustrated and does not exist. Nevertheless, as we shall see, a $\theta = \frac{1}{2}$ disordered flat phase does exist, and is even more stable than its square lattice counterpart! In fact, there are conditions [57] under which a disordered flat phase with *continuously varying* surface coverage, $\theta(T)$, can exist. This θDOF *phase* was first proposed by den Nijs [4] as a consequence of particle-hole symmetry breaking corner interactions. However, we find [57] that the same physics that gives rise to the first order preroughening mentioned above can, for different parameters, lead to a *spontaneous* breaking of particle-hole symmetry and a corresponding θDOF phase in a completely particle-hole symmetric model. Whether or not a given system will exhibit a disordered flat phase depends upon the detailed atomic interactions. It is clear that a rather sensitive balance of nearest and further neighbor interactions may be required [2, 3, 4, 5]. A two component "alloy" (discussed in section 4.8) seems to be required for the appearance of θDOF behavior.

The preceding section provides an introduction to the main phenomena discussed in this thesis. Before proceeding further it is useful to take a step back and review the field a little more systematically. Important experimental work is discussed in

the next section and theory is discussed in section 1.3.

1.2 Experiment

Historically experimental work was directed mostly towards understanding monolayer physics. Monolayer physics is very rich and there was (and still is) much to be understood about films which are at most one atomic layer in thickness. Despite the beautiful KTNHY theory [32, 33], 2D melting is not a fully solved problem, in part because of strong translational symmetry breaking due to the presence of a corrugated substrate potential. Moreover, there are a wide variety of registered and incommensurate phases and transitions between these phases. These phenomena have been explored experimentally using techniques such as heat capacity measurements, x-ray scattering, vapor pressure isotherms, neutron diffraction and low energy electron diffraction [43, 44, 45, 46, 47, 48, 49]. The focus of this work will, however, be on multilayer phenomena. The celebrated experiments of Thomy and Duval [39, 40] in 1969 were among the earliest ones in which multilayer films were studied. They observed layer by layer growth of adsorbate films on exfoliated graphite (commercially known as Grafoam) substrates, mapping out high resolution isotherms for the growth of xenon and krypton films. Since then there have been numerous experiments to probe the properties of thick films. We will only touch on a few of these that are relevant to our analysis. Various reviews (e.g. [42] and references therein) contain further details.

Youn, Meng and Hess [41, 42] undertook ellipsometry studies of xenon, argon and krypton on highly oriented pyrolytic graphite. (Ellipsometry is an optical technique which probes the film thickness by measuring the ratio ρ of the reflection coefficients for s- and p-polarized light and the reflective phase delay Δ between the two polarizations. By finding the phase delay Δ_o due to the bare substrate and the shifted delay Δ_1 with the adsorbed film, the film thickness can be accurately measured.) Youn et al. measured the evolution of film thickness with vapor pressure for several isotherms and their results were striking. There was very clear evidence for reentrant

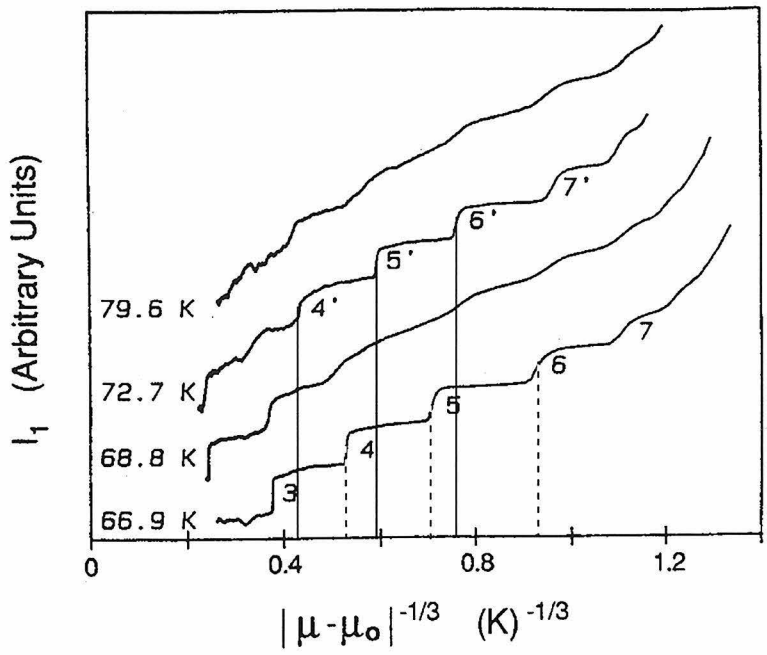

Figure 1.3: Ellipsometry isotherms for Argon on Graphite. I_1 is an ellipsometric output signal which is related to the adsorbate thickness. The interleaving of the layering chemical potentials of the low and high temperature isotherms is evident. From H. S. Youn and G. B. Hess, Phys. Rev. Lett. **64**, 918 (1990).

layering. One of their plots, for argon on graphite is shown in Fig. 1.3. From this figure it is seen that at low temperatures (66.9 K) there are sharp steps from one film thickness to the next. As the temperature is raised, the steps disappear but at yet higher temperature (72.7 K) there is reentrance: The steps reappear but they occur between half integer average-heights. Finally, at the highest temperatures (79.6 K) the film is in the rough phase and the growth is continuous once again.

Goodstein's group at Caltech then carried out several interesting experiments [52, 53, 54, 55, 56] on the layer by layer growth of rare gas adsorbates on graphite foam. Using a custom made adiabatic scanning ratio calorimeter they were able obtain a detailed picture of the phase diagrams of krypton and argon on graphite from the second layer upwards. (One of their aims was to probe the system in regimes which were complimentary to both the ellipsomery data [41, 42] which studied thick films and x-ray studies [51] which probed thin film properties.) The Caltech group found

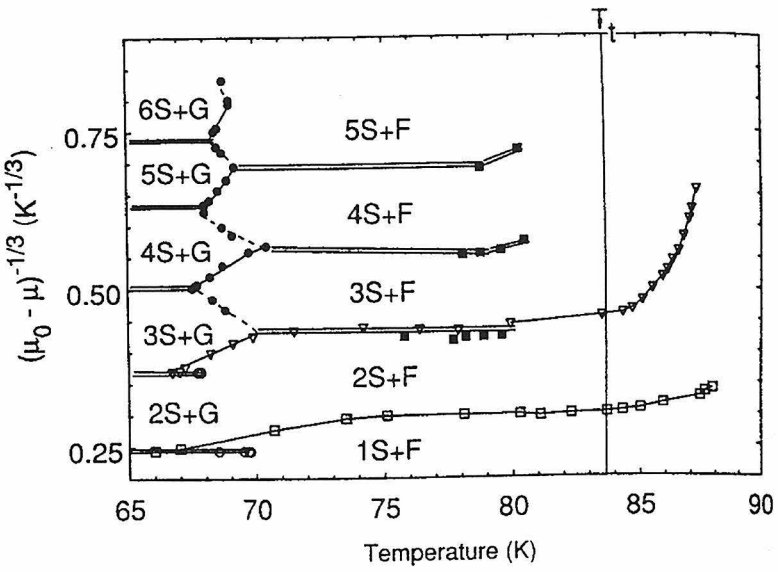

Figure 1.4: Phase diagram for Argon on Graphite, From Day et al. [52]. The variable plotted on the vertical axis is related to the pressure of the vapor.

evidence for several additional phase transitions (including registry transitions, and individual layer melting) not seen in the ellipsometry data. Substrate induced freezing was observed for films of thickness greater than four layers in agreement with [59]. The second layer was found to act as an independent 2D system but with very different characteristics from the monolayer. The presence of reentrant layering was confirmed. Moreover, it was found that the low temperature layering lines appear to connect to the higher temperature reentrant transitions through a line of heat capacity peaks.

Another important result was the discovery by Lysek et al. [55] that pores and wedges in the graphite substrate make capillary condensation an extremely important consideration even at fairly modes coverage. In fact some of the conclusions of [59] and other experiments were called into question because capillary condensation dominates layer-by-layer growth for films above about four atomic layers thick. Weber and Goodstein [58] are presently involved in experiments which will lead to a better understanding of these problems and how to circumvent them.

Finally we mention a recent x-ray reflection study of argon on MgO by Rieutord et al. [60]. This technique (on films adsorbed on single-crystal surfaces) yields information about both the quantity of adsorbate on the surface and about the struc-

tural state of the top layer. There appears to be evidence of preroughening in this system too; moreover the experiment yields confirming evidence that the half-filled disordered flat layer is in a liquid phase.

1.3 Theory

Equilibrium crystal shapes have been studied for a long time. The first important theoretical work was a famous paper by Wulff in 1901 [6]. Wulff found equilibrium macroscopic crystal shapes by minimizing the solid-vapor interfacial energy $F(T,\omega) = \int_{\partial\omega} dS f(\hat{\mathbf{m}},T)$ with respect to the shape, ω, of the crystal and subject to the constraint the the volume $V(\omega) = \int_{\omega} d\omega$ remains constant. Here $f(\hat{\mathbf{m}},T)$ is the interfacial free energy per unit area when the surface is oriented in a direction $\hat{\mathbf{m}}$ with respect to some fixed axis. Wulff constructed an explicit method (now called the Wulff construction) to solve this problem (see Fig. 1.5) for a given $f(\hat{\mathbf{m}},T)$. This method was later generalized [8] and details can be now found in standard textbooks [9]. The essential result found by Wulff is that only certain highly symmetric directions, $\hat{\mathbf{m}}$, at which f has corners will appear as facets on an equilibrium crystal surface. Finding the function $f(\hat{\mathbf{m}},T)$, however, is far from trivial and requires a detailed microscopic calculation. Our concern in this thesis is not with the theoretical calculation of f but with with the equilibrium *surface* structure on an equilibrium facet, $\hat{\mathbf{m}}$, determined by a given f.

The solid on solid (SOS) models are very useful in the study of thermal roughening and other surface phase transitions, given a choice of $\hat{\mathbf{m}}$ [10, 11, 12]. The roughening transition for such faces occurs when $f(\hat{\mathbf{m}},T) \to 0$. If $\hat{\mathbf{m}}$ is not a symmetry direction for the crystal but is only tipped slightly from a symmetry direction (a crystal can be made to grow in such a direction by externally applied boundary conditions) then there will be a finite number of steps on the surface even in the ground state (the surface will be a *vicinal* surface as shown in Fig. 1.6) and the ordered phase is one with parallel steps, a *striped* phase. When the temperature of this system is increased, the stripes disorder as described by Pokrovsky and Talapov and others [16, 17, 18]. Here

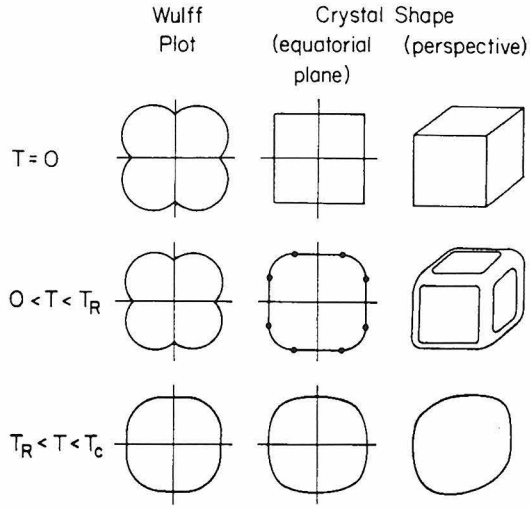

Figure 1.5: The Wulff Construction: The first column shows polar plots of $f(\hat{\mathbf{m}}, T)$ for a simple cubic crystal at three different temperatures. T_R is the roughening temperature, above which $f(\hat{\mathbf{m}}, T)$ is completely analytic. The second and third columns show the corresponding crystal shapes. (From C. Rottman and M. Wortis, Phys. Rep. **103**, 59 (1984).)

we will restrict our considerations to directions $\hat{\mathbf{m}}$ which are symmetry directions of the crystal.

Some of the earliest work on the statistical mechanics of surfaces was done by Burton, Cabrera and Frank [13, 14]. They realized the importance of steps and topological defects like screw dislocations as nuclei for crystal growth. In addition, using a two state Ising model to model the surface physics, they speculated that the crystal surface at high temperatures does not merely have isolated thermally induced steps with an exponentially low density as had been earlier thought [15] but that there is actually a phase transition to a completely disordered phase, similar to the DOF phase discussed earlier.

The original belief of Burton et al. and others [14, 19] that the transition was in the Ising universality class was subsequently found to be incorrect. Monte Carlo (MC) simulations [20] showed that near the disordering temperature an effective two layer approach is inadequate: Even if the MC simulation starts out with a flat surface close to the disordering temperature, as the simulation proceeds large clusters form and smaller clusters form on the large clusters and the concept of a reference height

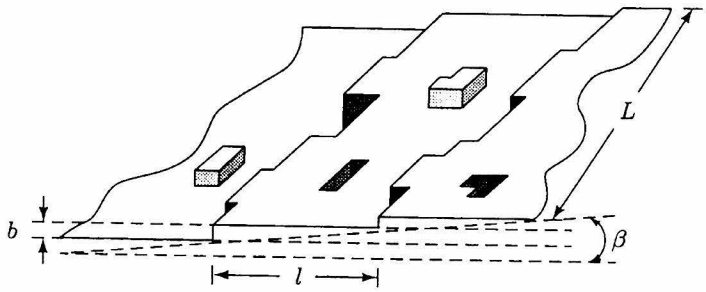

Figure 1.6: Striped phase at finite temperature. β is the angle of deviation from a symmetry direction. From P. Chaikin and T. Lubensky, *Principles of Condensed Matter Physics*, Cambridge University Press, New York (1995).

becomes meaningless. This led Chui and Weeks [21] to introduce a discrete Gaussian model with Hamiltonian

$$\mathcal{H}_{DG} = \frac{J}{2}\sum_{j,\delta}(h_j - h_{j+\delta})^2 \tag{1.3}$$

where h_j denotes the surface height at site j, and δ indexes nearest neighbors. At a given site the height variable can take any integer value. They showed that this model is exactly mappable to the neutral 2D lattice coulomb gas which had already been shown to be in a very different universality class by Kosterlitz and Thouless [22, 23]. Soon after this work, Jose et al. [1] showed quite generally that any nearest neighbor SOS model can be mapped onto a planar XY-type model by a duality transformation. This mapping (which can easily be generalized to include longer range interactions) has been of great importance in unifying the description of systems which had earlier seemed quite unrelated.

The **six-vertex** (6V) models constitute another extremely useful class of models (for a variety of systems including ice [24] hence the alternate name *ice-type models*) for surface reconstruction and roughening. 6V models are defined on a square lattice with the one additional condition that there *always* has to be a height difference between nearest neighbors. Hence the lines denoting the steps form the bonds of a regular lattice. In the ice-type models a certain energy is assigned to each vertex (i.e. each intersection of step-lines) rather than to each line segment. There are exactly 6 possible different vertex configurations (Fig. 1.7). In the most general model each

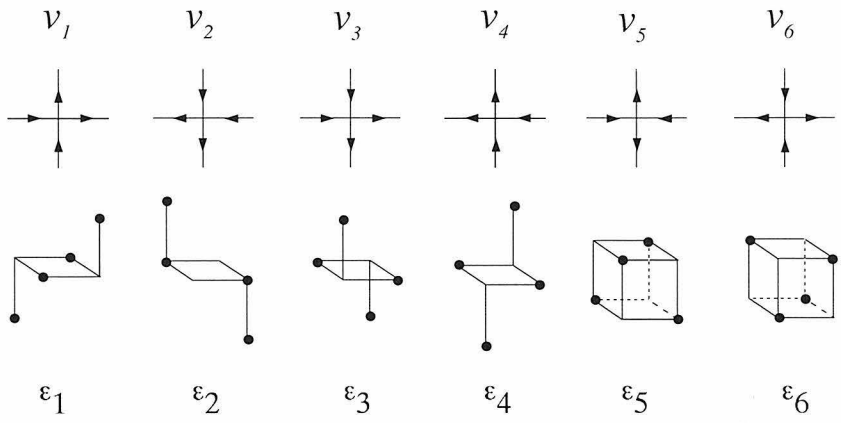

Figure 1.7: The six vertex model. Shown below each vertex is a schematic of the corresponding surface configuration.

vertex could have a different energy (except that symmetry considerations require that $\epsilon_5 = \epsilon_6$ for a system with periodic boundary conditions). For simplicity (and because there are generally certain symmetries is real systems) various additional symmetries are imposed on the ϵ_i. For example in one early 6V model (suggested by F. Rys in 1963 [25]) the choice

$$\epsilon_1 = \epsilon_2 = \epsilon_3 = \epsilon_4 > 0 \quad \text{and} \quad \epsilon_5 = \epsilon_6 = 0 \tag{1.4}$$

was made. This choice of energies defines the **F-model**. Clearly the ground state of this model will consist exclusively of vertices v_5 and v_6 and has a twofold degenerate checkerboard structure (one of which is shown in Fig. 1.8(b)). The F-model was solved exactly by Lieb [26, 27, 28] and a more general model with $\epsilon_1 = \epsilon_2$, $\epsilon_3 = \epsilon_4$, and $\epsilon_5 = \epsilon_6$ was solved subsequently [29, 30]. The phase diagram for this model is shown in Fig. 1.8. Here $a = e^{-\epsilon_1/T}$, $b = e^{-\epsilon_3/T}$, and $c = e^{-\epsilon_5/T}$. Regions I and II correspond to surface phases where almost all of the vertices are only of type 1 and 2 or of type 3 and 4. Thus in these phases the surface is tilted at 45° with respect to the (100) axis (Fig. 1.8). Region III corresponds to the reconstructed checkerboard phase and region IV is the disordered (rough) phase. The line from (0,1) to (1,0) is the roughening transition line; this transition is in the Kosterlitz-Thouless universality class [31].

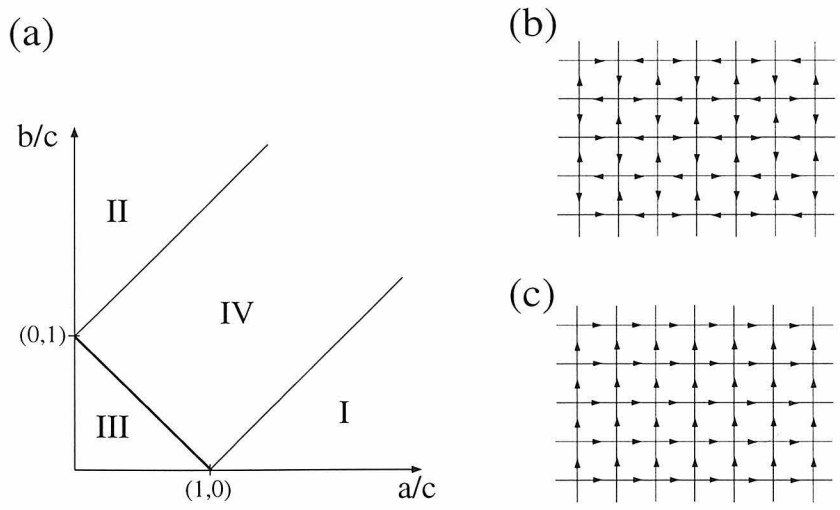

Figure 1.8: (a) Phase diagram for the generalized F-model. (b) Surface configuration in the ground state (III).(c) Surface configuration in phase I.

Some years ago K. Rommelse and M. den Nijs [2, 3, 4] investigated the effects of inter-step interaction in the model for roughening described similar to the discrete Gaussian model described by equation 1.3 (recall that there was a step energy J per unit length in that model but no additional step-step interaction energy). A step-step interaction is exactly equivalent to introducing a next-nearest neighbor interaction in $\mathcal{H}_{DG}$ and such an interaction is very reasonable on physical grounds. The model of Rommelse and den Nijs is therefore a combination of the F-model and the general step-energy models described above: Steps are represented by directed lines with an energy $J_1/2$ per unit length. Moreover step intersections (vertices) are assigned energies as in the F-model: ($\epsilon_1 = \epsilon_2 = \epsilon_3 = \epsilon_4 = 2J_2 > 0$ and $\epsilon_5 = \epsilon_6 = 0$). This model is quite different from the ordinary F-model because there is no requirement that the network of steps form an ordered lattice. The Hamiltonian for this model can be expressed concisely as:

$$\mathcal{H}_{RSOS} = \frac{J_1}{2}\sum_{\langle ij\rangle}(h_i - h_j)^2 + \frac{J_2}{2}\sum_{(ik)}(h_i - h_k)^2 \tag{1.5}$$

where h_i represents the column height of the SOS model; the first summation is over nearest neighbors and the second is over next nearest neighbors. In addition, the

RSOS condition (which mandates that the height difference between nearest neighbors can be at most one unit) is imposed as usual.

The inclusion of the next-nearest neighbor interaction introduces very interesting and non-trivial consequences. It implies that there is no cost to putting two antiparallel directed lines next to each but that two parallel lines will have higher energy and will thus "repel" each other as in Fig. 1.9. At low temperature the line

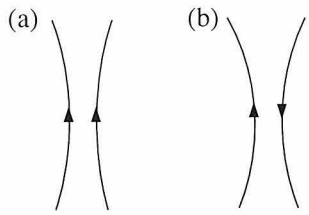

Figure 1.9: (a) Positive interaction energy repels two parallel steps. (b) No repulsion between antiparallel steps.

density on the surface is low and step-step interaction is not an issue. At higher temperatures, however, when the line density increases, one might expect the energy cost of parallel lines to dictate that adjacent arrows be anti-parallel. If one disregards the direction of the arrows, the line geometry looks essentially exactly like the line geometry in the rough phase (compare Fig. 1.10 with Fig. 1.1(b)) however once

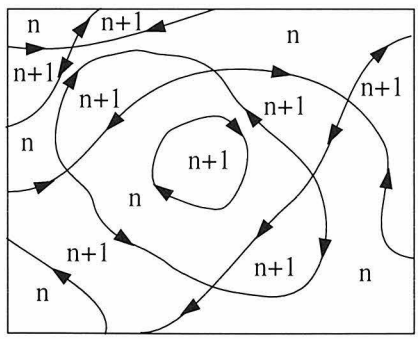

Figure 1.10: The Disordered Flat Phase for the same line geometry as in Fig. 1.1; the arrow configuration is quite different however.

arrows are considered, a crucial difference emerges: the inter-step interaction now introduces a long range arrow order; adjacent arrows point in opposite directions. This arrow-ordered but line-disordered phase is the new disordered flat (DOF) phase.

In terms of surface structure the long range arrow order means that an up-step is typically followed by a down-step and vice-versa. Thus the surface is essentially flat (i.e. $\lim_{|i-j|\to\infty}\langle(h_i - h_j)^2\rangle \to \text{const} < \infty$).

Rommelse and den Nijs formalize the above arguments by expressing the partition function of the system as

$$Z_{RSOS} = \sum_{\{s(\mathbf{r})\}} e^{-E(\{s(\mathbf{r})\},K)} \cdot Z_{\text{F-model}}(\{s(\mathbf{r})\}, L) \tag{1.6}$$

where the summation is over all possible *undirected* networks of lines (the undirected lines can be realized as domain walls of a two state classical Ising model with exchange constant $J = k_b T K$ for a particular configuration of spins, $\{s(\mathbf{r})\}$). $Z_{\text{F-model}}$ is the partition function due to different arrow arrangements on a given set of Ising walls. The interplay between Ising and F-model transitions leads to the DOF phase and the novel preroughening transition.

As an aside it should be noted that a spin-1 quantum chain is equivalent to a highly anisotropic RSOS model with next-nearest neighbor interactions [2]. This equivalence has been exploited to elucidate the properties of valence bond solid phases in spin chains and to clarify the Haldane conjecture.

1.4 Layering critical phenomena

Everything we have discussed so far relates to a free surface on a bulk semi-infinite crystal. This is important because it means that the potential experienced by an atom on the surface is an *exactly periodic* function of the number of layers: if a completed layer contains N_A atoms, the addition to the surface of a further N_A atoms yields a state thermodynamically indistinguishable from the original. It is this property that makes roughening and preroughening so different from more conventional two-dimensional critical phenomena.

For films of finite thickness there are two complimentary regimes: One is the limit of single layer phenomena. Monolayer and submonolayer physics is a vast subject;

important phenomena which it encompasses include the 2-D dislocation mediated melting of Kosterlitz-Thouless-Halperin-Nelson-Young (KTHNY) [22, 23, 32, 33, 34], commensurate-incommensurate phase transitions [35, 36, 37, 38], and a whole zoo of reconstruction transitions.

The other interesting limit is the thick film limit. Here the existence of a substrate at some depth below the surface of the crystal breaks the translational symmetry present in a semi-infinite crystal formed for example by considering a crystalline slab of finite thickness, or by growing a finite number of layers of the crystal on a smooth substrate made of a different material, For surface transitions like roughening and preroughening which involve an infinite number of layers, this broken symmetry profoundly alters the nature of the phase transition. Thermodynamics will no longer be periodic in the number of layers, and the types of surface phases may change drastically from layer to layer. Nevertheless, for a sufficiently large number of layers, the surface thermodynamics must, in some way, approach that of the perfect, bulk crystal surface. Conversely, the bulk surface phases and phase transitions must be reflected somehow in the behavior of a finite but sufficiently thick film. Motivated by the results of some recent experiments on rare gases adsorbed on graphite substrates [41, 52, 53, 54], our purpose will be to explore precisely this latter issue.

1.5 Outline

In this thesis we will examine various solid-on-solid models of surface critical phenomena in the presence of a substrate potential. It is our aim to understand the conditions under which ordinary preroughening, first order preroughening, θDOF preroughening, or perhaps something entirely different occur. Much can be understood qualitatively based on the sine-Gordon (closely related to the Coulomb gas) representation of the roughening and preroughening transitions [4], generalized to include a substrate potential. However our main quantitative tool will be a mean field theory sophisticated enough to account for all of the possible surface phases. Since the issue here is really the topology of the phase diagram, rather than the nature

of the critical points (which are all Ising-like for finite layer thickness n, and, in any case, the experiments do not resolve detailed critical behavior) one can go a long way with mean field theory, even to the point of obtaining semi-quantitative results.

In Chapter 2 we will summarize the various possible layering diagrams derived in later chapters.

In Chapter 3 we introduce the restricted solid-on-solid ($RSOS$) models of crystal-vapor interfaces and discuss their general properties. A great deal of intuition can be obtained by considering the limit of a strong substrate potential and restricting the model to a small number (two or three) of layers. One then obtains effective spin-j (with $j = \frac{1}{2}$ or $j = 1$) Ising models whose phase diagrams can be understood quite generally. A plaquette mean field formalism is then developed for later detailed computations.

In Chapter 4 we will use generalized sine-Gordon models along with renormalization group arguments to discuss the phenomenology of the layering phase diagram. In so doing we will uncover the four basic classes of layering behavior for thick films shown in Figs. 2.1(b-d).

In Chapter 5 we explore solutions to the mean field equations, classifying, to some extent, the possible phase diagrams. In addition we explore a number of phase diagrams that do not have sine-Gordon model descriptions, namely those that involve reconstruction. As alluded to above, some of these mimic closely some of the phase diagrams involving preroughening, but there are significant experimentally observable differences.

In Chapter 6 we conclude by comparing the theoretical and experimental phase diagrams. We also describe future work that might help in the search for new experimental systems that display the so far unobserved phase diagrams.

Various appendices contain more technical derivations. App. A contains a formal development of consistent plaquette mean field theories. In App. B explicit expressions for the free energies on various lattices and for various plaquettes are derived and in App. C the equivalence between the staggered BCSOS model and the Ashkin-Teller model is made explicit.

Chapter 2 Phase Diagrams

For future reference and in order to motivate some of the calculations and models of later chapters we collect some of our main results in this chapter. While this is by no means a complete summary of our work, this collection of phase diagrams does include the most essential results.

All phase diagrams in Fig. 2.1 have been computed using a sophisticated plaquette mean field theory, to be introduced in later sections, applied to the restricted solid-on-solid ($RSOS$) model. The model, which will be introduced in detail in Chap. 3, contains two parameters, $K = J_1/k_BT$ and $L = J_2/k_BT$, where J_1 and J_2 are, respectively, nearest and second nearest neighbor interactions between the surface heights, $h(\mathbf{r})$. For present purposes one need only know that positive J_1 energetically favors neighboring columns of equal height, while negative J_1 favors a unit height difference; J_2 is always kept positive, and favors second neighboring columns of equal height. The first plot, Fig. 2.1(A), is the bulk interface phase diagram for this model. We see clearly here five of the six different phases we have discussed (the θDOF phase does not appear in this model), and the transition lines between them. The inset to Fig. 2.1(A) shows the sixth possible phase, the θDOF phase. In the center of Figs. 2.1(B) and 2.1(C) are shown various paths through the bulk phase diagram. Associated with each of these paths is a layering phase diagram, Figs. 2.1(A)(a-d), 2.1(B)(e-h) corresponding to the same $RSOS$ model but now including a substrate potential.

Path 1 shows ordinary surface roughening behavior. The relation between this behavior and layering critical phenomena is actually well known (see especially [61]): the roughening temperature, T_r, is the accumulation point for the sequence of critical points, $T_{c,n}$, that terminate the first order layering transitions at lower temperatures [see Fig. 2.1(B)(a)]. The nth layering line separates phases with approximately integer film thicknesses, $n-1$ and n, and ends in an Ising critcial point, $T_{c,n}$.

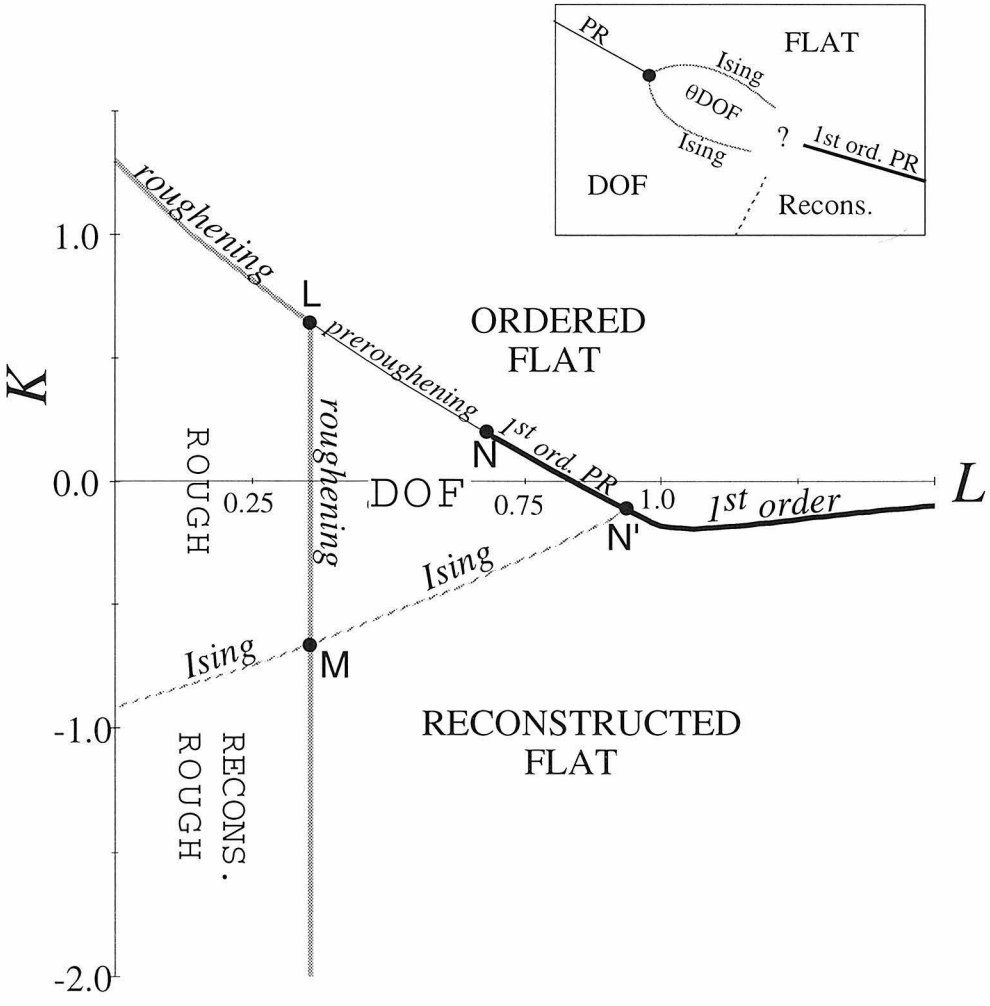

Figure 2.1: **A**: Global phase diagram, as computed using a plaquette mean field theory on a square lattice, for the $RSOS$ model of a bulk interface, with $K = J_1/k_BT$ and $L = J_2/k_BT$ the nearest and next nearest neighbor interactions, showing the six possible different surface phases. The inset shows schematically an alternative scenario containing the θDOF phase. This scenario is not found in the $RSOS$ model we study (hence the remaining questions about how some of the transition lines connect up), but is expected to appear in other models.

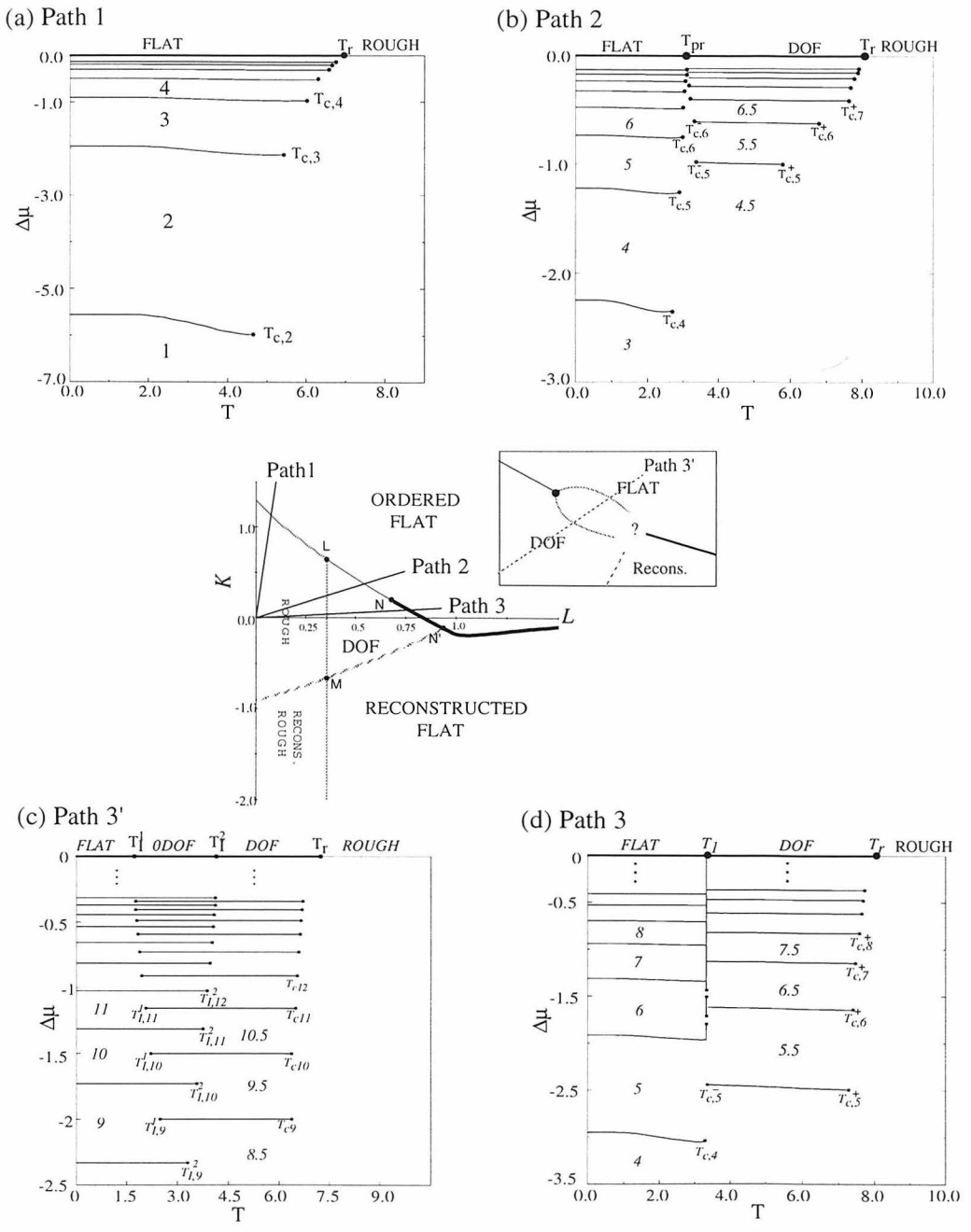

Figure 2.1: **B**: Paths 1-3 represent possible experimental trajectories through this phase diagram. The surrounding figures show the layering phase diagrams associated with these paths when a substrate potential is included: (a) Pure roughening behavior and associated low temperature layering transitions, path 1. (b) Continuous preroughening behavior and associated reentrant layering, path 2. (c) θDOF phase behavior and associated intermeshing, path 3′. (d) First order preroughening behavior and associated zippering, path 3.

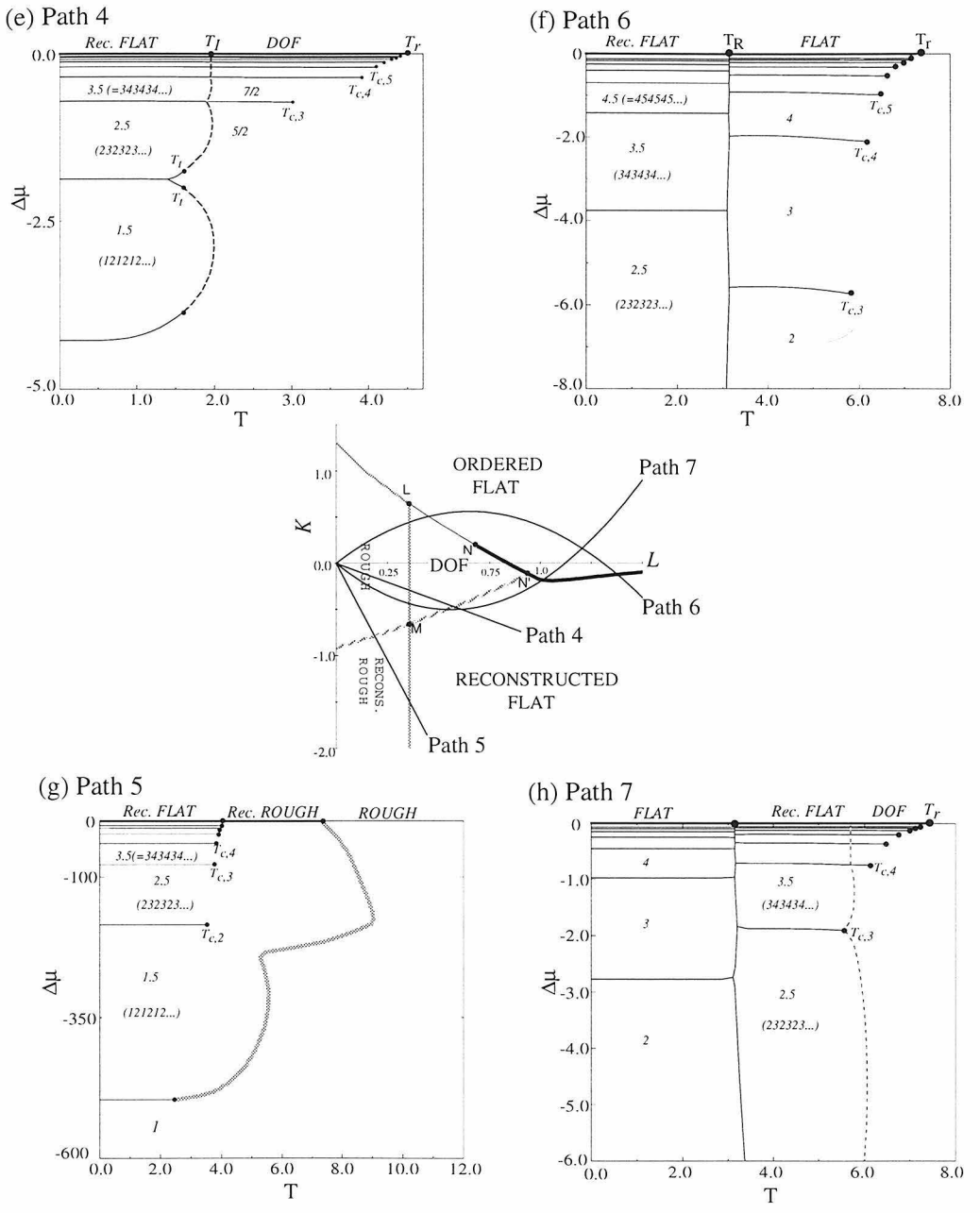

Figure 2.1: **C**: Paths 4-7 represent additional trajectories through the phase diagram. (e) *DOF* to Reconstructed behavior and associated antiferromagnetic transitions within each layer, path 4. (f) First order flat to reconstructed behavior, similar to 2.1(B)(d) but with layering lines reversed. (g) Reconstructed rough behavior and associated surrounding antiferromagnetic line, path 5. (h) First order reconstructed to flat behavior, similar to 2.1(B)(d) but with a surrounding antiferromagnetic line.

Paths 2, 3 and 3′ cut, in various ways, through the $J_1 > 0$ portion of the DOF phase, and are the primary focus of this paper. Path 2 corresponds to ordinary preroughening. Den Nijs has proposed some possible associated layering phase diagrams [5]. The basic idea is that there should be two sequences of layering transitions. At low temperatures, $T \lesssim T_{pr}$, there is a sequence of first order layering transitions between integer coverages, while at higher temperatures, $T_{pr} \lesssim T \lesssim T_r$, there is a sequence of first order layering transitions between integer-plus-one-half (or, more generally, integer-plus-θ_R) coverages. The second set of lines must therefore be reentrant, with upper and lower endpoints $T_{c,n}$ and T_n^2, respectively. The low temperature set have only upper endpoints, T_n^1. The temperatures $T_{c,n}$ still tend to T_r as $n \to \infty$. What was not previously understood is in what way (if at all) the endpoints T_n^2 and T_n^1 are connected together. Den Nijs [5] suggests two possibilities: (a) T_n^1 and T_n^2 are *Ising critical points*, as are $T_{c,n}$, with $T_n^1, T_n^2 \to T_{pr}$, and are not connected in any way [Fig. 2.1(B)(b)]; (b) T_n^2 and T_n^1 are *triple points*, "zipped" together by a sequence of first order lines, with $T_n^1, T_n^2 \to T_0$ [Fig. 2.1(B)(d)]. We distinguish between T_{pr} and T_0 for reasons that will become clear below. Another possibility (c) is that the two sets of layering lines *intermesh*, with distinct limits $T_n^1 \to T_I^1$ and $T_n^2 \to T_I^2$ where $T_I^2 < T_I^1$ [Fig. 2.1(B)(c)]. The high resolution heat capacity studies [52, 53, 54] suggest possibility (b). We will show that, depending on parameters, all of these possibilities, as well as others, can occur. Possibility (a) indeed corresponds to a continuous preroughening transition, path 2; while (b) corresponds to a *first order* transition between flat and DOF phases (T_0 denoting then the first order preroughening temperature), path 3; and (c) to a θDOF phase in the temperature interval $T_I^2 \leq T \leq T_I^1$, path 3′. The bulk interface transitions T_I^2 and T_I^1 are also Ising like, and in the θDOF phase one has a continuously varying surface coverage, $0 \leq \theta(T) \leq \frac{1}{2}$ with $\theta(T_I^2) = 0$ and $\theta(T_I^1) = \frac{1}{2}$.

Although not relevant to present experiments, one may also cut through the DOF phase with $J_1 < 0$, ending with a reconstructed phase at lower temperatures. This is represented by path 4, and the associated layering phase diagram is shown in Fig. 2.1(C)(e). Here there is only one set of layering lines, between half-integer cov-

erages. However, for each given film thickness an Ising antiferromagnetic ordering transition takes place at intermediate temperatures. This transition becomes the DOF-Reconstructed phase boundary on the bulk interface. The roughening transition at higher temperatures is again reflected in the sequence of Ising critical points, $T_{c,n}$.

Path 5 shows behavior for larger $|J_1|/J_2$, where the surface roughens before it deconstructs, yielding an intermediate *reconstructed rough* phase. The associated layering phase diagram [Fig. 2.1(C)(g)] displays a sequence of layering transitions between half-integer film thicknesses lying *completely within* an antiferromagnetic phase boundary. The nature of the order within this boundary is quite subtle, corresponding to antiferromagnetic order in the magnitude of the *mean square fluctuations* of each column height, not in the column heights themselves. The latter symmetry is broken only below $T_{c,n}$.

We also show layering phase diagrams for somewhat fanciful continuations of paths 1 and 5 which cross the first order flat to reconstructed phase boundary [see Figs. 2.1(C)(f,h)]. There is no experimental evidence for J_1 changing sign as a function of T, but the resulting phase diagrams, while not associated in any way with the DOF phase, are remarkably similar in appearance to Fig. 2.1(B)(d), associated with first order preroughening, and the experimental results for Argon and Krypton on graphite [52, 53, 56]. The continuation of path 1, shown in Fig. 2.1(C)(f), is identical to Fig. 2.1(B)(d), except that the integer and half-integer layering lines are interchanged. Ellipsometry [41] and vapor pressure isotherm measurements [52, 53, 54, 62], however, are sufficiently accurate to rule out such an interchange. The continuation of path 5 shown in Fig. 2.1(C)(h) has the two sets of layering lines in the correct order, but, just as in Fig. 2.1(C)(f)), they are surrounded by an antiferromagnetic Ising phase boundary. Once again, there is no evidence for the latter in any of the experiments.

As mentioned, the experimental graphite subtsrate lattice is triangular. Indications are that the reentrant layerings nevertheless occur at half filling. Although $\theta_R = \frac{1}{2}$ reconstructed phases, such those with every second *row* missing, do exist on a

triangular lattice, they do not arise in a natural way if the interactions are isotropic. It is likely, then, that for the models we consider here there is no stable half filled reconstructed phase. Until now, this was thought to be a problem for the DOF phase interpretation of reentrant layering [5]. What we will show, however, is that the absence of a reconstructed phase actually *enhances* the DOF phase, and that there are *two* factors that one must consider in determining the filling fraction, θ, at which it occurs. Thus, although it is *energetics* that favors a DOF phase with filling fraction θ_R, it is *entropy* that drives the preroughening transition and disfavors integer filling fractions. In the absence of the former, the latter will tend to form a DOF phase half way between the two bounding integer coverages even in the absence of an "attracting" incipient reconstructed phase, just as seen in the experiments. The triangular lattice bulk interface phase diagram, as computed using our plaquette mean field theory, is shown in Fig. 2.2. As can be seen, the main difference between this figure and Fig. 2.1(A) is the absence of the reconstructed and reconstructed rough phases, and the correpsondingly expanded DOF phase. The $K > 0$ portion of the phase diagram is, however, qualitatively unchanged.

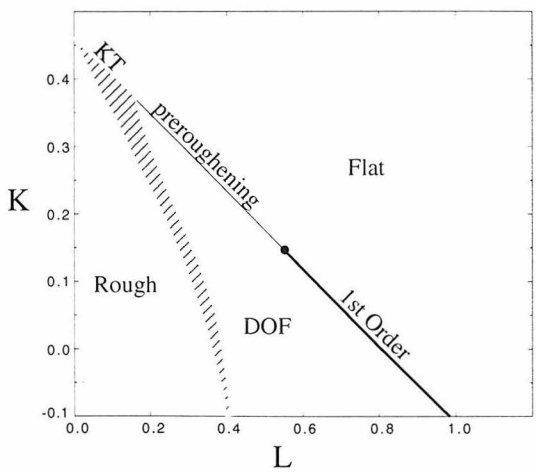

Figure 2.2: Global phase diagram, as computed using a plaquette mean field theory on a triangular lattice, for the $RSOS$ model of a bulk interface. The reconstructed and reconstructed rough phases, and transitions associated with them, are now absent, leading to a much enlarged DOF phase. The behavior for $K > 0$, however, is qualitatively unchanged from that for a square lattice, Fig. 2.1(A).

Chapter 3 Models and methods

3.1 Solid on solid models

Solid on solid (SOS) models are conventionally used to model interface phenomena. In these models the vapor phase above the surface is taken to be a perfect vacuum, while the solid phase below is taken to be a perfect crystal, and surface overhangs are ignored. The surface is then defined by a set of column heights, $h(\mathbf{r})$, above a two dimensional lattice spanned by the index $\mathbf{r}$. To begin with we shall assume a simple square lattice with $h(\mathbf{r})$ taking integer values. Later on we shall discuss the experimentally more relevant case of a triangular lattice. In fact, the bulk crystals considered here have a face centered cubic structure in which sequential layers of atoms sit in the interstices of the previous layer. Although, for a given $\mathbf{r}$, $h(\mathbf{r})$ can change only in integer steps, neighboring heights will then differ by noninteger amounts. For simplicity of modelling, we shall ignore this complication and take the triangular lattices to lie one on top of the other so that all $h(\mathbf{r})$ are integers. In the *restricted* solid on solid (RSOS) models, the further constraint is imposed that neighboring column heights can differ by at most unity. This reflects the physical constraint that it is energetically unfavorable to form steps of greater than unit height. In the RSOS models the energy barrier against such steps is simply taken to be infinite. This constraint greatly reduces the number of surface configurations and therefore simplifies certain analytic and numerical calculations (see below) without affecting the basic physics. It also decreases the configurational entropy, and roughness, of the surface relative to that of, say, the interface between oppositely magnetized domains in a three-dimensional Ising model. This tends to stabilize more delicate phases, like the disordered flat phase, which rely on a critical balance between configurational entropy and step free energy barriers. Clearly, whether the SOS model, RSOS model, or something in between, is most appropriate depends upon the details of the system

being modeled.

Following den Nijs [4], we first consider the RSOS Hamiltonian on a square lattice,

$$\begin{aligned}\mathcal{H} &= \frac{1}{2}J_1 \sum_{<\mathbf{r},\mathbf{r}'>} [h(\mathbf{r}) - h(\mathbf{r}')]^2 + \frac{1}{2}J_2 \sum_{(\mathbf{r},\mathbf{r}'')} [h(\mathbf{r}) - h(\mathbf{r}'')]^2 \\ &+ \sum_{\mathbf{r}} V[h(\mathbf{r})], \end{aligned} \tag{3.1}$$

where the first sum is over nearest neighbors and the second sum is over second (i.e. diagonal) neighbors. We assume $J_2 > 0$ always, but J_1 can be either positive or negative. The external potential, $V(h)$ [in the absence of which, (3.1) is precisely the model treated in [4]] is due to the substrate, and takes the form [61] (see Fig. 3.1)

$$V(h) = \begin{cases} h\Delta\mu + v(h), & h \geq 0 \\ \infty, & h < 0, \end{cases} \tag{3.2}$$

with $v(h) \approx ch^{-\alpha}$ for large h. For a van der Waals substrate potential, $\alpha = 2$ and $c > 0$. The linear coefficient, $\Delta\mu = \mu_{coex} - \mu$, is the deviation of the chemical potential from bulk solid-vapor coexistence. For $\Delta\mu > 0$ the bulk phase is vapor, while for $\Delta\mu < 0$ the bulk phase is solid. A true bulk equilibrium interface exists only for $\Delta\mu = 0$ (precisely analogous to external magnetic field $H = 0$ in an Ising model). If J_1 and J_2 are both positive, then at zero temperature the interface is perfectly flat and its equilibrium position is at the minimum, $h_0(\Delta\mu, T = 0)$, of $V(h)$ (over integer values of h). For small $\Delta\mu$ the minimum diverges as

$$h_0(\Delta\mu) \approx \left(\frac{\alpha c}{\Delta\mu}\right)^{\frac{1}{1+\alpha}} \sim \Delta\mu^{-\frac{1}{3}}, \ \Delta\mu \to 0. \tag{3.3}$$

It is for this reason that absorption isotherms, which essentially measure $h_{eq}(\Delta\mu, T) \equiv \langle h(\mathbf{r})\rangle$ as a function of $\Delta\mu$ for fixed T, are often plotted versus $\Delta\mu^{-\frac{1}{3}}$: the steps due to the sequence of layer completions then occur with roughly equal spacing [52, 53].

The physics behind (3.1) is as follows. Consider first a bulk interface with $V \equiv 0$. If J_1 is positive and large compared to J_2, the energetics give preference to a flat interface, and the model will produce a standard roughening transition with increasing

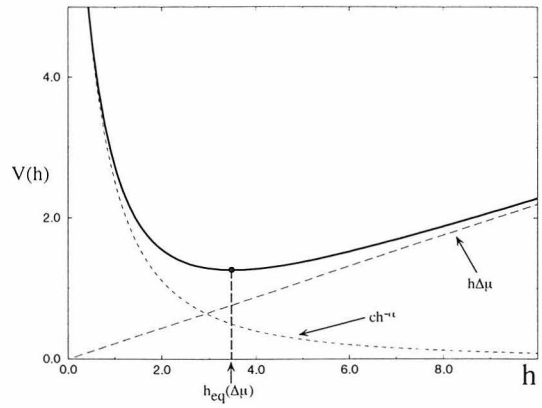

Figure 3.1: Substrate potential, $V(h)$.

temperature when $K \equiv J_1/k_BT$ and $L \equiv J_2/k_BT$ are sufficiently small. If $J_1 < 0$ and is large in magnitude compared to J_2, neighboring column heights prefer to differ by unity. However, since J_2 prefers that diagonal nearest neighbor column heights have equal height, an antiferromagnetic order is stabilized at low temperature: this is the checkerboard reconstructed phase. As K decreases, this phase roughens, but still retains a generalized long-range antiferromagnetic order [2]. A second Ising-like transition, at higher temperature, into a fully rough phase is required to finally eliminate this residual order. However, if $J_1 < 0$ is sufficiently small in magnitude, the antiferromagnetic order can be lost, via an Ising transition, *before* the surface roughens: this is the transition to the disordered flat phase. This phase actually persists also for $J_1 > 0$, but small: the entropy gain from disordering the surface more than offsets the loss of ferromagnetic energy. Fig. 2 in [4] and Fig. 2.1 of this work show how these four phases fit together.

Now, how are these phases affected by the presence of $V(h)$? The effect on the rough phases is catastrophic! Since $V(h)$ prefers a set of values of h near $h_0(\Delta\mu)$, the correlation function $G(\mathbf{r})$ [see (1.1)] must always remain finite as $|\mathbf{r}| \to \infty$. The logarithmic divergence in (1.2) must saturate. We may estimate the saturation value as follows: assuming that the interface does not wander too far from the minimum,

it will be governed by the effective Hamiltonian

$$\bar{\mathcal{H}}_{eff} \equiv \frac{\mathcal{H}_{eff}}{k_B T} = \frac{1}{2}\int d^2r \left[K_R|\nabla h|^2 + \kappa(h-h_0)^2\right] \tag{3.4}$$

where

$$\begin{aligned} k_B T\kappa &= \left(\frac{\partial^2 V}{\partial h^2}\right)_{h=h_0} \approx \alpha(\alpha+1)\left(\frac{\Delta\mu}{\alpha c}\right)^{\frac{2+\alpha}{1+\alpha}} \\ &\sim \Delta\mu^{\frac{4}{3}} \end{aligned} \tag{3.5}$$

is the curvature at the minimum, and K_R is the effective long wavelength (renormalized) tilt modulus [see (1.1)] in the absence of V. This Hamiltonian is Gaussian, and yields

$$\begin{aligned} \langle (h-h_0)^2\rangle &\approx \int_{q\lesssim\frac{\pi}{a}} \frac{d^2q}{(2\pi)^2}\frac{1}{K_R q^2+\kappa} \\ &= \frac{1}{4\pi K_R} ln\left[1+\frac{\pi^2 K_R}{\kappa a^2}\right] \\ &\approx \frac{2+\alpha}{1+\alpha}\frac{1}{4\pi K_R} ln\left(\frac{c}{\Delta\mu}\right) \ll \frac{1}{\kappa}, \end{aligned} \tag{3.6}$$

which also estimates the saturation value of $G(\mathbf{r})$. The final inequality tells us, self consistently, that although the interface width diverges logarithmically as $\Delta\mu \to 0$, the interface remains sufficiently close to h_0 that the quadratic approximation remains valid.

Clearly, the flat phases will be affected by the potential in much more subtle ways. They will, of course, remain flat. The question we address is the nature of the various transitions between them in the presence of $V(h)$.

3.2 Effective layer Hamiltonians

From the general Hamiltonian (3.1) one can derive various approximate effective Hamiltionians for describing the thermodynamics of individual layers. The basic

idea is that if the effective potential, $V(h)$, increases rapidly to either side of the minimum near $h_0(\Delta\mu)$, then large deviations of the column heights from h_0 will be strongly discouraged, and, to a good approximation, one can suppress all values of $h(\mathbf{r})$ outside of some narrow range. If this range encompasses an integer $2j+1$ of values, one then has reduced the full Hamiltonian to one of a classical spin-j Ising model. It will transpire that a description of the thin film analogue of the disordered flat phase requires $j \geq 1$. However, we will begin our discussion with the simpler spin-$\frac{1}{2}$ model.

3.2.1 Spin-j Ising models

A spin-$\frac{1}{2}$ description is valid if the substrate potential is so strong as to allow essentially only one value of the column heights, except when the value of $\Delta\mu$ is such that two column heights, say n and $n+1$, are nearly degenerate in energy. In this latter situation the true minimum of $V(h)$ lies near $n+\frac{1}{2}$, and $V(n) \approx V(n+1)$. Physically, we expect this to be a valid description for films only a few layers thick. We define the spin-$\frac{1}{2}$ variables $s(\mathbf{r})$ via

$$s(\mathbf{r}) = \begin{cases} -1 & \text{if } h(\mathbf{r}) = n \\ 1 & \text{if } h(\mathbf{r}) = n+1. \end{cases} \tag{3.7}$$

Ignoring all other possible values of $h(\mathbf{r})$, the Hamiltonian now becomes

$$\begin{aligned} \bar{\mathcal{H}} \;&\approx\; \bar{\mathcal{H}}_{\frac{1}{2}} \equiv \frac{1}{2}K \sum_{\langle \mathbf{r}\mathbf{r}' \rangle} [s(\mathbf{r}) - s(\mathbf{r}')]^2 \\ &+\; \frac{1}{2}L \sum_{(\mathbf{r}\mathbf{r}'')} [s(\mathbf{r}) - s(\mathbf{r}'')]^2 - h \sum_{\mathbf{r}} s(\mathbf{r}) \end{aligned} \tag{3.8}$$

where $\bar{\mathcal{H}} \equiv \mathcal{H}/k_BT$, $\bar{\mathcal{H}}_{\frac{1}{2}} \equiv \mathcal{H}_{\frac{1}{2}}/k_BT$, $h = H/k_BT$ with $H = \frac{1}{2}[V(n) - V(n+1)]$ an effective magnetic field, and we have dropped an overall constant term, $C = \frac{1}{2}[V(n) + V(n+1)]N_A$ where N_A is the number of atoms per layer. We should really distinguish between the coupling constants K and L that appear in (3.8) and those that appear in (3.1) because the former are effective parameters that will differ

somewhat from the latter in a way that depends upon how good an approximation the spin-$\frac{1}{2}$ model is. For simplicity of notation, however, we will not make this distinction explicit. For $L = 0$ this is the standard two-dimensional Ising Hamiltonian. If $K > 0$ the model is ferromagnetic, and when $H = 0$ there is a phase transition to a state with finite magnetization as K increases through a critical value $K = K_c$ [see Fig. 3.2(a)]. If $K < 0$ the model is antiferromagnetic. Since H does not couple directly to the staggered magnetization order parameter in this case, there is a *line* of transitions, $K = K_c(H)$ [see Fig. 3.2(b)], to states with finite staggered magnetization. Thus, although H polarizes the spins somewhat, antiferromagnetic order survives if H is not too large. Clearly, one must have $K_c(0) = -K_c$. This line terminates at $T = 0$ ($K = -\infty$) for a critical value of the field, $H = \pm H_c$, with $H_c = -2J_1$. Since $L > 0$ encourages the alignment of diagonal nearest neighbor spins, it enhances *both* ferromagnetic *and* antiferromagnetic order. If L is not too large, the phase diagrams are qualitatively unchanged.

For large $L > 0$, new behavior occurs. Suppose $K = 0$. Then the two interpenetrating sublattices are decoupled, and L provides a nearest neighbor ferromagnetic coupling within each one. Thus, at $H = 0$ and a critical value, $L = K_c$, the two sublattices will independently order ferromagnetically. We may view a small value of K as a perturbation on this behavior, which then determines how these two sublattices orient relative to one another. If $K > 0$ (but arbitrarily small) the two will order parallel to each other, yielding an overall ferromagnetic state; if $K < 0$ (but arbitrarily small) the two will order antiparallel to each other, yielding an overall antiferromagnetic state. There is therefore a first order transition from one ordered state to the other when K reverses sign at large enough L.

For nonzero H the ferromagnetic part of the critical line is destroyed (see Fig. 3.3(b)), but the antiferromagnetic part survives, and must merge somehow with the extension of the first order decoupling line, $K = 0$, $L > K_c$. For large L it is easy to see that the latter moves to negative $J_1 \simeq -\frac{1}{2}|H|$ since a finite $K < 0$ is now required to overturn one sublattice against the field. For small L the transition remains second order. How the two behaviors connect at intermediate L is surprisingly complicated:

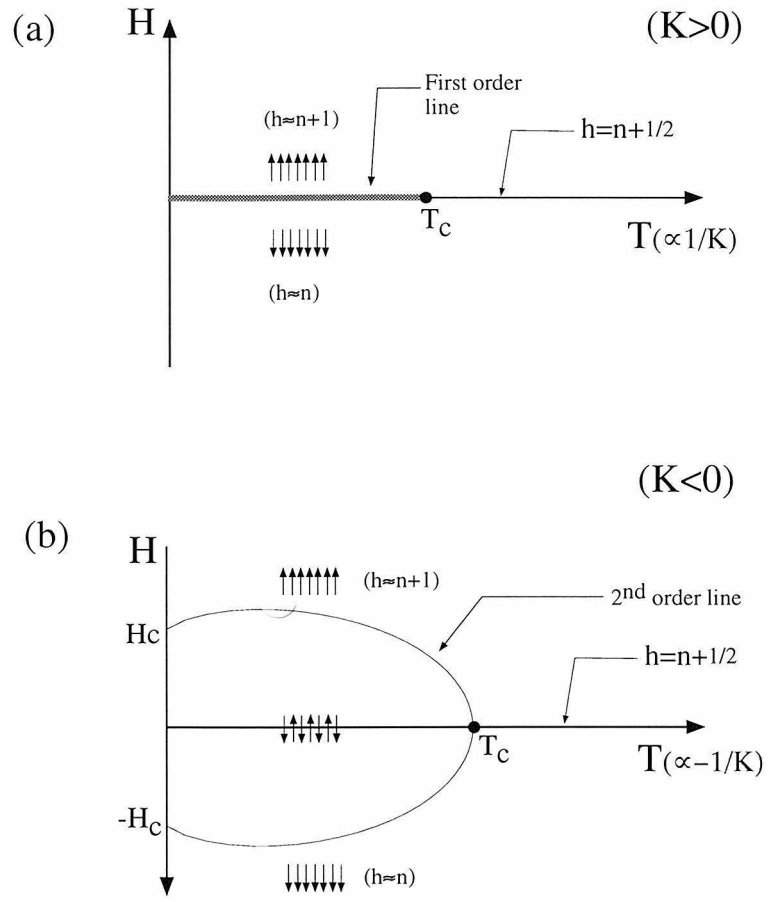

Figure 3.2: (a) Ferromagnetic and (b) antiferromagnetic Ising phase diagrams for $L = 0$.

for smaller H the two meet in a tricritical point, while for larger H the second order line ends in a critical endpoint on the first order line, while the first order line ends in an Ising critical point *inside* the antiferromagnetic phase. A *tetracritical point*, at a particular value of $H = H_{c4}$, separates these two behaviors. The phase diagrams in the H-T plane are shown in Fig. 3.3(a). A three-dimensional phase diagram in the full H-K-L space is shown in Fig. 3.3(b). All this will be described in more detail in Chapter 5.

Let us now understand the relationship between this phase diagram and the layering transitions in the solid-on-solid model. Consider first $K > 0$ and $L = 0$. At low temperature K will be larger than K_c, and as H passes through zero a first order transition will take place between the spin down ferromagnetic phase and the spin

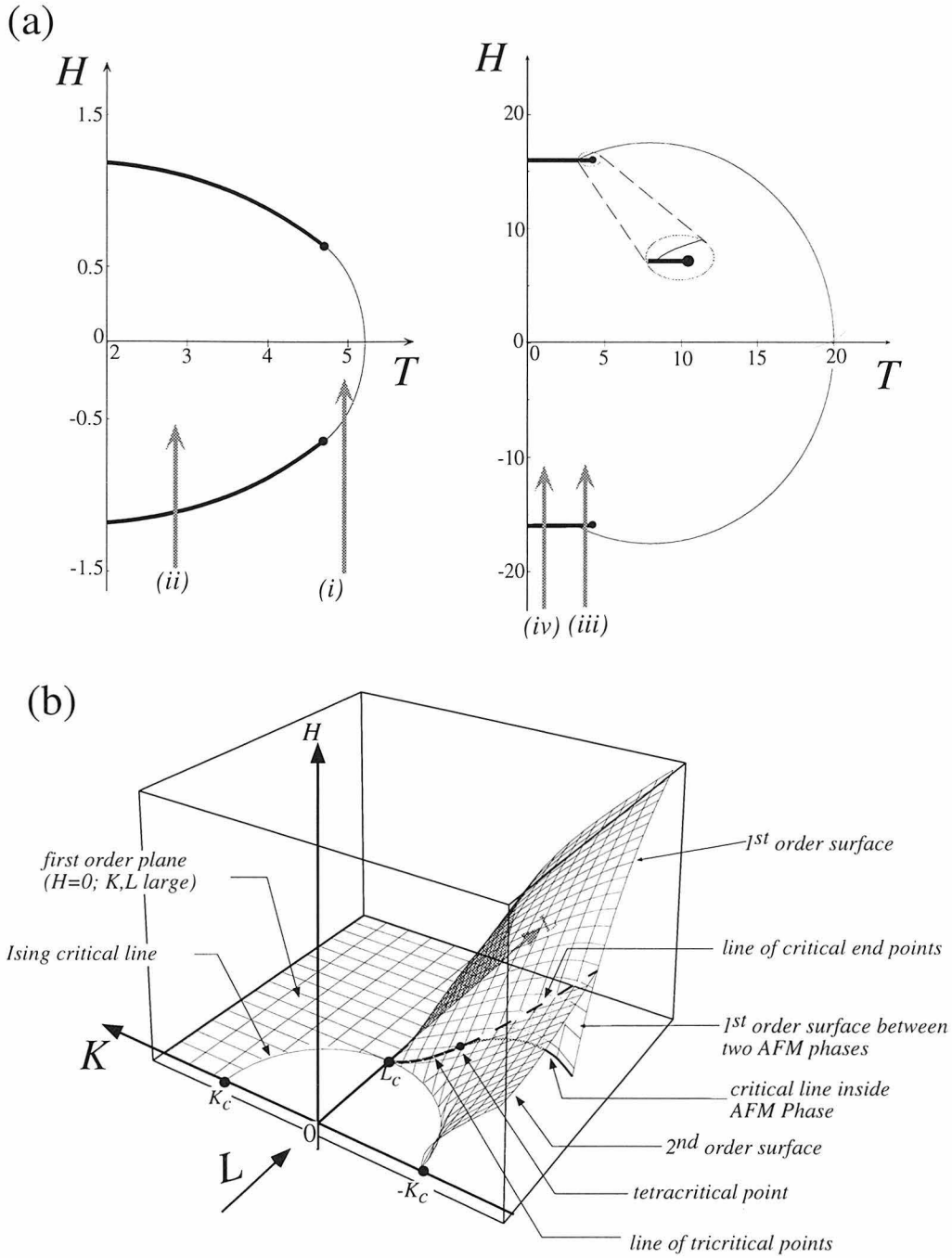

Figure 3.3: (a)Ising phase diagrams for $L > 0$: (a) H vs. T phase diagrams showing tricritical behavior for $J_2/|J_1| > j_{4c}$ and critical end point behavior for $J_2/|J_1| < j_{4c}$. Fig. 3.2(b) is recovered as $J_2/|J_1| \to 0$. The paths labelled (i),(ii), (iii), and (iv) refer to the corresponding parts of Fig. 5.1. (b) Three-dimensional plot, with details of the tricritcial and critical endpoint structure shown.

up ferromagnetic phase. This corresponds to a first order layering transition (as a function of $\Delta\mu$) between n completed layers, with a dilute gas of atoms (whose density varies continuously with $H < 0$) in the partially completed $(n+1)$st layer, and $n+1$ completed layers with a dilute gas of "holes" (whose density varies continuously with $H > 0$) in the $(n+1)$st layer, occuring precisely when $V(n)$ and $V(n+1)$ are degenerate. This first order line terminates in an Ising critical point, above which the layers grow continuously.

As $\Delta\mu$ decreases further, $V(n+2)$ eventually becomes degenerate with $V(n+1)$, and we leave the domain of validity of the Ising model (3.8). However, we may now ignore the nth layer, which is essentially full and inert, and consider a new effective Ising model, of the same form as (3.8), for the $(n+1)$st and $(n+2)$nd layers. The effective parameters will be slightly different since the precise shape of $V(h)$ has changed, but the same physics will now repeat, with $H = \frac{1}{2}[V(n+1) - V(n+2)]$. In particular, a new layering transition between $n+1$ and $n+2$ layers will now occur. Repeating this whole process indefinitely generates the entire infinite sequence of layering transitions. Of course, our assumption that $V(h)$ effectively isolates only two layers breaks down as the number of layers increases, but the picture actually remains valid. The point is that K prefers a flat surface, and Huse [61] has shown that the endpoints of the layering transitions accumulate at the roughening transition *from the low temperature side*. Therefore the renormalized tilt modulus, K_R, in (3.4) is still infinite, and the interface is flat right through the Ising transition. It is therefore a combination of a weak minimum in $V(h)$ and the fact that $T_{c,n} < T_r$ that maintains the correctness of our simple picture. These results are qualitatively unaffected if $L > 0$ since L just enhances the stability of the flat phase somewhat.

Consider next $K < 0$. The original $RSOS$ Hamiltonian does not really make sense in this case if $J_2 = 0$ since the surface will always be rough: in the absence of a strongly localizing substrate potential, one needs a finite J_2 to stabilize a flat surface at low temperatures. The corresponding effective layer Hamiltonian must then have a positive L. At low temperatures, then, the first order layering lines now broaden out into second order lobes enclosing checkerboard ordered phases that exist in the

interval $-H_c(T) < H < H_c(T)$ [see Figs. 3.2(b) and 3.3(a)]. As above, there will be one such lobe for each value of n. If $V(h)$ is sufficiently steep so that H passes through H_c *before* $V(n+2)-V(n+1)$ becomes smaller than $8|J_1|$, then the transition line reaches right to $T = 0$ and is completely disjoint from the checkerboard phases at neighboring coverages. In principle, all of the complicated triple point or critical end point structure will appear as well. This is shown at the bottom of Fig. 2.1(B)(d). If, on the other hand, $V(n+2) - V(n+1)$ becomes smaller than $8|J_1|$ before H passes through H_c, the neighboring lobes will overlap and one will have a *first order* transition between neighboring checkerboard phases at low temperature. This must happen for sufficiently large n, and is shown in the upper left hand parts of Fig. 2.1(B)(d).

What happens at higher temperatures? There are two possibilities, depending upon the relative strengths of J_1 and J_2. If J_2 is large compared to J_1, then the layering tendency is stronger than the reconstruction tendency, and will survive to higher temperatures. Therefore, as the temperature rises, first the reconstructed phase disorders, while the strong L continues to maintain a flat, roughly half-filled surface. The second order antiferromagnetic Ising transitions then terminate at critical endpoints on the first order layering lines. As the film thickens the reconstruction transitions accumulate at the bulk surface reconstruction transition, $T = T_R$. Meanwhile, the first order layering lines terminate at Ising critical points, $T_{c,n}$, at higher temperatures. These critical points accumulate at the bulk surface roughening transition, $T = T_r$. The bulk surface phase in the interval $T_R < T < T_r$ is precisely the disordered flat phase. This scenario is pictured in Fig. 2.1(B)(d).

If, on the other hand, J_1 is large compared to J_2, the reconstruction tendency is stronger than the layering tendency. Therefore, as the temperature rises, the layering critical points, $T = T_{c,n}$ will occur *completely within* the reconstructed phase. A single second order reconstruction transition line will now enclose all of the layering transition lines (for sufficiently large n), terminating at the bulk surface rough-to-reconstructed-rough transition. The layering endpoints will accumulate at a lower temperature, $T = T_r$, corresponding to the bulk surface reconstructed-flat to reconstructed-rough transition. This scenario is pictured in Fig. 2.1(C)(g).

Even more interesting behavior occurs if the effective coupling, K, *changes sign* as a function of temperature at a value of L larger than L_c. One can then obtain a phase diagram that looks very much like that shown in Fig. 2.1(B)(d), which, as mentioned is seen in experiments.

In Fig. 2.1(C)(f) we show the case where J_1 is antiferromagnetic at low temperatures, turning ferromagnetic at high temperatures. The result is similar to that shown in Fig. 2.1(B)(d), including a zig-zagging line of first order transitions that zip together the two sets of layering lines, differing only in that it is now the integer layering lines that are reentrant. In the bulk interface limit there are still two phase transitions. The surface is reconstructed at low temperatures, converts to the flat phase via a first order transition at $T = T_R$, and finally roughens at $T = T_r$. The two sets of layering triple points, T_n^2 and T_n^1 must accumulate at the same point, $T = T_R$, because when $J_1 = 0$ only J_2 stabilizes the flat surface. For thick films J_2 does not distinguish between half-integer and integer layers, so the switch from one to the other must take place essentially at constant temperature.

In Fig. 2.1(C)(h) we show what happens if J_1 is ferromagnetic at low temperatures and antiferromagnetic at higher temperatures. The possible behaviors are identical at high temperatures to those shown in Fig. 2.1C)(e). The only difference is that at low temperatures a new series of layering transitions between integer coverages takes over. These connect to the half-integer layering transitions in the same way as shown in Fig. 2.1(f), except that high and low temperatures are reversed. In the bulk interface limit there are now three transitions: a first order transition from flat to reconstructed flat at low temperatures, followed by a roughening transition to the film analogue of the reconstructed rough phase, followed finally by an Ising transition to the rough phase.

In neither of the two scenarios shown in Figs. 2.1(C)(f) and (h) is preroughening involved because the reconstructed surface never disorders, but simply converts to the flat phase when J_1 changes sign. We emphasize these scenarios only because they mimic Fig. 2.1(B)(d) but contain completely different physics. Fig. 2.1(C)(h) is especially similar since it is the half-integer layering lines that are reentrant. In both

phase diagrams, the first order zipper appears. The difference now is that there is a higher temperature Ising line below which the rough surface reconstructs. For the experiments that we will discuss, these scenarios are unlikely as there does not seem to be any indication that reconstruction takes place.

Although checkerboard reconstruction is described by the effective spin-$\frac{1}{2}$ Hamiltonian, the layering behavior discussed in the previous paragraphs is not since it involves three values of n. To derive the layering behavior from the $RSOS$ model one must use at least a spin-1 Hamiltonian, which takes the general form

$$\begin{aligned} \bar{\mathcal{H}}_1 &\equiv \frac{1}{2}K\sum_{\langle \mathbf{r}\mathbf{r}'\rangle}[s(\mathbf{r})-s(\mathbf{r}')]^2+\frac{1}{2}L\sum_{(\mathbf{r}\mathbf{r}'')}[s(\mathbf{r})-s(\mathbf{r}'')]^2 \\ &- h\sum_{\mathbf{r}}s(\mathbf{r})+h_2\sum_{\mathbf{r}}s(\mathbf{r})^2, \end{aligned} \tag{3.9}$$

where we have used the parabolic form, $-hs+h_2s^2$, with $h_2=H_2/k_BT$, to fit $V(h)$ for $h=n-1,n,n+1$, and dropped an overall constant $C_1=V(n)N_A$. Clearly the two parameters h, h_2 are all that are required. The restricted solid on solid ($RSOS$) condition now comes into play: since nearest neighbor sites can differ in height by at most unity, spin configurations in which $s(\mathbf{r})=+1$ and $s(\mathbf{r}')=-1$ for nearest neighbor sites $\mathbf{r}$ and $\mathbf{r}'$ are disallowed – in effect $K=\infty$ for $|s(\mathbf{r})-s(\mathbf{r}')|=2$. Detailed computations of the layering behavior described in the previous paragraphs using this model will be presented in Chapter 5.

3.2.2 Film analogue of the DOF phase

The spin-1 model is also required to understand the film analogue of the DOF phase. Recall that preroughening involves a transition from a flat phase to a disordered reconstructed phase (i.e., a disordered flat phase). In the context of a thin film, the disordered flat phase will correspond to a checkerboard phase that has "melted," but nevertheless retains a preference for a certain density of atoms, namely a half filled layer. To describe this properly the model must allow for two such phases: one with an extra half layer on top of the flat phase, and one with a half layer missing from

the flat phase. This is crucial because it will turn out that these two phases arise from a kind of *symmetry breaking* in the flat phase. Given this, it is clear that three different layers enter the physics in a crucial way, and the effective layer Hamiltonian must allow three different values of the spin.

The disordered flat phase on a bulk crystal interface occurs for small K and moderate, but sufficiently large $L > 0$, in order that $|h(\mathbf{r}) - h(\mathbf{r}'')| = 2$, where $\mathbf{r}$ and $\mathbf{r}''$ are second neighbors, is discouraged. The surface therefore is not rough, yet K and L are weak enough that $h(\mathbf{r})$ does not condense into a flat or reconstructed phase, preferring instead to take advantage of the entropy gain associated with a half-filled disordered layer. Clearly J_1 can have either sign, but we will be interested in $J_1 > 0$ so that the flat phase eventually stabilizes at low temperature. In the context of a thin film we are therefore asking the following question: if $H = 0$ but $H_2 \geq 0$ (so that $s = 0$ is nominally preferred) are there conditions under which both K and L are positive (so that, again, $s = 0$ is nominally preferred), and yet a spontaneously broken symmetry exists with $M \equiv \langle s(\mathbf{r}) \rangle \neq 0$? Clearly the *ground state* of $\mathcal{H}_1$ under these conditions is $s(\mathbf{r}) \equiv 0$, but there may be an *entropy driven* transition to a state with $M \neq 0$ in some interval of temperatures. At high temperatures this symmetry breaking will be destroyed due to complete disordering of the film. At low temperatures it will be destroyed as energetics wins out over entropy. Although this scenario yields reentrant behavior of the type we seek, a calculation is required to see which of Figs. 2.1(B)(b-d) give the correct global picture. Note that it is the *absence* of reconstruction in the DOF phase that eliminates the Ising line that is present in Fig. 2.1(C)(h).

3.3 Mean field formalism

The main calculational tool that we will use to explore the questions raised in the previous subsection is a self-consistent mean field formalism. The standard mean field formalism replaces each individual fluctuating spin or height variable by an effective continuous single site magnetization, or average height, which adjusts self-

consistently to the effective field generated by its neighbors. Equivalently, the free energy is computed in a saddle point approximation, with the phase space location of the saddle point determining the single site magnetizations. Since all sites are equivalent in a ferromagnetic state, such an essentially single spin theory suffices to capture the basic physics. For antiferromagnetism on a square lattice, the two sublattices are inequivalent, but if the individual spins interact only with nearest neighbors there is no ambiguity in the local effective field. The single spin mean field theory then again suffices to capture the basic physics. However, if one wishes to describe ordering into a state involving subtle competition between correlations, one must improve the level of approximation by treating the fluctuations within *plaquettes* of nearby spins exactly. Interactions between different plaquettes are still treated self-consistently. The general formalism for doing this is outlined in Appendix A. In our case we are seeking a state that is formed by a delicate balance of nearest neighbor and next nearest neighbor interactions. We therefore must keep enough spins that both types of interaction are present within a plaquette. For the square lattice we shall analyze a model using four spins in a given plaquette [see Fig. 3.4(a)]. For the triangular lattice we shall analyze two models, one with six spin plaquettes [see Fig. 3.4(b)], and one with seven spin plaquettes [see Fig. 3.4(c)].

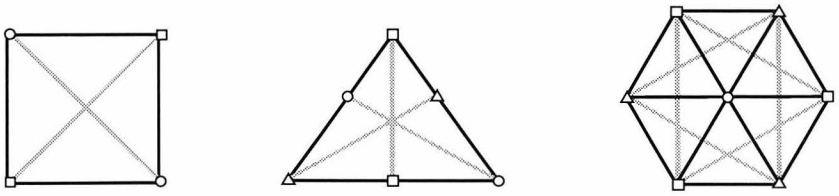

Figure 3.4: (a) Four spin plaquette for the square lattice containing two spins from each of the two sublattices. (b) Six spin plaquette for the triangular lattice which violates the full rotaional symmetry of the lattice, but treats the three sublattices symmetrically, keeping two spins from each. (c) Seven spin plaquette for the triangular lattice which has the full rotational symmetry of the lattice, but breaks the symmetry between the three sublattices.

3.3.1 Square lattice

In order to apply the mean field formalism of App. A we need to tile the entire lattice with copies of the chosen plaquette, carefully distinguishing between *intra*plaquette and *inter*plaquette interactions. This tiling is not unique, but for the square lattice plaquette there is a natural choice which is shown in Fig. 3.5. Let us begin by ignoring the $RSOS$ constraint. Applying the formalism of App. A to the Hamiltonian (3.9), the single plaquette Hamiltonian corresponding to Fig. 3.5 is

$$\begin{aligned} \bar{\mathcal{H}}_0^{(4)} &= \frac{1}{2}K[(s_1-s_2)^2+(s_2-s_3)^2 \\ &+ (s_3-s_4)^2+(s_4-s_1)^2] \\ &+ \frac{1}{2}L[(s_1-s_3)^2+(s_2-s_4)^2] \\ &+ \tilde{h}_2[s_1^2+s_2^2+s_3^2+s_4^2], \end{aligned} \tag{3.10}$$

where $\tilde{h}_2 = h_2 + \lambda_1 K + \frac{3}{2}\lambda_2 L$, arises from multiplying out $(s_i - s_j)^2$ terms for i and j on different plaquettes. The interplaquette scale factors, λ_1 and λ_2, nominally equal to unity, have been introduced for later convenience. Interactions between plaquettes then involve only products of pairs of single spins, so we need only introduce fields, H_α, conjugate to the individual spins, σ_α, $\alpha = 1, 2, 3, 4$. Defining the single plaquette free energy, $\Phi^{(4)}\{H_\alpha\}$ via (A.5) we obtain the free energy functional

$$\begin{aligned} &\mathcal{F}^{(4)}\{H_{P\alpha};\sigma_{P\alpha}\} = \sum_P \Phi^{(4)}\{H_{P\alpha}\} \\ - &\sum_{P\alpha}(H_{P\alpha}+h_{P\alpha})\sigma_{P\alpha} \\ - &\lambda_1 K\sum_P(\sigma_{P1}\sigma_{P_1 4}+\sigma_{P2}\sigma_{P_1 3}+\sigma_{P2}\sigma_{P_3 1}+\sigma_{P3}\sigma_{P_3 4}) \\ - &\lambda_2 L\sum_P(\sigma_{P1}\sigma_{P_1 3}+\sigma_{P2}\sigma_{P_1 4}+\sigma_{P2}\sigma_{P_2 4} \\ + &\sigma_{P2}\sigma_{P_3 4}+\sigma_{P3}\sigma_{P_3 1}+\sigma_{P3}\sigma_{P_4 1}), \end{aligned} \tag{3.11}$$

where P_1, P_2, P_3 and P_4 are neighboring plaquettes to P (see Fig. 3.5), and $\Phi^{(4)}$ will be computed explicitly in Chapter 5. Since the ordered phases we seek are all either

ferromagnetic or antiferromagnetic we now take

$$\begin{aligned} h_{P1} &= h_{P3} \equiv h_A, \quad h_{P2} = h_{P4} \equiv h_B \\ H_{P1} &= H_{P3} \equiv H_A, \quad H_{P2} = H_{P4} \equiv H_B \\ \sigma_{P1} &= \sigma_{P3} \equiv M_A, \quad \sigma_{P2} = \sigma_{P4} \equiv M_B. \end{aligned} \tag{3.12}$$

The free energy per spin is then

$$\begin{aligned} &\frac{1}{N}\mathcal{F}^{(4)}(H_A, H_B; M_A, M_B) = \frac{1}{4}\Phi^{(4)}(H_A, H_B) \\ - \;& \frac{1}{2}(H_A + h_A)M_A - \frac{1}{2}(H_B + h_B)M_B \\ - \;& \lambda_1 K M_A M_B - \frac{3}{4}\lambda_2 L(M_A^2 + M_B^2). \end{aligned} \tag{3.13}$$

Differentiating with respect to M_A and M_B we obtain the first set of saddle point conditions [see the first line of (A.9)]

$$M_A = \frac{1}{2}\frac{\partial \Phi^{(4)}}{\partial H_A}, \quad M_B = \frac{1}{2}\frac{\partial \Phi^{(4)}}{\partial H_B}. \tag{3.14}$$

The mean field free energy per spin is finally obtained by substituting these relations into (3.13) [this intermediate form represents the Bogoliubov free energy – see (A.16)] and then minimizing over H_A and H_B. This is equivalent to solving the second set of saddle point equations [see the second line of (A.9)]

$$\begin{aligned} -H_A &= 2\lambda_1 K M_B + 3\lambda_2 L M_A + h_A \\ -H_B &= 2\lambda_1 K M_A + 3\lambda_2 L M_B + h_B, \end{aligned} \tag{3.15}$$

where, again, (3.14) should be substituted for the M_A and M_B dependence. We emphasize that the order is important here: the alternative of using (3.15) first to eliminate M_A and M_B often leads to a free energy in which the saddle point is not a minimum. It is also worth commenting that, as discussed in App. A, consistency of

the theory implies that the saddle point conditions guarantee that

$$M_A = \langle s_{P1} \rangle = \langle s_{P3} \rangle = -\frac{2}{N}\frac{\partial \mathcal{F}^{(4)}}{\partial h_A}$$
$$M_B = \langle s_{P2} \rangle = \langle s_{P4} \rangle = -\frac{2}{N}\frac{\partial \mathcal{F}^{(4)}}{\partial h_B}. \tag{3.16}$$

This allows one to follow the alternative route of *inverting* (3.14) to eliminate H_A and H_B in favor of M_A and M_B, and computing the *Helmholtz* free energy

$$\begin{aligned} \frac{1}{N}A^{(4)}(M_A, M_B) &= \frac{1}{N}\mathcal{F}^{(4)} + \frac{1}{2}(h_A M_A + h_B M_B) \\ = \; & \frac{1}{4}\bar{\Phi}(M_A, M_B) \\ - \; & \frac{1}{2}[H_A(M_A, M_B)M_A + H_B(M_A, M_B)M_B] \\ - \; & \lambda_1 K M_A M_B - \frac{3}{4}\lambda_2 L(M_A^2 + M_B^2), \end{aligned} \tag{3.17}$$

where $\bar{\Phi}^{(4)}(M_A, M_B)$ is obtained from $\Phi^{(4)}(H_A, H_B)$ through this elimination. The equilibrium magnetizations are then obtained via the equations of state

$$\frac{1}{2}h_A = \frac{1}{N}\frac{\partial A^{(4)}}{\partial M_A}, \quad \frac{1}{2}h_B = \frac{1}{N}\frac{\partial A^{(4)}}{\partial M_B}. \tag{3.18}$$

The advantage here is that $A^{(4)}$ is a *bona fide* mean field free energy depending *only* on the M variables, and we avoid the "mixed" representation containing all three sets of variables, h, H and M.

3.3.2 The *RSOS* condition

Let us now turn to the inclusion of the *RSOS* condition. Recall that this condition requires that nearest neighbor spins differ by at most one, implying a nearest neighbor interaction $v_R(s - s')$ such that

$$e^{-\beta v_R(s)} = \theta(1 - |s|), \tag{3.19}$$

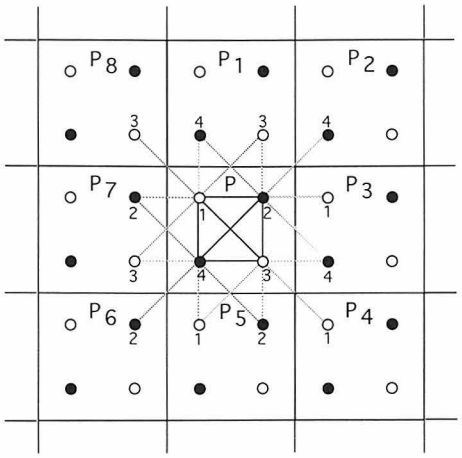

Figure 3.5: A natural tiling of the full square lattice by the four spin plaquette which maintains the symmetry of the lattice as well as the symmetry between the two sublattices.

where $\theta(x)$ is the step function [we take $\theta(0) = 1$]. The condition is crucial for stabilizing the bulk crystal surface when $K < 0$ since without it nearest neighbor column height differences would diverge. Within a plaquette, i.e. in the computation of Φ, this condition is easily accounted for simply by eliminating from the trace those spin configurations that violate it. However, between plaquettes greater care must be taken because one must now include the $RSOS$ condition explicitly in the interplaquette interaction term, $\mathcal{A}$, defined in (A.1). The difficulty lies in the fact that $v_R(s)$ is not simply expressible as a polynomial in s. For integer values of s, $v_R(s)$ is the large A limit of $v_A(s) \equiv As^2(s^2-1)$. This form leads to new interaction terms $s_i^2 s_j^2$ and $s_i^3 s_j$. Unfortunately, within the mean field approximation, the integer variable s is replaced by a continuous variable σ, and the fact that $v_A(s) \to -\infty$ as $A \to \infty$ for $0 < s^2 < 1$ leads to thermodynamic instabilities. The form $v_A(s) = As^2(s^2-1)^2$ is healthier in this regard, but now involves even higher powers of the spins and still unphysically restricts the continuous variable σ to the values $0, \pm 1$ when $A \to \infty$. One really needs $v_A(s) = A\theta(|s|-1)$, but this is nonpolynomial.

Our solution to this problem is to keep the $RSOS$ condition within a plaquette, but "soften" it between plaquettes. The condition's main role is to discourage large nearest neighbor column height differences, and its exact form is a matter of conve-

nience. We will consider then two "soft" forms for $v_R(s)$. Note that for $K > 0$ it is safe to simply take $v_R(s) \equiv 0$, but for sufficiently large $K < 0$ this choice becomes unstable to unbounded height differences between neighboring *plaquettes*. One solution then is to set $v_R(s) = (\lambda_1(K) - 1)Ks^2$ [effectively replacing K by $\lambda_1(K)K$ for all interplaquette interactions] with $0 < \lambda(K) \leq 1$ a smooth function of K which decreases as K becomes more negative, thereby *cancelling* at least part of the nearest neighbor interaction between plaquettes. At the same time one might *enhance* the interplaquette second neighbor coupling, replacing L by $\lambda_2(K)L$ with $\lambda_2(K) > 1$. This allows L to stabilize the reconstructed phase. It was precisely for this reason (as well as others – see below) that we introduced λ_1 and λ_2 in (3.11). Our second choice is to take $v_R(s) = As^4$, with fixed $A > 0$ of order unity chosen for convenience. This form guarantees thermodynamic stability without *ad hoc* variation of coefficients, at the expense of introducing higher powers of the spins. Unfortunately, it does allow ever larger nearest neighbor plaquette height differences as K becomes more negative, violating the expected equivalence of all plaquettes.

One is actually led to considering linear rescalings of the interplaquette interactions for other reasons. For example, the relative number of nearest neighbor and next neighbor bonds internal to the plaquette in Fig. 3.4(a) (namely 2:1) does not match the relative number in the full lattice (namely 1:1). One might therefore introduce phenomenological scale factors into the terms in (3.11) that couple to the environment, i.e. replace K by $\lambda_1 K$ and L by $\lambda_2 L$, and adjust λ_1 and λ_2 according to one's prejudice, or simply to optimize comparison with experiment.

It should now be clear how to write down spin-j Hamiltonians for arbitrary j, even $j \to \infty$. Keeping more layers should improve the accuracy of the approximation for thicker films. Similarly, the construction of the mean field theory is identical. The major differences are that the site free energy, Φ, becomes more complicated because there are more spin configurations to trace over.

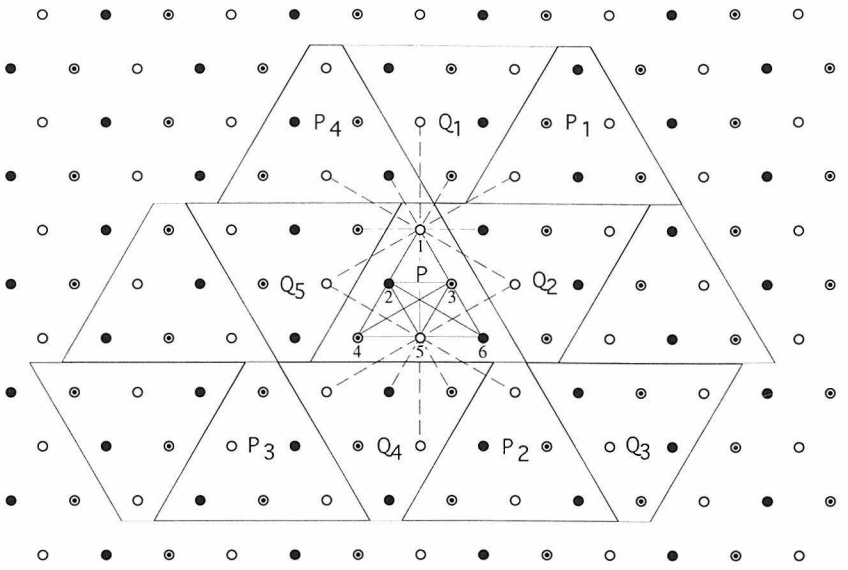

Figure 3.6: A possible tiling of the full triangular lattice by the six spin plaquette. Note that two different orientations of the original plaquette are required, and that the tiling is far from unique.

3.3.3 Triangular lattice

The second neighbor interaction divides the triangular lattice into three equivalent triangular sublattices, A, B and C. We consider mean field theories based on each of the two plaquettes of spins shown in Figs. 3.4(b) and 3.4(c). In the first, we keep two spins from each sublattice. In the second we keep a hexagonal plaquette of seven spins that contains the full rotational symmetry of the triangular lattice, but unfortunately does not treat the three sublattices symmetrically: three spins are kept from each of two of the sublattices, but ony one spin from the third. In neither case are all spins equivalent, which we will remedy somewhat by, again, introducing fudge factors, λ_i, that scale the couplings to the surroundings.

In principle, to distinguish the three sublattices, we need three magnetic fields, h_A, h_B and h_C, with corresponding sublattice magnetizations, M_A, M_B and M_C. However, since even with negative K frustration dictates that there are no phases that spontaneously break the symmetry between the three sublattices, we will keep only one field, h, and assume the sublattice magnetizations to have all the same value, M. Note that this is a statement about the exact behavior of the model. The mean

field approximation may well predict unphysical phases with broken symmetry. For this reason we will restrict triangular lattice computations to $K > 0$. In discussing the effects of reconstructed phases we will always use a square lattice.

In order to apply the formalism of App. A we must again tile the plane with the basic plaquette. If one remains completely faithful to the triangular lattice, this turns out to be very unnatural. Examples of tilings are shown in Figs. 3.6 and Fig. 3.7. The hexagonal tiling maintains the rotational symmetry of the lattice, but has a "chirality," and therefore breaks the inversion symmetry. The triangular tiling is clearly highly nonunique, requires two different orientations of the basic plaquette, and breaks the rotational symmetry of the lattice more badly than does the triangle itself. The nonuniqueness reflects itself in the differing identifications of interplaquette and intraplaquette interactions implied by each possible tiling. For example, the symmetry of the triangle would normally imply equivalency of the three corner sites and equivalency of the three noncorner sites. However, in the tiling shown in Fig. 3.6 the top corner site connects to four different plaquettes through nearest neighbor bonds, while the right and left corner sites connect to three and to two different plaquettes, respectively. All six sites are therefore distinguishable and will have potentially different order parameter values. This is not only inconvenient for eventually solving the mean field equations, but may also give rise to unphysical reconstructed phases. It seems clear that this will be true for any tiling with this plaquette.

Only by distorting the triangular lattice somewhat can one preserve the full symmetries of the plaquettes in the tiling: see Figs. 3.8 and 3.9. The drawback is that identifying second neighbors becomes ambiguous (see below). In particular, there is no way to preserve both the rotational symmetry and the property that second neighbor bonds join sites only on the same sublattice. Notice in any case that both in Figs. 3.6, 3.7 and in Figs. 3.8, 3.9, that different tiles contain different orientations of the sublattices A, B and C, so any reconstructed phase that is uniform on each sublattice will not have the same periodicity as the tiling. A different choice of six spin plaquette, say, would have to made to respect this periodicity (for example a

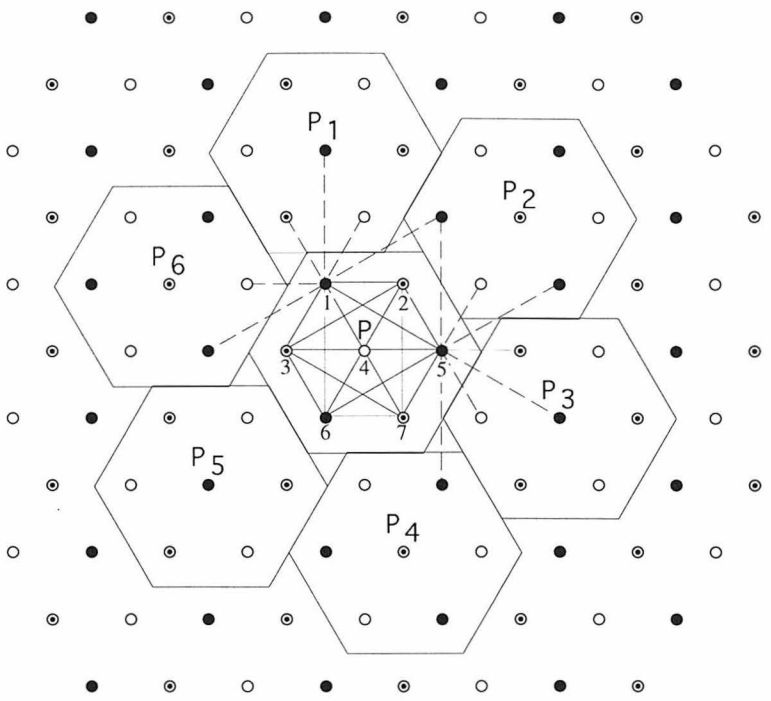

Figure 3.7: A possible tiling of the full triangular lattice by the seven spin plaquette. Other possible tilings differ only by translation or mirror reflection.

parallelogram of two rows of three spins), but such a choice would generally violate the rotational symmetry even further. Since we work only in the mean field approximation and with ferromagnetic interactions we feel that maintainance of qualitative symmetries is more important than that of quantitative details of interactions. In any case, our hope is that the basic physics should be dominated by the interactions within the plaquette, which are treated exactly. We emphasize that we go through all this trouble of embedding the plaquette in a real lattice only to ensure that we obtain a fully consistent mean field theory (see App. A and discussions therein).

Keeping the above physical considerations in mind, we now write down the appropriate free energies. Detailed expressions and comparisons of the expressions obtained from the distorted and undistorted lattices are contained in App. B. Here we exhibit only the simplified expressions valid in the unreconstructed phases.

First, the single plaquette Hamiltonian corresponding to Fig. 3.4(b) is given by

$$\bar{\mathcal{H}}_0^{(6)} = \frac{1}{2}K[(s_1 - s_2)^2 + (s_2 - s_4)^2 + (s_4 - s_5)^2$$

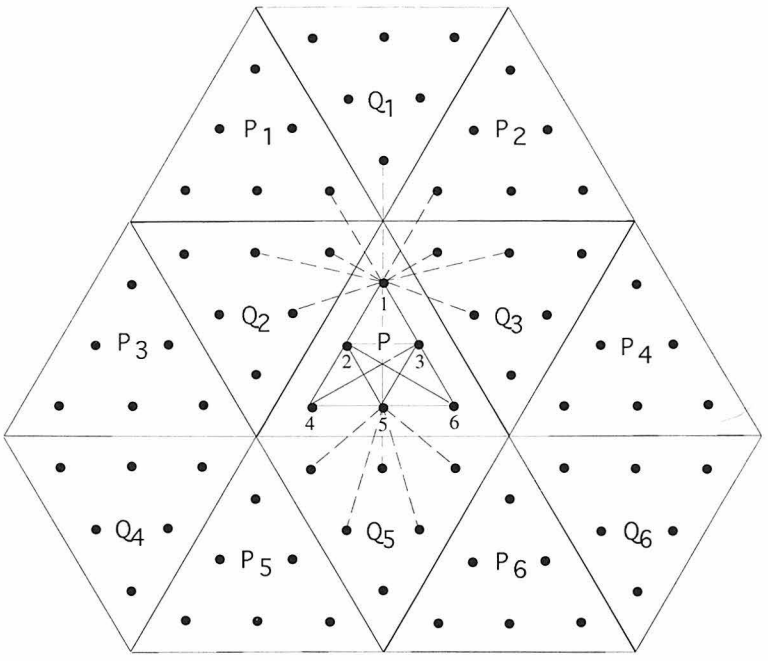

Figure 3.8: A more symmetric tiling of a distorted triangular lattice by the six spin plaquette. Two different orientations of the original plaquette are still required, but the tiling is unique up to translations. Choice of second neighbor interactions becomes ambiguous, but unreconstructed phases should not be sensitive to this.

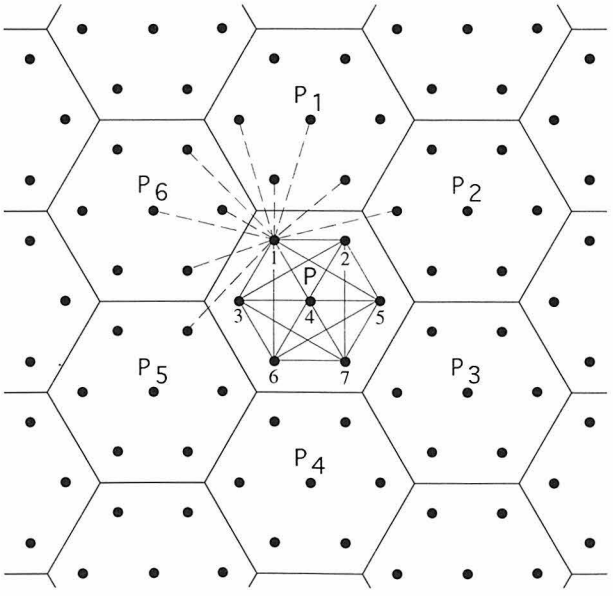

Figure 3.9: A more symmetric tiling of a distorted triangular lattice by the seven spin plaquette. The tiling is unique up to translations. Choice of second neighbor interactions becomes ambiguous, but unreconstructed phases should not be sensitive to this.

$$
\begin{aligned}
&+ \quad (s_5 - s_6)^2 + (s_3 - s_6)^2 + (s_1 - s_3)^2 \\
&+ \quad (s_2 - s_3)^2 + (s_3 - s_5)^2 + (s_2 - s_5)^2] \\
&+ \quad \frac{1}{2} L[(s_1 - s_5)^2 + (s_2 - s_6)^2 + (s_3 - s_4)^2] \\
&+ \quad \tilde{h}_2^{out}[s_1^2 + s_4^2 + s_6^2] + \tilde{h}_2^{in}[s_2^2 + s_3^2 + s_5^2], \qquad (3.20)
\end{aligned}
$$

where $\tilde{h}_2^{out} = h_2 + 2\lambda_1 K + \frac{5}{2}\lambda_2 L$ and $h_2^{in} = h_2 + \lambda_1 K + \frac{5}{2}\lambda_2 L$. The scale factors, λ_1 and λ_2, have again been introduced for later convenience. Let $\Phi^{(6)}$ be the plaquette free energy defined in (A.1) (to be computed explicitly in Chapter 5). Ignoring once again the $RSOS$ condition between plaquettes, the free energy functional corresponding to Fig. 3.8 is then (see App. B)

$$
\begin{aligned}
&\frac{1}{N}\mathcal{F}^{(6)}(H_{in}, H_{out}; M_{in}, M_{out}) = \frac{1}{6}\Phi^{(6)}(H_{in}, H_{out}) \\
- \quad &\frac{1}{2}[(H_{out} + h)M_{out} + (H_{in} + h)M_{in}] \\
- \quad &\frac{1}{2}\lambda_1 K(3M_{out}^2 + M_{in}^2 + 2M_{in}M_{out}) \\
- \quad &\lambda_2 L(M_{out}^2 + M_{in}^2 + 3M_{in}M_{out}). \qquad (3.21)
\end{aligned}
$$

Here M_{out} is the magnetization on the three corner sites of the plaquette, while M_{in} is the magnetization on the three edge sites. Except for very special values of λ_1 and λ_2 the two will in general be different in the mean field approximation. The same considerations apply to the fields H_{out} and H_{in}.

Similarly, the plaquette Hamiltonian corresponding to the hexagonal plaquette in Fig. 3.4(c) is given by

$$
\begin{aligned}
\bar{\mathcal{H}}_0^{(7)} \quad = \quad &\frac{1}{2} K[(s_1 - s_2)^2 + (s_2 - s_5)^2 + (s_5 - s_7)^2 \\
&+ \quad (s_7 - s_6)^2 + (s_6 - s_3)^2 + (s_3 - s_1)^2 \\
&+ \quad (s_1 - s_4)^2 + (s_2 - s_4)^2 \\
&+ \quad (s_3 - s_4)^2 + (s_5 - s_4)^2 + (s_6 - s_4)^2 + (s_7 - s_4)^2] \\
&+ \quad \frac{1}{2} L[(s_1 - s_6)^2 + (s_1 - s_5)^2 + (s_2 - s_6)^2 \\
&+ \quad (s_5 - s_6)^2 + (s_3 - s_7)^2]
\end{aligned}
$$

$$+ \quad \tilde{h}_2^{out}[s_1^2 + s_2^2 + s_3^2 + s_5^2 + s_6^2 + s_7^2] + \tilde{h}_2^{in} s_4^2, \tag{3.22}$$

where $\tilde{h}_2^{out} = h_2 + \frac{3}{2}\lambda_1 K + 2\lambda_2 L$ and $\tilde{h}_2^{in} = h_2 + 3\lambda_2 L$. If $\Phi^{(7)}$ is the corresponding plaquette free energy, the mean field free energy corresponding to Fig. 3.9 is then (see App. B)

$$\begin{aligned} \tfrac{1}{N} \quad & \mathcal{F}^{(7)}(H_{in}, H_{out}; M_{in}, M_{out}) = \frac{1}{7}\Phi^{(7)}(H_{in}, H_{out}) \\ - \quad & \frac{1}{7}[6(H_{out} + h)M_{out} + (H_{in} + h)M_{in}] \\ - \quad & \frac{9}{7}(\lambda_1 K + \lambda_2 L)M_{out}^2 - \frac{6}{7}\lambda_2 L M_{in} M_{out}. \end{aligned} \tag{3.23}$$

Here M_{out} is the magnetization on the outer ring of sites, while M_{in} is the magnetization on the inner site. Fields H_{in} and H_{out} are defined similarly.

Chapter 4 Sine-Gordon phenomenology: first order preroughening and zippering

In this chapter we develop a general, large length-scale "hydrodynamic" theory of the layering phase diagram. This will serve as a rigorous guide to the different classes of behavior available to the system. A full microscopic calculation is still required to determine the behavior of any given model. The plaquette mean field formalism will be applied to this end in later chapters.

The basic idea we exploit is that roughening and preroughening are large scale phenomena, governed by only a few renormalized parameters. The small scale structure of the surface (be it locally disordered, flat, or possibly even reconstructed) feeds into these parameters, but is otherwise irrelevant to the large scale behavior. Of course, a phase transition in the local structure could preempt the onset of long range roughening or preroughening correlations (for example, it might induce some kind of critical endpoint with the roughening or preroughening line then ending on a first order line), but we assume this not to be the case. Imagine, then, that the system is close to a roughening or preroughening transition so that the correlation length is very large. The way we would formally derive the large scale theory is to perform some kind of renormalization group transformation on the Hamiltonian of the system, iterating it until we enter the neighborhood of the fixed point that governs the transition. If we are not precisely at criticality, further iteration will move the Hamiltonian away from the fixed point once more, but along a very restricted set of paths. The point is that during the approach to the fixed point all irrelevant variables have decayed away. Only one (or perhaps two, as we shall see) relevant variables remain, and it is their eventual growth that moves the Hamiltonian away from the fixed point. However the dimension of this "escape manifold" is just the number of relevant variables. If we then stop the renormalization process on some

matching boundary, not too far from the fixed point, we may parameterize the final theory with these one or two renormalized variables.

4.1 Sine-Gordon-type models

In many problems the detailed analysis of the fixed point region cannot be performed explicitly. The advantage in the present case is that this region may be characterized simply and completely by a sine-Gordon type model:

$$\bar{\mathcal{H}}_{SG} = \int d^2r \left\{ \frac{1}{2} K_0 |\nabla h(\mathbf{r})|^2 + V_0[h(\mathbf{r})] \right\} \tag{4.1}$$

with

$$V_0[h] = -y_0 \cos[2\pi h(\mathbf{r})] - u_0 \cos[4\pi h(\mathbf{r})] + V_{sub}[h(\mathbf{r})], \tag{4.2}$$

where $h(\mathbf{r})$ represents a coarse grained *continuous* surface height field, K_0 is a partially renormalized surface stiffness, y_0 represents the the fundamental Fourier component of the partially renormalized atomic periodic modulation, u_0 the next harmonic, and $V_{sub}[h]$ is a partially renormalized substrate potential. The fixed point is actually a fixed line on which only K_0 is nonzero, and the critical behavior has already been alluded to in (1.2). As we will discuss in detail below, for pure Kosterlitz-Thouless roughening we may set $u_0 = 0$, but in order to discuss preroughening we must sometimes keep $u_0 \neq 0$ [4]. All higher harmonics, however, are irrelevant and may be assumed to have decayed to zero in the neighborhood of the fixed line. The substrate potential grows steeper under renormalization, and the form (4.1) is valid only in the thick film limit where $V[h]$ is extremely weak, so that the partially renormalized $V_0(h)$ is weak as well. Since $V[h]$ has power law behavior (3.2) for large h, $V_0[h]$ will as well. The quadratic form,

$$V_{sub}[h] \approx \frac{1}{2} \kappa_0 [h - h_0(\Delta\mu)]^2, \; h \ll h_0(\Delta\mu), \tag{4.3}$$

[see also (3.4)] with a renormalized curvature, κ_0, suffices for thick films. Huse [61] has written down general functional recursion relations for any potential, $V_0[h]$, and treated in detail the case $u_0 = 0$, i.e. the interplay between roughening and layering. Here we will extend key parts of that analysis to the preroughening regime, $u_0 \neq 0$. It will transpire that $u_0 > 0$ and $u_0 < 0$ can yield very different behaviors, and this gives rise to very interesting physics in the layering phase diagram.

To formalize what we have said so far we write down the renormalization group recursion relations for the Hamiltonian (4.1) [61]:

$$\begin{aligned}
\frac{dK}{dl} &= \kappa^2/2K\Lambda^4 + (4\pi^4/K\Lambda^4)y^2 + (64\pi^4/K\Lambda^4)u^2 \\
\frac{dy}{dl} &= (2 - \pi/K)y + (4\pi^2/K\Lambda^2)yu \\
\frac{du}{dl} &= (2 - 4\pi/K)u - (\pi^2/K\Lambda^2)y^2 \\
\frac{d\kappa}{dl} &= 2\kappa - \kappa^2/K\Lambda^2. \qquad (4.4)
\end{aligned}$$

where $\Lambda \sim \frac{\pi}{a}$ is the (nonuniversal) momentum space cutoff due to the lattice. The flow parameter, l, is related to the spatial rescaling factor b via $b = b_0 e^l$, where b_0 is the initial rescaling factor required to enter the neighborhood of the fixed line and is assumed to depend smoothly on the parameters of the initial $RSOS$ model, say. The recursion relations are valid for small y, u and κ and we have the initial conditions $K(l = 0) = K_0$, $y(l = 0) = y_0$, $u(l = 0) = u_0$ and $\kappa(l = 0) = \kappa_0$, which are assume to lie on some trajectory *incoming* toward the fixed line.

4.2 Roughening and preroughening

Let us now consider the various possible behaviors as a function of initial condition. Consider first the substrate free case, $\kappa_0 = 0$. For small enough K_0 ($K_0 \lesssim \pi/2$ for small y and u) both y and u flow to zero as $l \to \infty$, while the stiffness $K(l) \to K_R(K_0)$, its fully renormalized value which then appears in (1.2). This corresponds to the rough phase.

For intermediate values of K_0 ($\pi/2 \lesssim K_0 \lesssim 2\pi$ for small y and u) $u(l)$ still flows to zero, and may be ignored, but if $y_0 \neq 0$, $y(l)$ eventually begins to grow again, as does $K(l)$. The strengthening corrugation potential, and increasing surface stiffness, signal the onset of a flat phase. Notice that if $y_0 > 0$ the minima of the corrugation potential occur at integer h, while if $y_0 < 0$ they occur at half-integer h. Since $y_0(J_1, J_2, T)$ is a renormalized parameter we may, in fact, imagine that as a result of short scale fluctuations it might *change sign*. The minima then switch abruptly from integer to half-integer. This precisely describes the physics of preroughening, with the preroughening critical line corresponding to $y_0(T) = 0$ [4]. The sign reversal is driven precisely by the entropy of small scale roughness discussed in previous chapters. As we shall see below, a negative value of y_0 could also be associated with a *reconstructed* surface, which may also roughen while maintaining a form of long range reconstructed order. The sine-Gordon Hamiltonian does not distinguish between these two cases, though the dependence of the partially renormalized parameters on the original model parameters would of course be different (possibly even singular if a surface reconstruction transition takes place). For $y_0 = 0$ the fixed line is again stable, and we will have $u(l) \to 0$ and $K(l) \to K_R$, with $\pi/2 < K_R < 2\pi$. The critical surface is therefore *rough*, but with a *larger* renormalized stiffness than is generically possible: the short range fluctuations have renormalized away the strongest Fourier component of the corrugation potential.

Finally, for even larger K_0 ($K_0 \gtrsim 2\pi$ for small y and u) both y and u are relevant, so even if $y_0 = 0$ the second harmonic of the corrugation potential will grow and the surface will flatten. Notice then that there are twice as many minima. This will be discussed in detail below. In principle, if we had a second free parameter at our disposal, we might imagine that both y_0 and u_0 could be made to vanish. Flattening would then take place only when the *third* harmonic became relevant, i.e. for $K_0 > 9\pi/2$. This situation, however, does not seem to be experimentally relevant [1]

If y_0 is not precisely zero then both u and y will grow under renormalization,

[1] Generally, the rigorous statement is that if the pth one is the first nonvanishing Fourier component, the surface will be rough for $K_R = \lim_{l\to\infty} K(l) < \pi p^2/2$. Generically this will only happen if one has $p-1$ control variables to tune.

and the interesting question then arises of how the two Fourier components might constructively or deconstructively interfere in the final renormalized corrugation potential. We shall explore these effects in detail below, seeing that they have very strong effects on both the surface and layering phase diagrams.

4.3 Roughening and layering

Since u is strongly irrelevant for $K_0 \lesssim 2\pi$, the asymptotic behavior in the roughening and preroughening regions may be addressed simply by setting $u = 0$ in the recursion relations, (4.4). The usual roughening transition may then be described by studying the region where the starting manifold, $(y_0(T), K_0(T))$, crosses the critical trajectory into the fixed point at $y = 0$, $K = \pi/2$. For small y and $\lambda \equiv 2 - \pi/K$ this trajectory is defined by $\lambda = \tilde{y}$, where $\tilde{y} \equiv (4\sqrt{2}\pi/\Lambda^2)y$. Correct to quadratic order in λ and $\tilde{y}$, the recursion relations simplify to

$$\frac{d\kappa}{dl} = 2\kappa; \quad \frac{d\lambda}{dl} = \tilde{y}^2; \quad \frac{d\tilde{y}}{dl} = \lambda\tilde{y}. \tag{4.5}$$

The flows generated by these equations are shown in Fig. 4.1. By integrating the flows in region II of this figure, from the starting manifold to some noncritical matching manifold, for example $\lambda = \lambda_f > 0$, Huse [61] has shown that the Ising layering critical points, $T_{c,n}$, approach the bulk roughening temperature, T_r, from below asymptotically as

$$T_r - T_{c,n} \propto \frac{4\pi^2}{(2+\alpha)^2 \ln^2(n/\tilde{n})} \tag{4.6}$$

where α, defined below (3.2), describes the power law tail of the substrate potential, $\tilde{n}$ is a nonuniversal amplitude determined by the strength of the substrate potential, and the overall constant of proportionality depends on the detailed mapping of the original model onto the sine-Gordon model.

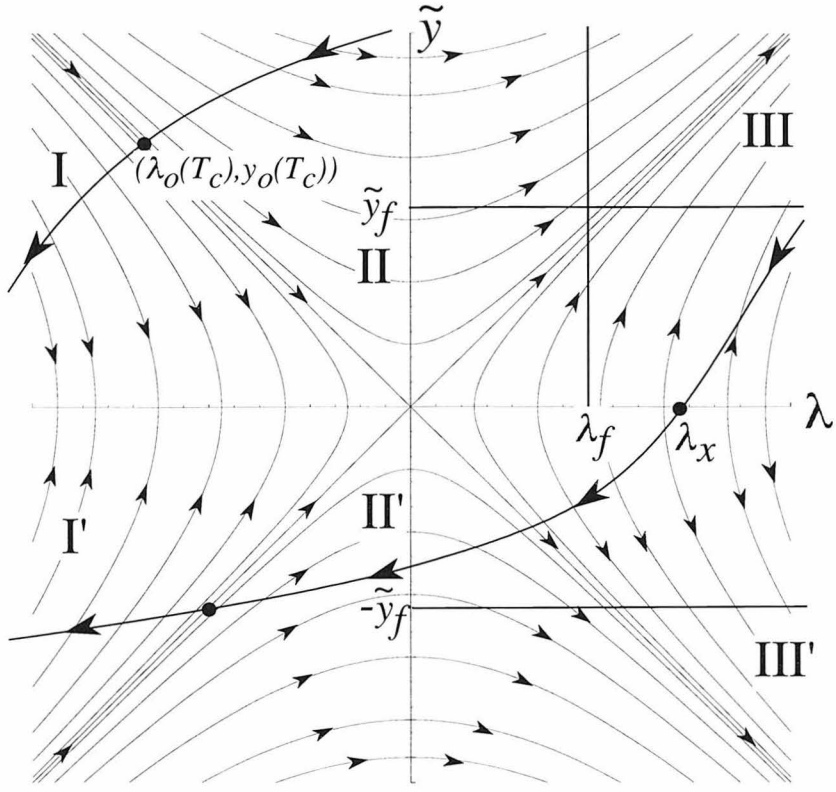

Figure 4.1: Renormalization group flows generated by equations (4.5). Regions I, II and III are bounded by the two separatrices that flow into and out of the Kosterlitz-Thouless fixed point at $\tilde{y} = \lambda = 0$. The thicker two flow lines represent possible trajectories of the system as temperature is varied. The path on the upper left corresponds to conventional roughening, while the path on the right represents preroughening (at the point $(\lambda_x, 0)$) followed by roughening. The solid lines drawn at $\lambda = \lambda_f$ and $\tilde{y} = \tilde{y}_f$ represent two possible noncritical manifolds at which the renormalization flows can be stopped.

4.4 Preroughening and reentrant layering

Preroughening, on the other hand, corresponds to the rather different situation in which the starting manifold begins in region III of Fig. 4.1. As the temperature rises the manifold *crosses* $\tilde{y} = 0$ into region III′ at some positive value λ_0 of λ. Precisely at $\tilde{y} = 0$ the system is on the fixed line and the interface is rough. On either side of $\tilde{y} = 0$ the renormalization group trajectories move away from the fixed line into an ordered phase. As before, region III corresponds to the flat phase. Region III′ corresponds to the DOF phase. Since $\tilde{y} < 0$ in the DOF phase, the minima in the corrugation potential occur at half-integer h. The fractional filling, θ, of the top layer of the interface then jumps discontinuously from $\theta = 0$ to $\theta = \frac{1}{2}$ at preroughening. As the temperature continues to rise, the trajectory eventually crosses into region II′ and then into region I′. The latter corresponds to the transition from the DOF to the rough phase. In the presence of a substrate potential regions II′ and III′ give rise to first order layering transitions between half-integer coverages. The Huse [61] computation for the critical points goes through in exactly the same way and leads once again to (4.6) for the $T_{c,n}$ [see Fig. 2.1(c)].

The effect of the substrate on preroughening is quite different. The bulk critical behavior is now determined by the rate at which flows are pushed away from the fixed line for small $\tilde{y}$. This is completely determined by the value, λ_X, at which the starting manifold crosses the $\tilde{y} = 0$ axis. In particular, $\tilde{y}$ itself now plays the role of the deviation from criticality, the Kosterlitz-Thouless fixed point no longer plays any role, and the flows are completely confined to regions III and III′. The solutions to the flow equations in these regions are given by

$$\begin{aligned} \kappa(l) &= \kappa_0 e^{2l} \\ \tilde{y}(l) &= -\mathrm{sgn}(\tilde{y}_0) B_0 \mathrm{csch}(B_0 l + \phi_0) \\ \lambda(l) &= -B_0 \coth(B_0 l + \phi_0), \end{aligned} \tag{4.7}$$

where

$$\begin{aligned} B_0^2 &= \lambda_0^2 - \tilde{y}_0^2 = \lambda(l)^2 - \tilde{y}(l)^2 > 0 \\ \phi_0 &= \frac{1}{2}\ln\left(\frac{\lambda_0 - B_0}{\lambda_0 + B_0}\right) < 0. \end{aligned} \tag{4.8}$$

We run the flows until $|\tilde{y}(l)| = \tilde{y}_f$, some fixed value. The corresponding value l_f of l is then

$$\begin{aligned} l_f &= -\frac{1}{B_0}\sinh^{-1}(B_0/\tilde{y}_f) - \frac{\phi_0}{B_0} \\ &\approx -\frac{1}{\lambda_X}\sinh^{-1}(\lambda_X/\tilde{y}_f) - \frac{1}{\lambda_X}\ln(|\tilde{y}_0|/\lambda_X), \end{aligned} \tag{4.9}$$

where the second line is valid for $\tilde{y}_0 \ll \lambda_0$. At this point we have

$$\lambda_f \equiv \lambda(l_f) = \sqrt{B_0^2 + \tilde{y}_f^2} \approx \sqrt{\lambda_X^2 + \tilde{y}_f^2}. \tag{4.10}$$

Following Huse [61], for given values of $\tilde{y}$ and λ, there will be a critical value of $\kappa = \kappa_c(\tilde{y}, \lambda)$ at which the Ising layering critical point occurs. Let us define

$$\kappa_c^{\pm}(\lambda_X) = \kappa_c(\pm\tilde{y}_f, \sqrt{\lambda_X^2 + \tilde{y}_f^2}). \tag{4.11}$$

Then, as $\tilde{y} \to 0$, we locate the value of κ_0 at which the critical point occurs by demanding that

$$\kappa_c(\pm\tilde{y}_f, \lambda_f) \approx \kappa_c^{\pm}(\lambda_X) = \kappa_0 e^{2l_f}, \ \pm\tilde{y}_0 > 0, \tag{4.12}$$

which yields

$$\kappa_0 \approx \tilde{\kappa}^{\pm}(\lambda_X)(|\tilde{y}_0|/2\lambda_X)^{2/\lambda_X} \tag{4.13}$$

where

$$\tilde{\kappa}^{\pm}(\lambda_X) \equiv \kappa_c^{\pm}(\lambda_X) e^{\frac{2}{\lambda_X}\sinh^{-1}(\lambda_X/\tilde{y}_f)}. \tag{4.14}$$

Finally, from (3.3) for a van der Waals substrate we have $\kappa_0 = \alpha(\alpha+1)c/h_0(\Delta\mu)^{2+\alpha}$, with the nth layering line corresponding to $h_0(\Delta\mu) = n - \frac{1}{2}$ for $\tilde{y}_0 > 0$ and to

$h_0(\Delta\mu) = n$ for $\tilde{y}_0 < 0$ (i.e. exact degeneracy of two neighboring minima in the renormalized corrugation potential). This yields immediately [see Fig. 2.1(c)]

$$\begin{aligned} T_{pr} - T_n^1 &\propto \tilde{y}_0 \approx 2\lambda_0(\tilde{n}^+/n)^{(2+\alpha)\lambda_0/2}, \quad \tilde{y}_0 > 0 \\ T_n^2 - T_{pr} &\propto -\tilde{y}_0 \approx 2\lambda_0(\tilde{n}^-/n)^{(2+\alpha)\lambda_0/2}, \quad \tilde{y}_0 < 0 \end{aligned} \tag{4.15}$$

where $\tilde{n}^{\pm}(\lambda_X) = [\alpha(\alpha+1)c/\tilde{\kappa}^{\pm}(\lambda_X)]^{1/(2+\alpha)}$ is a nonuniversal amplitude. Once again the overall constants of proportionality are determined by the detailed mapping of the original model onto the sine-Gordon model. We see then that the critical points have a power law rather than logarithmic approach the preroughening point. The power is nonuniversal, depending on λ_X, and vanishes as the Kosterlitz-Thouless point is approached. We have therefore established Fig. 2.1(c) as the correct thick film layering phase diagram corresponding to a preroughening trajectory such as that shown in Fig. 4.1.

4.5 Recursion relations when u is relevant

We have seen that the experimental phase diagrams for Argon and Krypton on graphite show rather different behavior, with apparent first order lines that "zip" the integer and half-integer layering lines together. It is possible that these transitions arise from some confluence of preroughening and two-dimensional melting phenomena, where the melting and preroughening temperatures are nearly the same. This is certainly true in the first two layers where two dimensional triple points are observed [52, 53]. However it seems an unlikely coincidence that such a confluence would survive, as seen, to much thicker films, where the energetics of melting and preroughening ought to be distinct. Here we offer a much simpler and more natural explanation, phrased entirely within the physics of the sine-Gordon model. More detailed comparisons between theory and experiment will made in Chapter 6

The idea now is to consider values of K_0 in the region where u becomes relevant. Typically, u will be of order unity in the original model, so if K_0 is significantly larger

than 2π then even when $y \equiv 0$ the renormalization group flows will never come close to the fixed line, and there will be no simple analytic description of the behavior. We therefore assume that K_0 is sufficiently close to 2π that, in the absence of y, u_0 may be assumed small. Defining $\bar{y} = \sqrt{2}\pi y/\Lambda^2$, $\bar{u} = 4\sqrt{2}\pi u/\Lambda^2$ and $\mu = 2 - 4\pi/K$, correct to quadratic order in these variables the recursion relations (4.4) simplify to

$$\begin{aligned}
\frac{d\kappa}{dl} &= 2\kappa \\
\frac{d\bar{y}}{dl} &= \frac{3}{2}\bar{y} + \frac{1}{4}\mu\bar{y} + \frac{\sqrt{2}}{4}\bar{u}\bar{y} \\
\frac{d\mu}{dl} &= \bar{y}^2 + \bar{u}^2 \\
\frac{d\bar{u}}{dl} &= \mu\bar{u} - \sqrt{2}\bar{y}^2.
\end{aligned} \tag{4.16}$$

If $\bar{y}_0 \ll u_0$ these further simplify to

$$\frac{d\kappa}{dl} = 2\kappa; \quad \frac{d\mu}{dl} = \bar{u}^2; \quad \frac{d\bar{u}}{dl} = \mu\bar{u}; \quad \frac{d\bar{y}}{dl} = \frac{3}{2}\bar{y}; \tag{4.17}$$

the first three of which are identical to (4.4) with μ replacing λ and $\bar{u}$ replacing $\tilde{y}$. The solutions, in the equivalent to region II, are

$$\begin{aligned}
\kappa(l) &= \kappa_0 e^{2l}; \quad y(l) = y_0 e^{\frac{3}{2}l} \\
\bar{u}(l) &= A_0 \sec(A_0 l + \theta_0); \quad \mu(l) = A_0 \tan(A_0 l + \theta_0)
\end{aligned} \tag{4.18}$$

with $A_0^2 = \bar{u}_0^2 - \mu^2 > 0$ and $\theta_0 = tan^{-1}(\mu_0/A_0)$. These solutions hold up until $\bar{y} \approx \bar{u}$. In the absence of $\bar{y}_0$ we would integrate these equations until $\mu = \mu(l_f^0) \equiv \mu_f^0 > 0$ [and $|\bar{u}(l_f^0)| = \bar{u}_f^0$ where $(\bar{u}_f^0)^2 = A_0^2 + (\mu_f^0)^2$] reaches some final value [just as in Huse's analysis of (4.5)]. If $\bar{y}_0$ were to remain zero for all μ_0 (or, equivalently, K_0), we would then predict, as a function of μ_0, first order layering lines terminating in Ising critical points *every half layer*. However, since $\bar{y}_0$ vanishes only at the putative preroughening point, we conclude that there is only a single value of μ_0 at which this analysis is correct. Since we assume the model to be in region II, rather than region I, the bulk interface would be in the flat phase. In thick films we would therefore

observe first order transitions every half layer, with Ising critical points observed only, perhaps, for an initial finite set of layers (the closer the initial values to the incoming separatrix, the greater the number of critical points).

What happens away from this value of μ_0 depends upon the growth of y_0 under renormalization. If y_0 is so small that $\bar{y}_f^0 \equiv \bar{y}_0 \exp(\frac{3}{2} l_f^0) \ll \bar{u}_f^0$, then we may still use (4.18), and stop integrating at l_f^0 as before. Thus, as y_0 passes through zero, the contribution, y_f^0, of the lowest harmonic to the corrugation potential is linear in y_0. If, however, $\bar{y}_f^0 \gtrsim \bar{u}_f$ then we should stop integrating at l_f such that $\bar{y}(l_f) \equiv \bar{y}_f \approx \mu_f^0$, say, some final value. There is then a regime in the integration where $\bar{y}(l) \gtrsim \bar{u}(l)$, and the solutions (4.18) are no longer valid. If $\bar{u}(l)$ is not too much smaller than $\bar{y}_f$ we may use the fact that $\bar{y}$ is rapidly varying relative to $\bar{u}$ and μ. Thus in the time it takes $\bar{y}(l)$ to go from $\bar{u}(l)$ to y_f it is easy to see that $\bar{u}(l)$ and $\mu(l)$ change only by $O(y_f^2)$, which we assume to be much smaller than $\bar{u}(l)$. Thus $\bar{u}_f$ and μ_f are essentially the unperturbed values of μ and $\bar{u}$ at which $y(l)$ "crosses" $\bar{u}(l)$. If, on the other hand, $\bar{u}(l)$ and $\mu(l)$ are very small compared to $\bar{y}_f$, then we may essentially delete all but $\bar{y}(l)$ from the right hand sides of (4.16): the flows are driven entirely by $\bar{y}(l)$. The final values, $\bar{u}_f$ and $\bar{\mu}_f$, are then of order $y_f^2 << y_f$.

To summarize, then, we are interested in the final renormalized form of the corrugation potential. The above analysis shows that for small $\bar{y}_0$, the amplitude of the fundamental Fourier component varies linearly with $\bar{y}_0$ and changes sign precisely when $\bar{y}_0$ does, while the amplitude of the second harmonic can be taken as fixed. For larger $\bar{y}_0$, the ratio of the amplitudes, $\bar{y}_f/\bar{u}_f$, is nonlinear, but monotonically increasing in $\bar{y}_0$. This is all we need to know for the purposes of the following analysis.

4.6 Thermodynamics of the bulk interface when u is relevant

Now that we have understood the general structure of the fully renormalized Hamiltonian, we must understand its thermodynamics. We are in a regime in which the

corrugation potential wins out over thermal fluctuations, leading to a flat phase in which the interface height sits at a minimum of the potential. Since thermal fluctuations have not been completely integrated out [$K_f = 4\pi/(2-\mu_f)$ is still finite – this was necessitated by the restricted regime in which the flow equations are valid] this is not entirely accurate: the interface still has fluctuations about this minimum. Since K_f is large, however, these fluctuations may be taken as small (so long as one is not too close to any second order phase transition – see further below), leading to some slight renormalization of the corrugation potential, but not altering its basic form. Including the substrate potential, we therefore arrive, essentially rigorously, at the following single variable free energy functional which completely determines the thermodynamics:

$$f[h] = -y_R \cos(2\pi h) - u_R \cos(4\pi h) + \frac{1}{2}\kappa_R (h - h_0)^2, \tag{4.19}$$

where the absolute minimum of $f(h)$ determines the equilibrium average interface height, and y_R and u_R are mildly renormalized versions of $y_f \equiv (\Lambda^2/\sqrt{2}\pi)\bar{y}_f$ and $u_f \equiv (\Lambda^2/4\sqrt{2}\pi)\bar{u}_f$ into which K_f has been completely subsumed. Similarly for $\kappa_R \approx \kappa_f \equiv \kappa_0 \exp(2l_f)$, where we assume that κ_0 is sufficiently small that l_f is set only by the bulk interface recursion relations. This means, for example, that κ_R is linearly related to κ_0. We reiterate that the validity of this free energy presumes that the essential physics lies only in the large scale, coarse grained fluctuations. It is also possible that small scale energetics of the original model preempt this physics at some temperature, beyond which (4.19), and the entire sine-Gordon analysis, fails (see further below). The control variable is y_R, which switches sign, while u_R may be taken as fixed and nonzero, but either positive or negative.

4.6.1 $u_R > 0$: first order preroughening and zippering

Begin with the bulk interface, $\kappa_R \equiv 0$. Suppose first that $u_R > 0$, and imagine beginning with $y_R \gg u_R$, then decreasing y_R through zero, and ending with $y_R \ll -u_R$. The evolution of the corrugation potential is shown in Fig. 4.2(a). We see that

when $y_R = 4u_R$ local minima develop at half-integer h. Since these local minima are not absolute minima, the surface height remains an integer. As y_R decreases these local minima decrease, and precisely at $y_R = 0$ they become degenerate with the integer minima. For $y_R < 0$ the half integer minima lie *below* the integer minima, and therefore define the equilibrium surface height. We therefore have a *first order transition* from the flat to the DOF phase. The preroughening line therefore has a tricritical point precisely where the fully renormalized stiffness reaches 2π.

For clarity, this picture is contrasted in Fig. 4.2(b) with the standard preroughening case in which $u_R \equiv 0$. There, at $y_R = 0$ the corrugation potential is competely flat and the interface is free to wander.

Consider now the addition of the substrate potential, κ_R. Since κ_R will vary only slowly with film thickness, our control variable is h_0. Minimizing (4.19) yields the equation

$$\sin(4\pi h) + \frac{y_R}{2u_R}\sin(2\pi h) = -\frac{\kappa_R}{4\pi u_R}(h - h_0). \tag{4.20}$$

Suppose first that $y_R = 0$, in which case we require

$$\sin(4\pi h) = -\frac{\kappa_R}{4\pi u_R}(h - h_0). \tag{4.21}$$

By periodicity we may suppose that $n \leq h_0 \leq n + \frac{1}{2}$. The local minima closest to h_0 which solve this equation lie just above n and just below $n + \frac{1}{2}$. When $h_0 = n + \frac{1}{4}$ they are symmetrically located and degenerate. They exist for sufficiently small κ_R, namely

$$\kappa_R < (4\pi)^2 u_R. \tag{4.22}$$

Thus for sufficiently thick films we will have, with increasing h_0, a first order transition precisely at $h_0 = n + \frac{1}{4}$ from slightly more than n layers to slightly less than $n + \frac{1}{2}$ layers. As h_0 increases further, h will increase to slightly more than $n + \frac{1}{2}$ layers until, precisely at $h_0 = n + \frac{3}{4}$, there is transition to slightly less than $n + 1$ layers. If (4.22) is not satisfied the substrate wipes out the corrugation and the film will grow continuously until (4.22) is satisfied. The closer we are to the triple point, the larger

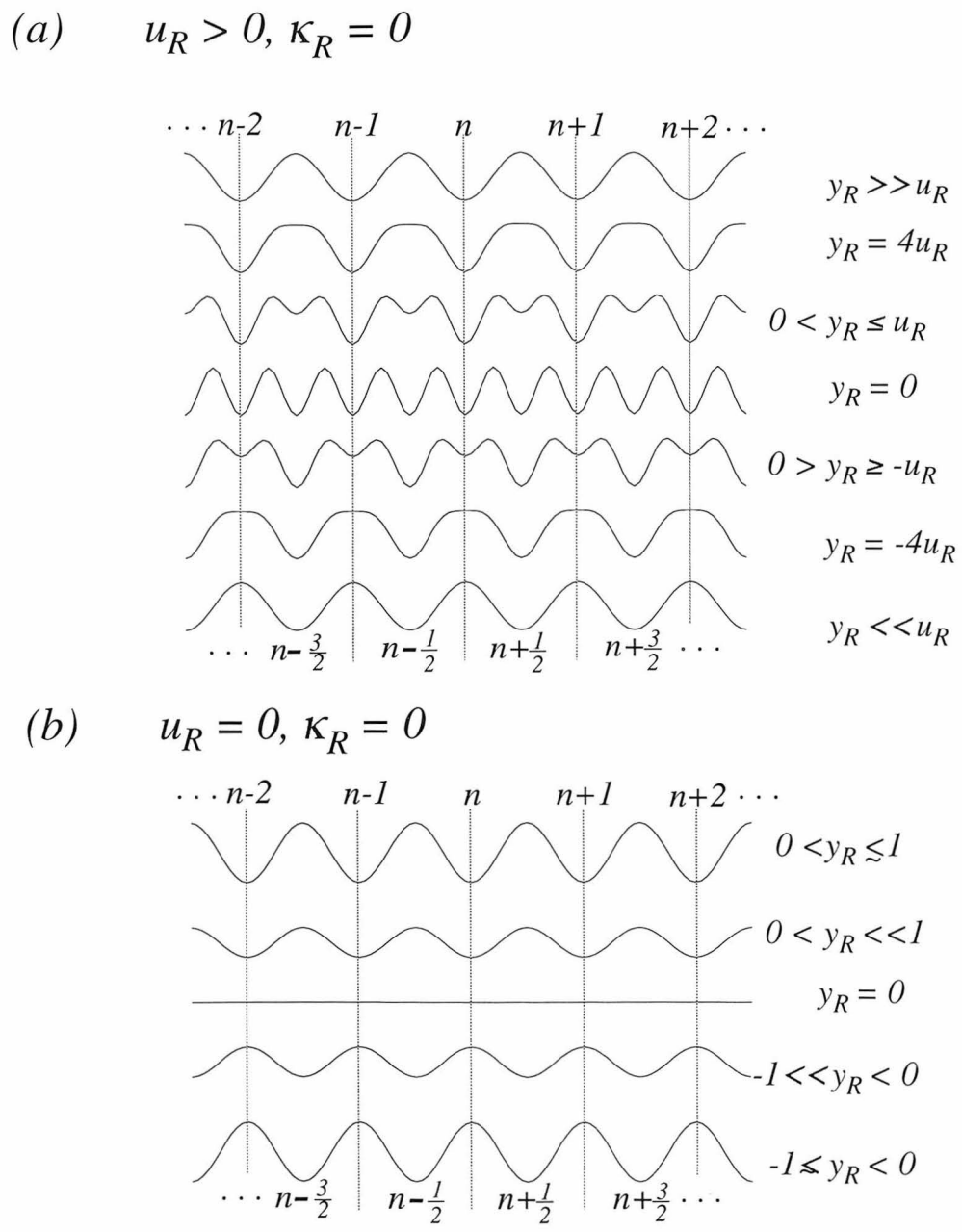

Figure 4.2: (a) Corrugation potential for the bulk interface ($\kappa_R = 0$) with $u_R > 0$ as a function of y_R. There is a first order preroughening transition at $y_R = 0$ when the integer minima exchange stability with the half-integer minima. (b) For comparison, the corrugation potential in the continuous preroughening case, $u_R = 0$.

will be κ_R and the thicker the film required to see layering.

In the opposite limit, where $|y_R| > 4u_R$, we may ignore u_R and obtain essentially the same picture as above, but with twice the period. Thus if $y_R > 0$ there are first order transitions between essentially integer interface heights precisely at $h_0 = n + \frac{1}{2}$, while if $y_R < 0$ the transitions are between essentially half-integer interface heights precisely at $h_0 = n$. Both sets of transitions are wiped out unless $\kappa_R < (2\pi)^2 y_R$.

The interesting question is what happens for $0 < |y_R| < 4u_R$. Clearly the local minima at half-integer h are most stable if $h_0 = n + \frac{1}{2}$. This minimum can be an absolute minimum only if κ_R is sufficiently large, namely

$$\begin{aligned} \kappa_R > \kappa_R^t \quad &\equiv \quad 16|y_R|\Big[1 + \frac{|y_R|}{\pi^2 u_R} - (\pi^2 - 4)\frac{y_R^2}{4\pi^4 u_R^2} \\ &+ \quad O\left(\frac{|y_R|^3}{u_R^3}\right)\Big] \end{aligned} \tag{4.23}$$

for small κ_R/u_R and y_R/u_R, which will be valid for thick films close to the bulk first order transition at $y_R = 0$. If this inequality is violated, which will always occur for sufficiently thick flims, only the transitions between integer surface heights (for $y_R > 0$) or half-integer surface heights (for $y_R < 0$) will be observed. If the inequality is satisfied, both sets of transitions will be seen. For κ_R larger than κ_R^t, we may compute the range, Δh_0, of h_0 around $n + \frac{1}{2}$ ($y_R > 0$) or n ($y_R < 0$) over which the new minimum is stable. Indeed one finds that

$$\Delta h_0 = \frac{1}{4}\left[1 - \frac{2y_R}{\pi^2 u_R} + O\left(\frac{y_R^2}{u_R^2}, \frac{\kappa_R - \kappa_R^t}{u_R}\right)\right]\frac{\kappa_R - \kappa_R^t}{\kappa_R^t}. \tag{4.24}$$

Thus $\kappa_R^t(y_R)$ is a triple point, with two new first order transitions extending out linearly from the horizontal layering lines at larger $|y_R|$. At $y_R = 0$ these new lines are precisely the transitions at $n \pm \frac{1}{4}$ found above. In the thick film limit, $\kappa_R \to 0$ one sees from (4.24) that these lines are essentially straight. We have therefore confirmed precisely the zippering picture shown in Fig. 2.1(d).

Finally, since $\kappa_R \sim 1/n^{2+\alpha}$ and, inverting (4.23), the triple point position, $y_R^t(\kappa_R) \approx \kappa_R/16u_R$, vanishes linearly with κ_R, the two sequences of triple points on either side

of $y_R = 0$ converge to the bulk interface first order preroughening temperature, T_0, also as $|T_n^{1,2} - T_{fo}| \sim 1/n^{2+\alpha}$ (with $\alpha = 2$ for a van der Waals substrate potential).

To complete the analysis, we discuss the question of how Fig. 2.1(d) converts to Fig. 2.1(c), either as κ_R increases or as K_0 decreases into the region where u is irrelevant. We shall see that if κ_R/u_R is sufficiently large, the triple points are wiped out and replaced by ordinary Ising critical points. We wish to understand how this happens in detail.

We have already seen that when $y_R = 0$ the first order transitions at $h_0 = n \pm \frac{1}{4}$ disappear if $\kappa_R/u_R > (4\pi)^2$. More generally, the critical point that signals the first appearance of the first order transition occurs when the line representing the right hand side of (4.20) precisely kisses an inflection point of the left hand side [see Fig. 4.3(a)]. For $y_R = 0$ this inflection point is at $h = n \pm \frac{1}{4}$, and the slope at this point gives the above critical value, $\kappa_R/4\pi u_R = k_c(y_R = 0) \equiv 4\pi$. For $y_R \neq 0$ but small one finds that the inflection points are at

$$\begin{aligned} \pm(h_{infl} - n) &= \frac{1}{4} + \frac{y_R}{32\pi u_R} \\ &+ \frac{2\pi^2}{3}\left(\frac{y_R}{32\pi u_R}\right)^3 + O\left(\frac{y_R^5}{u_R^5}\right), \end{aligned} \tag{4.25}$$

and the (negative of the) slope is

$$\begin{aligned} k_c(y_R) &= 4\pi\Bigg[1 + 8\pi^2\left(\frac{y_R}{32\pi u_R}\right)^2 \\ &+ 128\pi^4\left(\frac{y_R}{32\pi u_R}\right)^4 + O\left(\frac{y_R^6}{u_R^6}\right)\Bigg], \end{aligned} \tag{4.26}$$

with corresponding value of h_0,

$$\pm(h_0^c - n) = 4\frac{y_R}{32\pi u_R} - \frac{88\pi^2}{3}\left(\frac{y_R}{32\pi u_R}\right)^3 + O\left(\frac{y_R^5}{u_R^5}\right). \tag{4.27}$$

This is *larger* than $k_c(0)$, meaning that the first order transition is *more* stable for $y_R \neq 0$, existing for larger κ_R/u_R. Note that this computation assumes, effectively, $K_R \to \infty$ so that mean field theory is exact. This is fine for first order transitions,

but for second order transitions there will, in fact, be fluctuation corrections to this behavior so that both the exact position of the critical point and the critical behavior (which will be that of the two-dimensional Ising model) will be different.

We expect, then, that the stability of the first order transition will continue to increase as y_R increases. As further evidence for this we may examine the stability of the triple point, y_R^t. As shown in Fig. 4.4, the triple point becomes a tricritical point, and then a critical point when κ_R/u_R becomes so large that the pair of inflection points on either side of $h = n + \frac{1}{2}$ *merge* with the one at $h = n + \frac{1}{2}$, forming a single *fifth degree* inflection point (which, within Landau theory, defines a tricritical point). The vanishing of the third derivative at $h = n + \frac{1}{2}$ occurs when $y_R/u_R = 16$. The slope at this point is then $k_c^{tri} = 12\pi$. Thus only for $\kappa_R/u_R > 3(4\pi)^2$ is the triple point washed out. This is quite a bit larger than the value, $(4\pi)^2$, at which the first order transition disappears at $y_R = 0$.

We finally obtain, then, the following picture of the disappearance of the zipper with increasing κ_R and/or decreasing u_R. The zipper, for a given value of h_0, first breaks in the middle ($y_R = 0$), forming a pair of two-pronged forks. The prongs then become shorter, eventually retracting into the triple point. Precisely at the point where the prongs disappear, the triple point becomes a tricritical point. Beyond this the tricritical point becomes a simple Ising critical point, and locally the picture is now indistinguishable from Fig. 2.1(c). Now, κ_R decreases as h_0 increases. Hence as long as $u_R > 0$ remains fixed as the film thickens, this process occurs in *reverse* order, with the zipper reappearing for sufficiently thick films. In the higher, three dimensional space, $(h_0, y_R/u_R, \kappa_R/u_R)$, this process can be viewed as a sequence of plane sections of the usual tricritical surface [see Fig. 4.5]. Consequently, as K_0 decreases toward the point at which u become irrelevant, one has $u_R \to 0$, and ever thicker films will be required to see the zipper. This means that integer and half-integer layering transitions "unzip" from the bottom, becoming fully unzipped all the way to infinite layer thickness precisely when u becomes marginal. Note that the mapping of the original model onto this fully renormalized description may lead to some nonmonotonic dependence of the renormalized parameters on the original

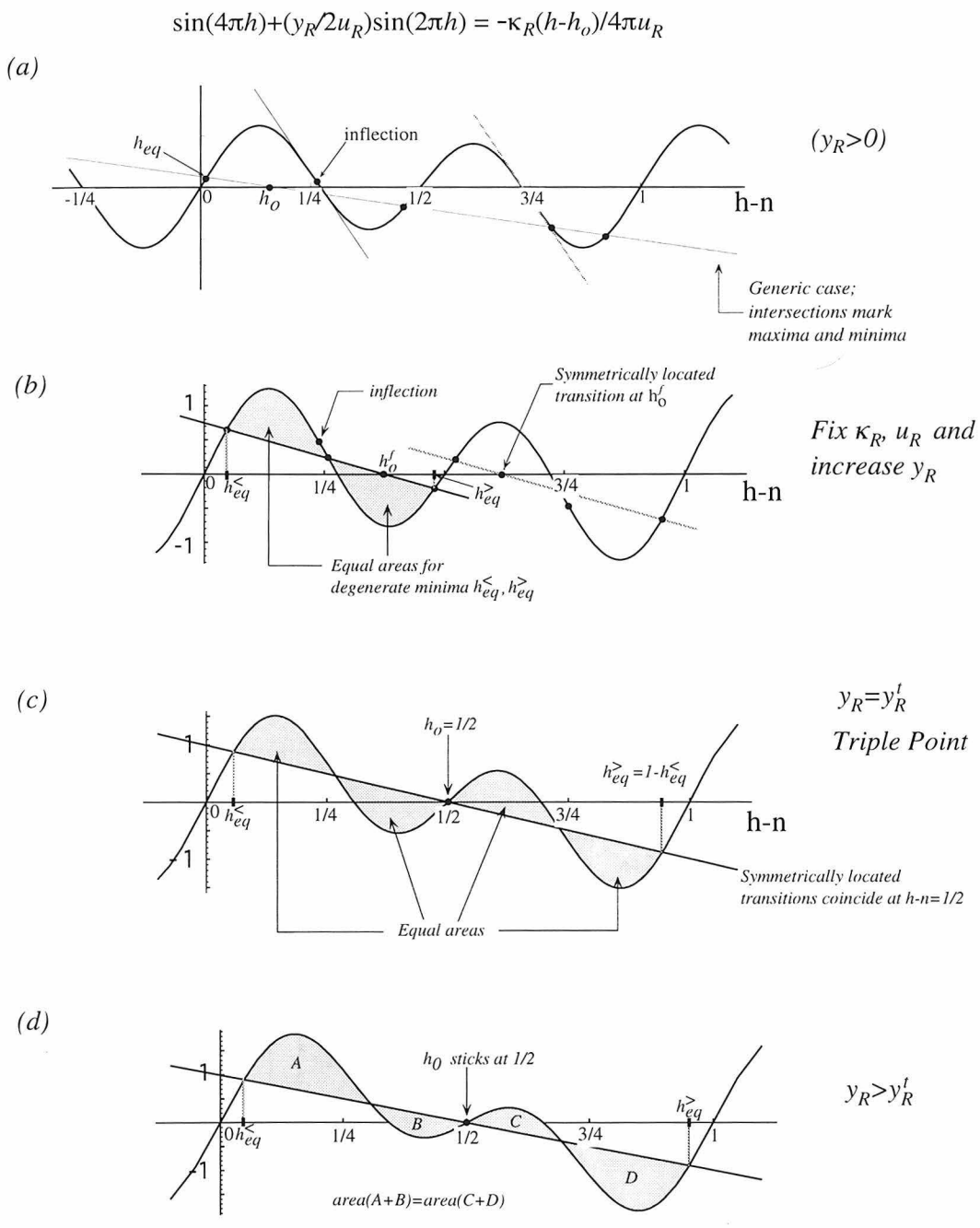

Figure 4.3: Graphical solutions of equation (4.20) for $u_R > 0$ which relates the layering phase diagram to the behavior of the bulk interface in the first order preroughening regime. (a) Inflection points and the first appearance of first order layering lines in the zipper regime. (b) Equal areas construction for the position of the first order zipper layering line. (c) The triple point. (d) Ordinary layering beyond the triple point.

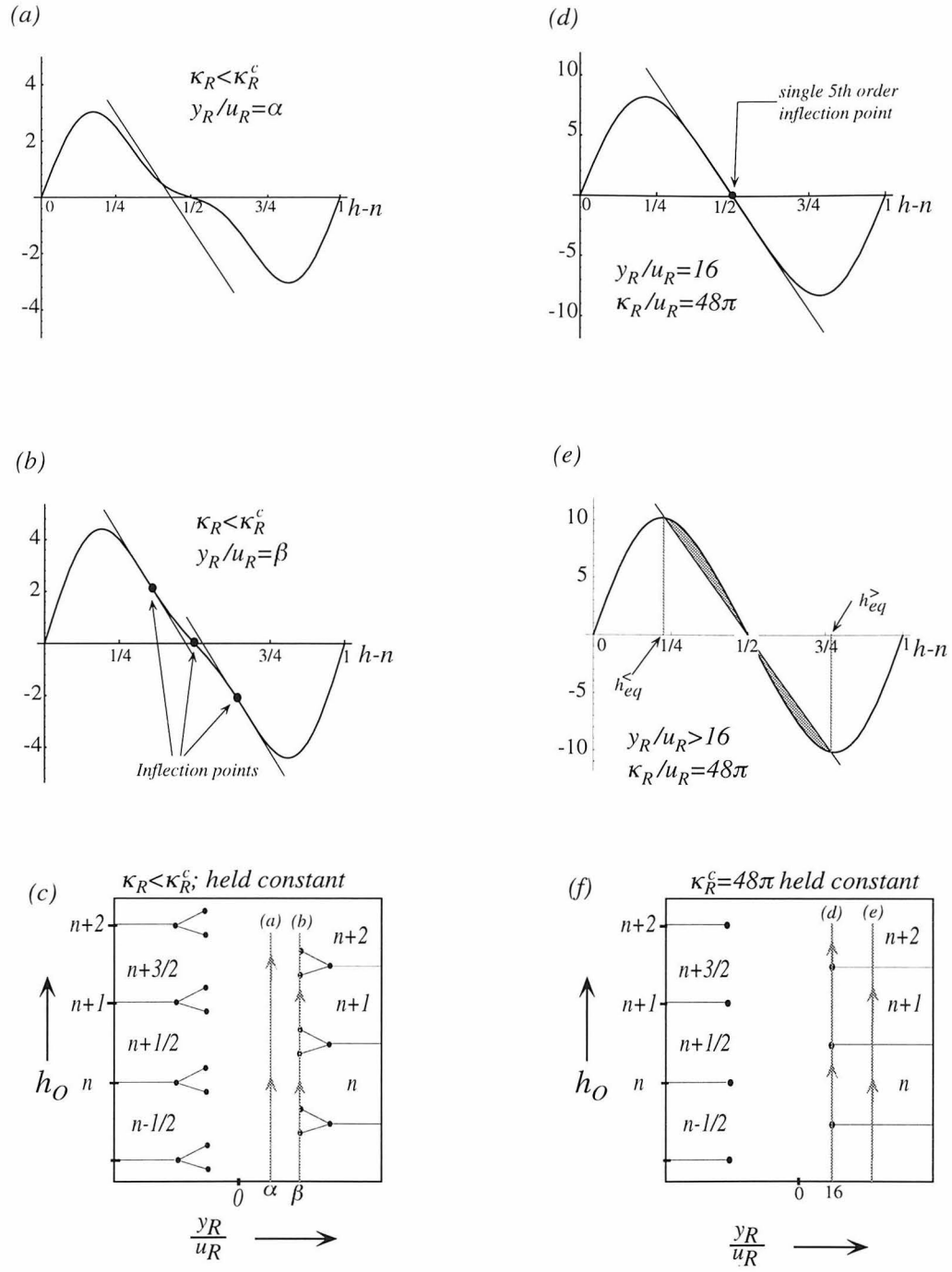

Figure 4.4: From triple point to tricriticality in the layering phase diagram for $u_R > 0$. (a) continuous increase in film thickness (shown as path a in part (c) of this figure). (b) corresponds to path b of part (c). (c) Schematic phase diagram, assuming for now that the substrate potential κ_R is constant , independent of film thickness, with $= \kappa_R < \kappa^c{}_R$. (d) When $\kappa_R = 48\pi$ and $y_R/u_R = 16$ the three inflection points merge into a single fifth order inflection point and triple point becomes a tricritical point; path d in part (f) of this figure. (e) Ordinary first order layering beyond the tricritical point (path (e) in part (f)).

ones (thus, for example, u_R, y_R and κ_R are all functions of J_1, J_2 and T). In thinner films one may therefore see behaviors different from the asymptotic behaviors we have found.

4.6.2 $u_R < 0$: Spontaneously broken particle-hole symmetry and interlacing

We next consider the case $u_R < 0$, which turns out to yield completely different behavior. The evolution of the substrate potential as y_R goes through zero is shown in Fig. 4.6. This figure is actually identical to Fig. 4.2(a) turned upside down. The major difference now is that the absolute minima at integer $h = n$ split *continuously in two* at $y_R = 4|u_R|$. The two new minima lie at $h = n \pm \theta(y_R)$ where $\theta(y_R)$ grows continuously from zero. Again, since this transition is continuous, fluctuation corrections will alter its nature and position. The transition, which appears as a classical Landau mean field critical point in our theory, must become a two-dimensional Ising critical point with $\theta(y_R) \sim |y_R - y_R^c|^{1/8}$ and $y_R^c \lesssim 4|u_R|$. At $y_R = 0$ one has, by symmetry, $\theta(0) = \frac{1}{4}$ so that the equilibrium mean surface heights are now $h = n \pm \frac{1}{4}$, rather than $h = n$ or $h = n + \frac{1}{2}$ as found when $u_R > 0$. For $y_R < 0$ the minima at $h = n + \theta(y_R)$ and $h = n + 1 - \theta(y_R)$ move together, eventually merging at $h = n + \frac{1}{2}$ when $y_R = -y_R^c \gtrsim 4u_R$. The merging also corresponds to a two-dimensional Ising critical point, with $\frac{1}{2} - \theta(y_R) \sim |y_R + y_R^c|^{1/8}$. For $y_R < -y_R^c$ only minima at $h = n + \frac{1}{2}$ remain, signifying the usual DOF phase.

Thus instead of the preroughening line simply becoming first order, it splits into two second order Ising lines, with a new intervening phase, which we call the θDOF phase [4], with *continuously varying mean surface height.* Den Nijs [4] first introduced this phase as a consequence of particle-hole symmetry violating terms in the Hamiltonian (which we neglect throughout this work), completely analogous to magnetic field terms in an Ising model. Here we find this phase as a result of *spontaneous* breaking of particle-hole symmetry driven by $u_R < 0$.

The layering phase diagram is now very simple to describe. In the presence of the

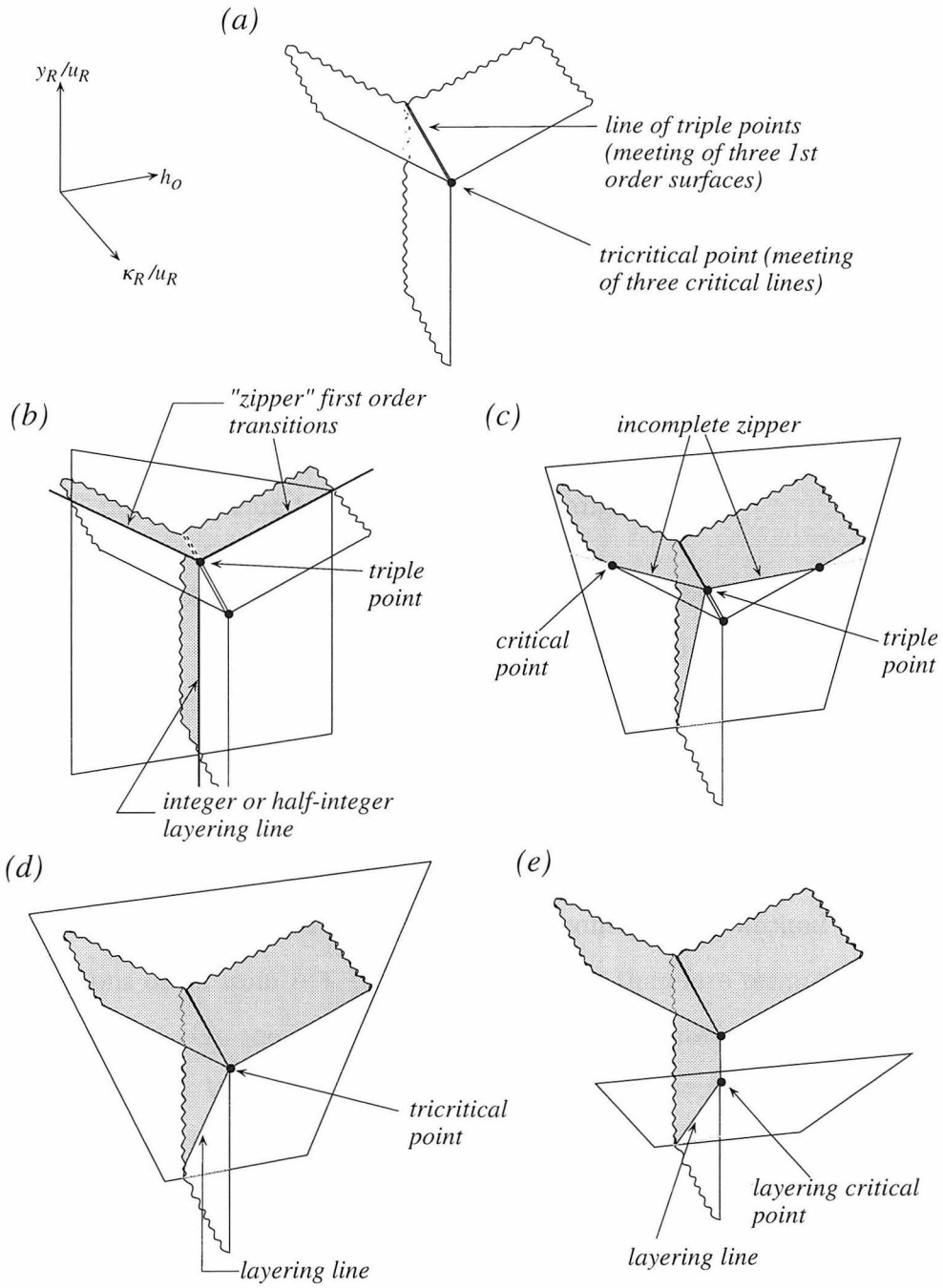

Figure 4.5: Zippered layering phase diagram as a sequence of plane sections of the ususal three dimensional tricritical region.

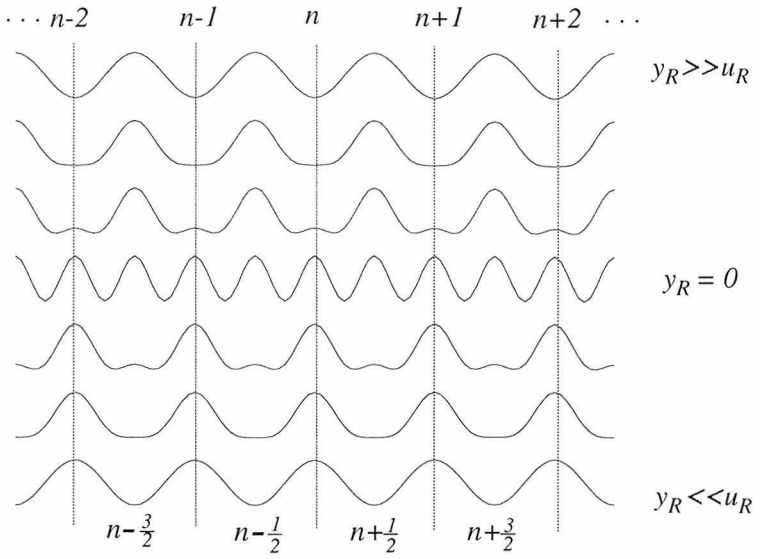

Figure 4.6: Evolution of the bulk interface corrugation potential for $u_R < 0$. The new θDOF phase appears for an intermediate range of y_R.

substrate potential it is clear by symmetry that neighboring minima can be degenerate only when $h_0 = n$ or $h_0 = n + \frac{1}{2}$. If $h_0 = n + \frac{1}{2}$ degenerate minima are, for large positive y_R, $h \simeq n$ and $h \simeq n + 1$, signifying the usual first order transitions between essentially integer film thicknesses. However, when $y_R \lesssim y_R^c$ the degeneracy is between $h \simeq n+\theta(y_R)$ and $h \simeq n+1-\theta(y_R)$ (approximate equality only due to the perturbative effect of κ_R on the positions of the minima). When $y_R \gtrsim -y_R^c$ these two minima merge, and the film thickness then varies continuously around $h = n + \frac{1}{2}$ for small deviations of h_0 from $n + \frac{1}{2}$. The layering line therefore terminates there in an Ising critical point. On the other hand, if $h_0 = n$ degenerate minima are, for large negative y_R, $h \simeq n \pm \frac{1}{4}$. When $y_R \gtrsim -y_R^c$ the degeneracy is between $h \simeq n \pm \theta(y_R)$, and when $y_R \lesssim y_R^c$ these two minima merge. The film thickness then varies continuously around $h = n$ for small deviations of h_0 from n. The layering line therefore again terminates in an Ising critical point, but this time as y_R increases rather than decreases. In the intermediate regime, $-y_R^c \lesssim y_R \lesssim y_R^c$, both sets of lines exist. Thus, unlike the case $u_R = 0$ where the two sets of lines are pushed apart so that there is a small region about $y_R = 0$ where the film can grow continuously, the two sets, though independent and nonintersecting, are interlaced so that at no time can one have

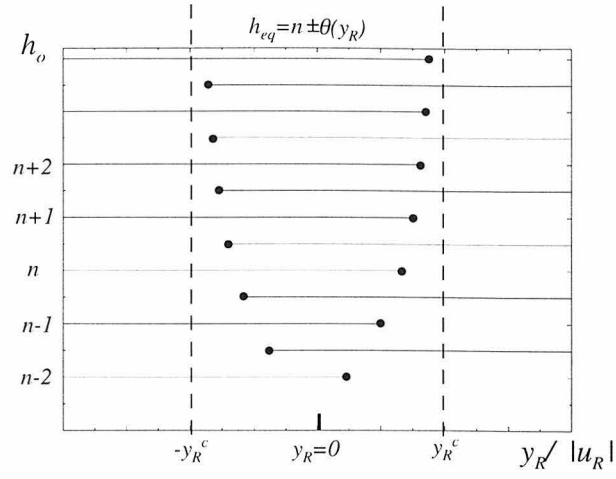

Figure 4.7: Intermeshing layering phase diagram for $u_R < 0$. The two sequences of layering critical points approach the boundaries of the θDOF phase as the film thickens.

unbounded continuous film growth (see Fig. 4.7). Note, however, that if one varies y_R in an oscillatory fashion as h_0 increases, one can in principle follow a snake-like path to grow an arbitrarily thick film without ever crossing a layering line. This is another signal that the bulk interface transition is second order rather than first order. As $n \to \infty$ the two sets of Ising critical points converge to the bulk interface Ising transitions at $y_R = \pm y_R^c$, with $T^1_{I,n} - T^1_I, T^2_I - T^2_{I,n} \sim n^{-(2+\alpha)}$, just as for first order preroughening.

4.7 Global phase diagram

The computations in this section are relevant both to roughening and preroughening phenomena on the bulk interface and to layering phenomena in film growth. The results for $u_R \neq 0$ are new and, as we have seen, have strong impact on the phase diagrams. In particular, some previous results in the literature [4] require some revision.

Thus, Fig. 2 in Ref. [4] shows the Ising transition between DOF and reconstructed phases joining the preroughening line precisely at the point labelled N where u becomes relevant. We believe this to be incorrect: the point N will generically lie to the

left (toward smaller $L = J_2/k_BT$) of the Ising line, which we expect, assuming that $u_R > 0$ for the $RSOS$ model, to join the *first order* preroughening line at a critical end point N' distinct from N [see Fig. 2.1(a)]. The point N is therefore tricritical, rather than bicritical as proposed by den Nijs [4]. The physics of the Ising line is separate from that of the preroughening line (in fact, for a triangular lattice substrate the reconstructed phase, and hence the Ising line, is completely absent), and we see no reason why they should be connected at N. Our plaquette mean field calculations will lend further credence to the distinction between N and N'. We shall find, however, that the first order transition remains extremely weak, which may explain why it was not seen in earlier numerical investigations of the $RSOS$ model.

Alternatively, if $u_R < 0$ the preroughening line splits into two Ising lines at the point N, with the new θDOF phase in between [see the inset to Fig. 2.1(a)]. This type of behavior is not seen in the $RSOS$ model, but has been seen in the two-dimensional Ashkin-Teller model [68], which may also be interpreted as a interface model but different from the $RSOS$ model that we have focussed on so far. The connection between the Ashkin-Teller model and a Solid-on-Solid model is explored further in the next section.

4.8 An explicit model with a θDOF phase

In our considerations of the sine-Gordon phenomenology above we found that if $u_R < 0$ when y_R changes sign, then the preroughening transition occurs with a *continuous* variation of surface height even in the absence of a substrate (in contrast to "conventional" preroughening where there there is an abrupt change from integer to half-integer average surface height). In this section we discuss the two component BCSOS model; this is a bona fide microscopic model which will have an intermeshed phase diagram. This model was first introduced in another context by [65] and certain aspects of its phase diagram were discussed recently in [66]

4.8.1 The two component BCSOS Model

The BCSOS model is a solid on solid model with a (100) body centered cubic structure. There is *always* a height difference between nearest neighbors. Moreover, since a *two component* model is being considered, there are two species of atoms, A and B and nearest neighbors are *required* to be of different species. (These restrictions are not necessarily unrealistic: NaCl has precisely this structure.) It is convenient to represent steps appearing between different heights by directed lines just as was done in the in the discussion of the ice type models. If there were only one species of atom, then there would be exactly six different types of vertex configurations that could occur. (As we have already discussed in the context of the 6 vertex model). The presence of two species gives rise to 12 different vertex configurations; these are shown in Fig. 4.8. We will sometimes be refer to this model as the staggered-6V model. We take the boltzmann weights to be $a = e^{-J_A}$, $b = e^{-J_B}$ and $c = 1$ where J_A and J_B are positive vertex energies. It is clear that if one atom, say of type A, occupies a

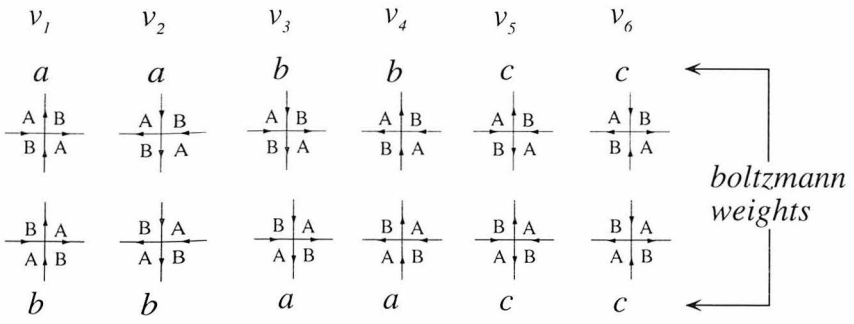

Figure 4.8: The 12 distinct vertices in the two component BCSOS model along with their boltzmann weights.

site whose height (relative to some reference zero height) is an even number then all atoms of species A will have even surface height regardless of the phase of the film. Henceforth we will assume that A atoms have even integer heights and B atoms have odd integer heights. One sample configuration of the system is shown in Fig. 4.9.

For the purposes of establishing the correspondence of this model to the Ashkin-Teller (AT) model (details can be found in App. C) it is convenient to treat it as a *staggered 8-vertex model* with boltzmann weights equal to zero for the vertices shown

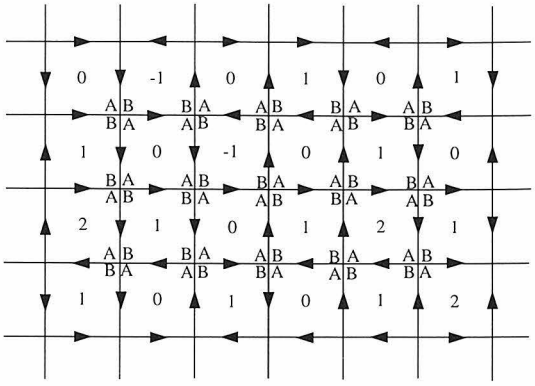

Figure 4.9: A sample configuration of the two component BCSOS model. Note that all A sites are at even integer heights and all B sites are odd.

in Fig. 4.10 and the weights of Fig. 4.8 for the other vertices. It should be emphasized that the additional vertices that are being introduced in Fig. 4.10 have no consistent interpretation in terms of surface heights and are only used to facilitate the mapping to the AT model. From equation (C.5) which relates the staggered BCSOS model

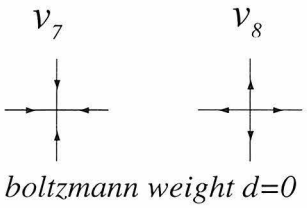

Figure 4.10: Vertices added on (with zero weight) to allow the staggered-6V model to be considered as a staggered-8V model.

to the AT model, the phase diagram of the staggered BCSOS model can be mapped out; it is shown in Fig. 4.11(a). There is a line of continuously varying exponents which splits into two Ising lines. In region I the average height of the surface is an even integer and the A sublattice is essentially completely ordered while the B lattice is disordered with about half the B-atoms at a height one layer above the A lattice height and half of the B-atoms one layer below. In region III the B lattice is ordered and the A lattice is disordered. In region II both sublattices are ordered. If, as the temperature is varied, the system follows the path PQ shown in the figure, then there will be two Ising transitions with continuous surface height growth between these transitions. When, in addition, a substrate potential is present and the full

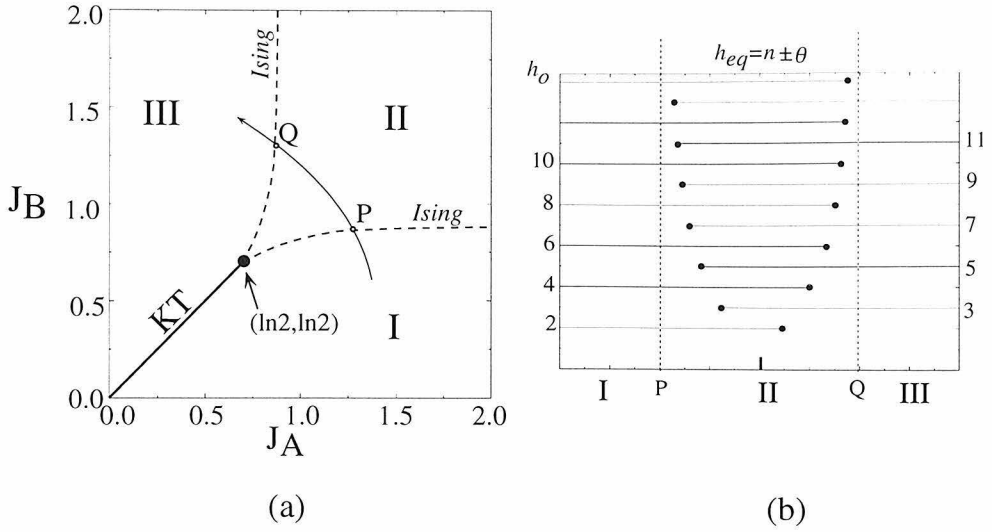

Figure 4.11: (a) Staggered BCSOS model phase diagram. The line labelled PQ is a path through phase space that would yield the layering diagram shown in (b).

chemical potential vs. temperature phase diagram is mapped out, it will be as shown in Fig. 4.11(b). It should be noted that the filling factor of the top layer, θ, ranges continuously from 0 to 1 (rather than from 0 to half as in previous sections) because we have chosen to define one unit of height as one layer of A atoms or one layer of B atoms instead of as being the sum of one layer of each.

Chapter 5 Calculational results

5.1 Single spin computations

Many of the phases we are interested in can be investigated, often analytically, within a simple single spin mean field formalism. In order to gain insight we begin with these computations. This allows one to discuss not only the usual layering phenomena, but also the interplay between the thin film analogues of reconstruction and roughening. In particular, we shall elucidate the nature of the reconstructed rough phase. Multi-spin plaquettes will be used later to improve the accuracy of the calculations as well as to describe phases that the single spin theory misses.

5.1.1 Spin-$\frac{1}{2}$ computations: tricriticality and tetracriticality in reconstructed layering

If in addition, one is interested only in phenomena involving at most two different layers, a spin-$\frac{1}{2}$ model suffices. The Hamiltonian is given by equation (3.8), and its basic phenomenology was outlined in Sec. 3.2.1. Here we fill in some of the details via explicit computations.

Applying the formalism of App. A, the single site mean field free energy functional is

$$\begin{aligned} \mathcal{F}\{H_i, \sigma_i; h_i\} &= -K \sum_{\langle ij \rangle} \sigma_i \sigma_j - L \sum_{(ik)} \sigma_i \sigma_k \\ &- \sum_i (H_i + h_i)\sigma_i - \sum_i \ln \cosh(H_i). \end{aligned} \tag{5.1}$$

We assume that $L > 0$, but that K can have either sign. The first of the saddle point equations, (A.9), yields $\sigma_i = -\tanh(H_i)$. Substituting this relation into (5.1)

we obtain the Bogoliubov mean field free energy

$$F\{h_i\} = \min_{\{\sigma_i\}}[A\{\sigma_i\} - \sum_i h_i\sigma_i] \tag{5.2}$$

where the mean field Helmholtz free energy is [see also equation (3.17) and the discussion preceeding it]

$$\begin{aligned} A\{\sigma_i\} &= -K\sum_{\langle ij\rangle}\sigma_i\sigma_j - L\sum_{(ik)}\sigma_i\sigma_k \\ &- \frac{1}{2}\sum_i[(1-\sigma_i)\ln(1-\sigma_i) \\ &+ (1+\sigma_i)\ln(1+\sigma_i)]. \end{aligned} \tag{5.3}$$

We restrict our attention to a bipartite lattice, with sublattices A and B. Let there be q_1 nearest neighbors and q_2 next nearest neighbors. We assume that the only relevant phases are those with uniform magnetization, $\sigma_i = m_A$ for $i \in A$ and $\sigma_i = m_B$ for $i \in B$, on each sublattice, with corresponding fields h_A and h_B. The ferromagnetic and antiferromagnetic order parameters are, respectively, $m \equiv \frac{1}{2}(m_A + m_B)$ and $m^\dagger \equiv \frac{1}{2}(m_A - m_B)$, with corresponding conjugate fields $h = h_A + h_B$ and $h^\dagger = h_A - h_B$. In terms of these (5.2) becomes

$$F\{h_i\}/N \equiv f(h, h^\dagger) = \min_{m,m^\dagger}[a(m, m^\dagger) - hm - h^\dagger m^\dagger], \tag{5.4}$$

where the Helmholtz free energy per site is

$$\begin{aligned} a(m, m^\dagger) &\equiv A\{\sigma_i\}/N = -\frac{1}{2}cm^2 - \frac{1}{2}c^\dagger m^{\dagger 2} \\ &+ \frac{1}{4}(1-m-m^\dagger)\ln(1-m-m^\dagger) \\ &+ \frac{1}{4}(1-m+m^\dagger)\ln(1-m+m^\dagger) \\ &+ \frac{1}{4}(1+m-m^\dagger)\ln(1+m-m^\dagger) \\ &+ \frac{1}{4}(1+m+m^\dagger)\ln(1+m+m^\dagger), \end{aligned} \tag{5.5}$$

and where $c = Kq_1 + Lq_2$ and $c^\dagger = -Kq_1 + Lq_2$. Notice that $c > c^\dagger$ whenever $K > 0$ and $c^\dagger > c$ whenever $K < 0$. When both K and L are positive we expect $m_A = m_B = m$ and $m^\dagger = 0$. In this case $a(m)$ is identical to the mean field free energy of a model with nearest neighbor interactions only, but effective coupling $K_{eff} = K + q_2 L/q_1$, and we learn nothing new. The second neighbor coupling gives rise to interesting new physics, then, only in the antiferromagnetic regime, $K < 0$.

Let us then use (5.4) to understand the onset of antiferromagnetism. The antiferromagnetic-paramagnetic phase boundary is located by considering the stability of the paramagnetic phase, where $m^\dagger = 0$, to nonzero $m^\dagger$. To this end, let $m_0(h)$ be the value of m that minimizes the right hand side of (5.4) with $m^\dagger \equiv 0$ and $h^\dagger \equiv 0$, i.e.,

$$m_0(h) = \tanh[cm_0(h) + h], \tag{5.6}$$

and let the corresponding free energy be $f_0(h)$. To see if this is the true minimum we Taylor expand the right hand side of (5.4) in the deviations $\delta m \equiv m - m_0(h)$ and $m^\dagger$ (maintaining $h^\dagger = 0$). Since we expect any phase transition to be driven by the onset of $m^\dagger$, we further minimize the resulting expression over δm for a given $m^\dagger$, yielding

$$\begin{aligned} \delta m &= -\frac{m_0}{(1-m_0^2)[1-c(1-m_0^2)]} m^{\dagger 2} \\ &+ \frac{m_0}{(1-m_0^2)^3[1-c(1-m_0^2)]} \left\{ \frac{m_0^2}{[1-c(1-m_0^2)]^2} \right. \\ &- \left. \frac{1+3m_0^2}{[1-c(1-m_0^2)]} + (1+m_0^2) \right\} m^{\dagger 4} + O(m^{\dagger 6}). \end{aligned} \tag{5.7}$$

We obtain then the result

$$\begin{aligned} a(m, m^\dagger) - hm &= f_0(m_0) + \frac{1}{2} r^\dagger m^{\dagger 2} + u^\dagger m^{\dagger 4} \\ &+ v^\dagger m^{\dagger 6} + w^\dagger m^{\dagger 8} + O(m^{\dagger 10}), \end{aligned} \tag{5.8}$$

where

$$\begin{aligned} r^\dagger &= \frac{1-c^\dagger(1-m_0^2)}{(1-m_0^2)} \\ u^\dagger &= \frac{(1-3m_0^2)-c(1+3m_0^2)(1-m_0^2)}{12(1-m_0^2)^3[1-c(1-m_0^2)]} \\ v^\dagger &= \frac{m_0^2}{6(1-m_0^2)^5[1-c(1-m_0^2)]^3}[(m_0^2-3) \\ &+ 3c(m_0^2+3)(1-m_0^2) \\ &- 6c^2(1+m_0^2)(1-m_0^2)^2]. \end{aligned} \tag{5.9}$$

We have therefore obtained a standard Landau free energy functional for $m^\dagger$. Thus, if $u^\dagger > 0$, there is an instability toward antiferromagnetism when $r^\dagger < 0$. The antiferromagnetic critical point therefore occurs when

$$c^\dagger \equiv T^\dagger(h)/T_0^\dagger = 1 - m_0(h)^2, \tag{5.10}$$

where $T_0^\dagger = (|J_1|q_1 + J_2q_2)/k_B \equiv J_0^\dagger/k_B$ is the transition temperature at $h = 0$. Note that $T/T_0^\dagger < 1$. For very large h, $m_0(h)$ will be very close to unity, and $r^\dagger > 0$. As h decreases, for a given fixed $T < T_0^\dagger$, $m_0(h)$ decreases and eventually the phase boundary will be reached for some critical $h = h^\dagger(T)$, which increases as T decreases. Below the transition $m^\dagger$ increases continuously from zero as $m^\dagger \sim (h^\dagger - h)^\beta$ with $\beta = \frac{1}{2}$ in this mean field approximation (an exact theory would yield the two-dimensional Ising result $\beta = \frac{1}{8}$).

Another possibility is that $u^\dagger < 0$ but $v^\dagger > 0$. In this case the transition will be first order, with the minimum at $m^\dagger = 0$ trading stability with two degenerate minima at nonzero $m^\dagger$. The point $u^\dagger = r^\dagger = 0$ where the transition converts from second to first order is then a tricritical point. From (5.9) we see that $u^\dagger$ is positive for

$$c \equiv T/T_0 > \frac{(1-m_0^2)(1+3m_0^2)}{1-3m_0^2} \tag{5.11}$$

where $T_0 = (q_2J_2 - q_1|J_1|)/k_B \equiv J_0/k_B$. This inequality will be valid for sufficiently small m_0. Therefore the antiferromagnetic transition line will be second order if $T/T_0^\dagger$

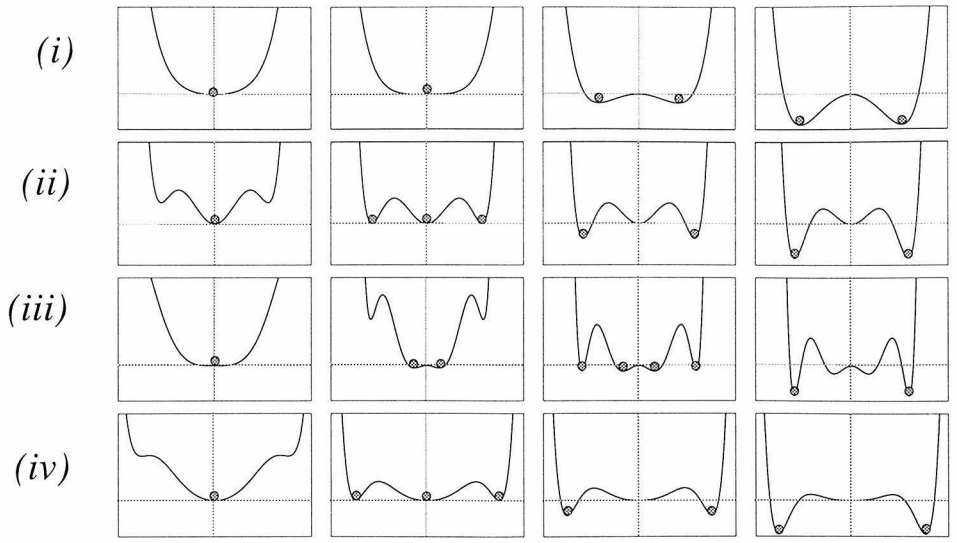

Figure 5.1: Behavior of the free energy in the vicinity of the tetracritical point. The sequences shown correspond to paths (i),(ii),(iii),(iv) in figure (3.3a)

is large enough. On the other hand, the simultaneous condition $r^\dagger = 0$ and $u^\dagger = 0$ then yields a tricritical point, T_{tri}, at

$$\frac{k_B T_{tri}}{J_0^\dagger} = \frac{2}{3}\frac{1 + 2J_0/J_0^\dagger}{1 + J_0/J_0^\dagger}. \tag{5.12}$$

This actually leads to *line* of tricritical points in the K-L plane. It is easy to check that $u^\dagger$ remains negative for all $T < T_{tri}$.

When $T < T_{tri}$ the transition line is no longer given by $r^\dagger = 0$. Rather, one must look to see when the minimum at $m^\dagger = 0$ is no longer the absolute minimum. For small negative $u^\dagger$ one then finds a first order transition at $r^\dagger = u^{\dagger 2}/2v^\dagger > 0$ at which $m^\dagger$ jumps from zero to $m^\dagger = \sqrt{-u^\dagger/2v^\dagger}$. The transition therefore takes place *before* the putative second order line at $r^\dagger = 0$.

The tricritical point exists so long as $v^\dagger > 0$. One may check the sign of $v^\dagger$ on the tricritical line and verify that it is positive for

$$\frac{k_B T}{J_0^\dagger} > \frac{11 - \sqrt{33}}{6} \simeq 0.8759. \tag{5.13}$$

The point $k_B T_{tet}/J_0^\dagger = (11 - \sqrt{33})/6$ is *tetracritical* since $r^\dagger$, $u^\dagger$, and $v^\dagger$ all vanish

simultaneously. For $k_BT/J_0^\dagger < (11-\sqrt{33})/6$ new behavior occurs. In Fig. 5.1 we show the structure of the minima in the free energy, (5.8). One finds that the tricritical point now becomes a critical end point which terminates the second order line *before* the first order line ends. The first order line now terminates in a critical point completely within the antiferromagnetic phase (see Fig. 3.3). Thus at temperatures below the critical end point, as a function of magnetic field, there is a first order transition to the antiferromagnetic phase, while above it the transition is second order. However, at temperatures above, but close to the critical end point, the second order transition is followed by a first order transition from one nonzero value of $m^\dagger$ to another. The projection of these lines into the K-L plane is shown at the bottom of Fig. 3.3(d). Note that the antiferromagnetic transition in the model with nearest neighbor interactions only ($J_2 = 0$) is always second order.

5.1.2 Spin-1 computations: the reconstructed rough phase

We consider next the spin-1 model (3.9). This will allow us to deal with phases and phase transitions involving three different layer thicknesses. It will turn out that this model contains essentially all the physics needed to explain all the phases in the exact Hamiltonian. The simplest application is to layering in the ferromagnetic regime where the spin-1 model exhibits two layering transitions at low temperatures: between the phase with $m \simeq -1$ and the phase with $m \simeq 0$ and between the phase with $m \simeq 0$ and the phase with $m \simeq 1$. However the results here do not contain any new physics, and the extension to the full layering phase diagram, Fig. 2.1(b), is clear. In this subsection, therefore, we focus instead on the film analogue of the reconstructed rough phase, and transitions from it to the reconstructed flat and disordered flat phases. All of these may be elucidated from the single site mean field theory. Only the preroughening transition between the flat and disordered flat phases requires the retention of a plaquette of spins, and this will be discussed in Sec. 5.2.

For the spin-$\frac{1}{2}$ model the $RSOS$ condition was redundant because the spins could take only two values. In the spin-1 case we must include it explicitly. Since we are

still dealing only with single site mean field theories the condition must be imposed on the mean field alone and the discussion in Sec. 3.3.2 is relevant. We choose to approximate the $RSOS$ condition by a nearest neighbor quartic interaction. Thus we consider the mean field theory of the Hamiltonian

$$\begin{aligned}\bar{\mathcal{H}}_1' &= \bar{\mathcal{H}}_1 + \frac{1}{4}K'\sum_{\langle ij\rangle}(s_i - s_j)^4 \\ &= -(K+2K')\sum_{\langle ij\rangle} s_i s_j + \frac{3}{2}\sum_{\langle ij\rangle} s_i^2 s_j^2 \\ &- L\sum_{(ik)} s_i s_k - h\sum_i s_i + \tilde{h}_2\sum_i s_i^2, \end{aligned} \tag{5.14}$$

with $K' \equiv J_1'/k_BT > 0$, $\tilde{h}_2 = h_2 + \frac{1}{2}Kq_1 + \frac{1}{4}K'q_1 + \frac{1}{2}Lq_2$ and we have used the fact that $s_i^3 = s_i$.

Since the interactions between spins now include quadratic terms the formalism in App. A tells us that the most general single site free energy functional we need to consider is

$$\begin{aligned}\Phi(H, H_2) &= -\ln\left(\frac{1}{3}\sum_{s=0,\pm1} e^{-Hs - H_2 s^2}\right) \\ &= -\ln\left\{\frac{1}{3}\left[1 + 2e^{-H_2}\cosh(H)\right]\right\}. \end{aligned} \tag{5.15}$$

The full mean field free energy functional is now obtained by associating independent saddle point theory variables σ_i with s_i and τ_i with s_i^2, yielding

$$\begin{aligned}\mathcal{F} &= -(K+2K')\sum_{\langle ij\rangle}\sigma_i\sigma_j + \frac{3}{2}K'\sum_{\langle ij\rangle}\tau_i\tau_j \\ &- L\sum_{(ik)}\sigma_i\sigma_k - \sum_i (H_i + h)\sigma_i \\ &- \sum_i (H_{2,i} - \tilde{h}_2)\tau_i + \sum_i \Phi(H_i, H_{2,i}). \end{aligned} \tag{5.16}$$

The only coupling between the σ's and the τ's is indirectly through the coupling of the H's and H_2's in Φ. Notice the *antiferromagnetic* coupling between the τ's.

To elucidate the nature of the reconstructed rough phase, specialize to $h = 0$.

What we will show is that when $J_1 < 0$ and J_2 is not too large there exists a phase in which $H_i, \sigma_i \equiv 0$, but τ_i has long range antiferromagnetic order. This means that the magnetization vanishes on all sites, but there is antiferromagnetic order in the magnitude of the *fluctuations* on each site. This is intuitively plausible because if we consider the special case $J_2 = 0$, the exact $T = 0$ *ground state* of $\mathcal{H}_1'$ has $s_i \equiv 0$ on one sublattice and $s_i = \pm 1$ randomly on the other sublattice. Thus even though $\langle s_i \rangle = 0$ everywhere, s_i^2 alternates between 0 and 1. Note that the $RSOS$ condition is required to stabilize this state: in its absence the ground state would have $s_i = 1$ on one sublattice and $s_i = -1$ on the other. Similarly, in our mean field treatment we expect such a state to exist only in a certain range of sufficiently large J_1'. At high enough temperature we expect this order to be destroyed, signaling the film analogue of the reconstructed rough to fully rough transition [The negative part of the K-axis in Fig. 2.1(A)]. We shall also see below that inclusion of $J_2 > 0$ allows for a transition to a phase with true antiferromagnetic order in the s_i. This corresponds to the film analogue of the reconstructed rough to reconstructed flat transition [path 5 in Fig. 2.1(C)]. This is again intuitively plausible because $J_2 > 0$ will force the ground state to break the symmetry of $s_i = \pm 1$ on the second sublattice, forcing all these s_i to take a common value. There will then be a first order layering-type transition as a function of field, h, between the state with alternating 0's and 1's and that with alternating 0's and -1's. When J_2 is large enough we shall find that the antiferromagnetic order can be lost with increasing temperature before the layering line terminates, corresponding to reconstructed flat to disordered flat transition [path 4 in Fig. 2.1(B)]. Thus long range positional order in the 0's and 1's (or 0's and -1's) can be lost while still maintaining a broken symmetry between 1's and -1's. This is the film analogue of the $K < 0$ region of the DOF phase. As mentioned earlier, to describe the film analogue of the preroughening transition in the $K > 0$ region of Fig. 2.1(A) will require a plaquette of more than one spin (see Sec. 5.2 below).

Specializing the free energy functional (5.16) to a two sublattice stucture for σ_i,

τ_i and $H_{2,i}$ we have

$$\begin{aligned} f \equiv \mathcal{F}/N &= -\frac{1}{2}(K+2K')q_1 m_A m_B - \frac{1}{4}Lq_2(m_A^2+m_B^2) \\ &- \frac{1}{2}(H_A+h)m_A - \frac{1}{2}(H_B+h)m_B \\ &+ \frac{3}{4}K'q_1\tau_A\tau_B - \frac{1}{2}(H_{2A}-\tilde{h}_2)\tau_A \\ &- \frac{1}{2}(H_{2B}-\tilde{h}_2)\tau_B \\ &- \frac{1}{2}\ln\left\{\frac{1}{3}\left[1+2e^{-H_{2A}}\cosh(H_A)\right]\right\} \\ &- \frac{1}{2}\ln\left\{\frac{1}{3}\left[1+2e^{-H_{2B}}\cosh(H_B)\right]\right\}. \end{aligned} \tag{5.17}$$

Variation with respect to H_{2A}, H_{2B} yields

$$\begin{aligned} \tau_A &= \frac{2e^{-H_{2A}}\cosh(H_A)}{1+2e^{-H_{2A}}\cosh(H_A)} \\ \tau_B &= \frac{2e^{-H_{2B}}\cosh(H_B)}{1+2e^{-H_{2B}}\cosh(H_B)}. \end{aligned} \tag{5.18}$$

Variation with respect to H_A and H_B yields

$$\begin{aligned} m_A &= -\frac{2e^{-H_{2A}}\sinh(H_A)}{1+2e^{-H_{2A}}\cosh(H_A)} \\ m_B &= -\frac{2e^{-H_{2B}}\sinh(H_B)}{1+2e^{-H_{2B}}\cosh(H_B)}. \end{aligned} \tag{5.19}$$

Inverting these and substituting them back into (5.17) we obtain the Bogoliubov free energy

$$\begin{aligned} f_{Bog} &= -\frac{1}{2}(K+2K')q_1 m_A m_B - \frac{1}{4}Lq_2(m_A^2+m_B^2) \\ &- \frac{1}{2}h(m_A+m_B) \\ &+ \frac{3}{4}K'q_1\tau_A\tau_B + \frac{1}{2}(\tau_A+\tau_B)[\tilde{h}_2-\ln(2)] + \ln(3) \\ &+ \frac{1}{2}(1-\tau_A)\ln(1-\tau_A) + \frac{1}{2}(1-\tau_B)\ln(1-\tau_B) \\ &+ \frac{1}{4}(\tau_A+m_A)\ln(\tau_A+m_A) \end{aligned}$$

$$
\begin{aligned}
&+ \quad \frac{1}{4}(\tau_A - m_A)\ln(\tau_A - m_A) \\
&+ \quad \frac{1}{4}(\tau_B + m_B)\ln(\tau_B + m_B) \\
&+ \quad \frac{1}{4}(\tau_B - m_B)\ln(\tau_B - m_B).
\end{aligned} \tag{5.20}
$$

Focusing first on the reconstructed rough phase, we set $h = 0$ and assume that $m_A = m_B = 0$. Minimizing f_{Bog} with respect to τ_A and τ_B then yields

$$
\begin{aligned}
\tau_A &= \frac{2e^{-\frac{3}{2}K'q_1(\tau_B - \tau_0)}}{1 + 2e^{-\frac{3}{2}K'q_1(\tau_B - \tau_0)}} \\
\tau_B &= \frac{2e^{-\frac{3}{2}K'q_1(\tau_A - \tau_0)}}{1 + 2e^{-\frac{3}{2}K'q_1(\tau_A - \tau_0)}},
\end{aligned} \tag{5.21}
$$

where $\tau_0 = -\frac{2}{3}\tilde{h}_2/K'q_1$ and $\tilde{h}_2$ was defined below (5.14). At high temperatures we expect $\tau_A = \tau_B \equiv \bar{\tau}$ with $0 \leq \bar{\tau} \leq 1$ satisfying

$$
\bar{\tau} = \frac{2e^{-\frac{3}{2}K'q_1(\bar{\tau} - \tau_0)}}{1 + 2e^{-\frac{3}{2}K'q_1(\bar{\tau} - \tau_0)}}. \tag{5.22}
$$

As T decreases we expect an instability either to a state with $\tau^\dagger \equiv \frac{1}{2}(\tau_A - \tau_B) \neq 0$, but $m_A = m_B = 0$ still, or to a state with $m_A = m_B \equiv m \neq 0$, but $\tau^\dagger = 0$. Treating the first case first, let $\tau = \frac{1}{2}(\tau_A + \tau_B)$ and $\delta\tau = \tau - \bar{\tau}$. Completely analogous to the computation leading to (5.8), we expand the free energy in a double Taylor series in $\tau^\dagger$ and $\delta\tau$. Mininimizing the result over $\delta\tau$ we find

$$
\delta\tau = -\frac{1}{2}\frac{(1-\bar{\tau})^{-2} - \bar{\tau}^{-2}}{3K'q_1/2 + \bar{\tau}^{-1}(1-\bar{\tau})^{-1}}\tau^{\dagger 2} + O(\tau^{\dagger 4}). \tag{5.23}
$$

Substituting this into the free energy we obtain the Landau expansion in $\tau^\dagger$ alone:

$$
f_{Bog} = f_0 + \frac{1}{2}r^\dagger\tau^{\dagger 2} + u^\dagger\tau^{\dagger 4} + O(\tau^{\dagger 6}) \tag{5.24}
$$

with

$$
f_0 = \frac{3}{4}K'q_1\bar{\tau}^2 = \ln(3) + [\tilde{h}_2 - \ln(2)]\bar{\tau}
$$

$$
\begin{aligned}
&+ \quad \bar{\tau}\ln(\bar{\tau}) + (1-\bar{\tau})\ln(1-\bar{\tau}) \\
r^{\dagger} &= \bar{\tau}^{-1}(1-\bar{\tau})^{-1} - \frac{3}{2}K'q_1 \\
u^{\dagger} &= \frac{1}{12}[(1-\bar{\tau})^{-3} + \bar{\tau}^{-3}] \\
&- \quad \frac{1}{8}\frac{[(1-\bar{\tau})^{-2} - \bar{\tau}^{-2}]^2}{3K'q_1/2 + \bar{\tau}^{-1}(1-\bar{\tau})^{-1}}.
\end{aligned} \tag{5.25}
$$

There is a unique minimum at $\tau^{\dagger} = 0$ for $\bar{\tau}^{-1}(1-\bar{\tau})^{-1} = 3K'q_1/2$. Therefore the critical point occurs at a temperature T_c determined by

$$
\bar{\tau}_c(1-\bar{\tau}_c) = \bar{T}_c. \tag{5.26}
$$

where $\bar{T} \equiv 2k_BT/3J_1'q_1$ and

$$
\bar{\tau}_c = \frac{2e^{-(\bar{\tau}_c - \tau_0)/\bar{T}_c}}{1 + 2e^{-(\bar{\tau}_c - \tau_0)/\bar{T}_c}}. \tag{5.27}
$$

It is easy to check that $u^{\dagger} > 0$ at this point. Since $\bar{\tau}(1-\bar{\tau}) \leq \frac{1}{4}$ it is clear that $\tau^{\dagger} = 0$ for $\bar{T} > \frac{1}{4}$. Whether or not solutions to (5.25), (5.26) exist depends on the temperature independent parameter $\tau_0 = -(2H_2 + J_1q_1 + J_2q_2 + J_1'q_1/2)/3J_1'q_1$ (recall that $H_2 = k_BTh_2$ is the curvature of the substrate potential). For example, if $\tau_0 = \frac{2}{3}$ then $\bar{\tau} = \frac{2}{3}$ for all $\bar{T}$, and we have $\bar{T}_c = \frac{2}{9}$. If $H_2 = 0$ on a square lattice ($q_1 = 4$) then this situation corresponds to $|J_1|/J_1' = \frac{3}{2}$. The maximal $\bar{T}_c$ is $\frac{1}{4}$ and corresponds to $\bar{\tau}_c = \frac{1}{2}$. This occurs for $\tau_0 = (2 - \ln(2))/4 \simeq 0.3267$. The general solution for τ_0 given any $0 < \bar{\tau}_c < 1$ is

$$
\begin{aligned}
\tau_0 &= \bar{\tau}_c(1-\bar{\tau}_c)\{(1-\bar{\tau}_c)^{-1} + \ln[\bar{\tau}_c/2(1-\bar{\tau}_c)]\} \\
&\approx \begin{cases} \bar{\tau}_c\ln(\bar{\tau}_c/2) \to 0, & \bar{\tau}_c \to 0 \\ 1 - (1-\bar{\tau}_c)\ln[2(1-\bar{\tau}_c)] \to 1, & \bar{\tau}_c \to 1. \end{cases}
\end{aligned} \tag{5.28}
$$

Treating now the second case, we take $\tau^{\dagger} = 0$ and expand the free energy in $\delta\tau$ and m. Again, minimizing the result with respect to $\delta\tau$ for given m we obtain

$$
\delta\tau = \frac{1-\bar{\tau}}{3\bar{\tau}}m^2 + O(m^4). \tag{5.29}
$$

Substituting this back into the free energy we obtain a Landau expansion in m alone:

$$f_{Bog} = f_0 + \frac{1}{2} r m^2 + u m^4 + O(m^6), \tag{5.30}$$

with

$$\begin{aligned} r &= \bar{\tau}^{-1} - (K + 2K')q_1 - L q_2 \\ u &= (2\bar{\tau}^{-2} + \bar{\tau}^{-3})/36 > 0. \end{aligned} \tag{5.31}$$

There is a phase transition to a ferromagnetic phase at $r = 0$. This yields implies a critical temperature T_0 determined by

$$\bar{\tau}_0 \equiv \bar{\tau}(T_0) = \tilde{T}_0, \quad \tilde{T} \equiv k_B T/(J_1 q_1 + 2J_1' q_1 + J_2 q_2). \tag{5.32}$$

The temperatures T_c and T_0 *coincide* when J_1, J_1', J_2 and h_2 satisfy the constraint

$$\begin{aligned} \tau_0 &= \rho(1-\rho)\{\rho^{-1} + \ln[(1-\rho)/2\rho]\} \\ \rho &\equiv (J_1 q_1 + 2J_1' q_1 + J_2 q_2)/(3J_1' q_1/2). \end{aligned} \tag{5.33}$$

where τ_0 was defined below (5.27). For given J_1, J_1' and h_2 it is easy to check that for J_2 larger than that satsfying (5.33) one has $T_0 > T_c$: the instability to the thin film analogue of the DOF phase occurs first, with a transition to a reconstructed checkerboard state occuring only at lower temperature. Conversely, for smaller J_2 one has $T_c > T_0$: the transition to the film analogue of the reconstructed rough phase occurs first, with the transition to the true antiferromagnetic state occuring only at lower temperature. The special value of J_2 at which $T_0 = T_c$ is bicritical with a direct transition from the paramagnetic to antiferromagnetic state. In Fig. 5.2 we show a numerical computation of the full phase diagram in the H-T plane for various values of J_2.

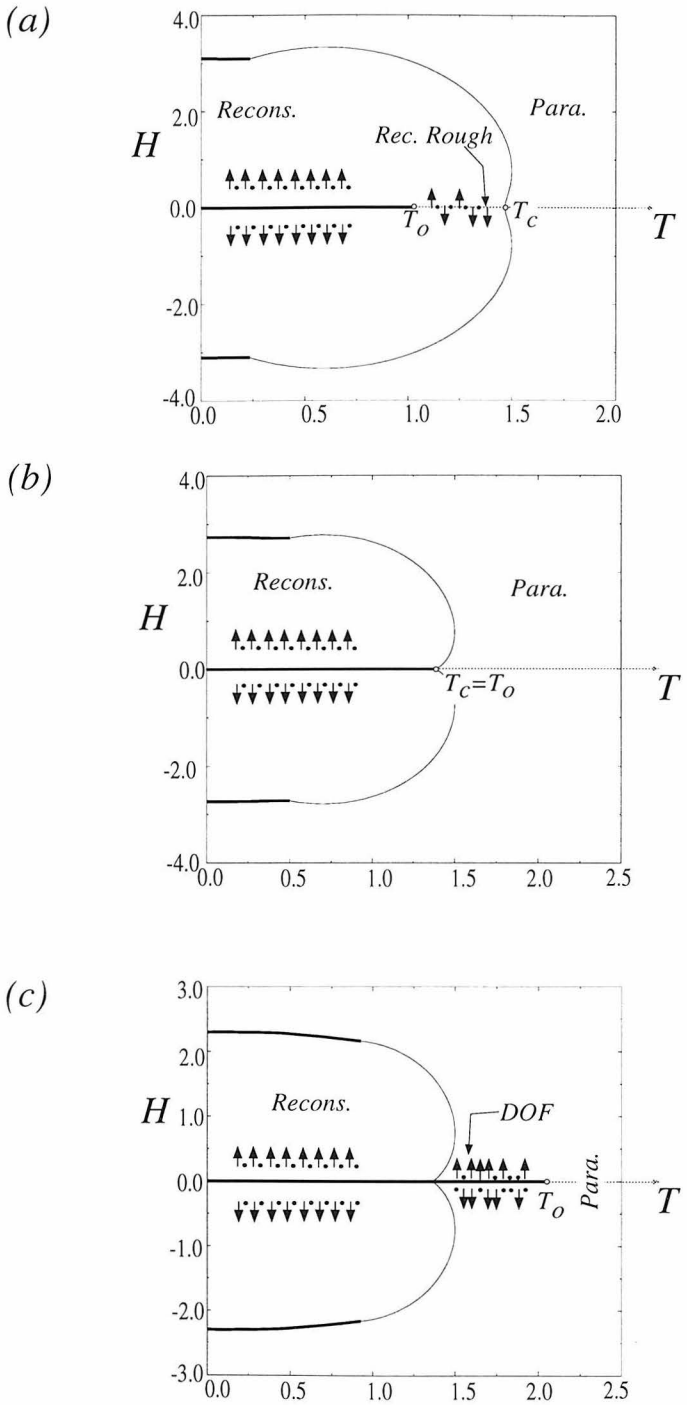

Figure 5.2: Spin-1 phase diagrams showing the thin film analogues of the reconstructed flat, reconstructed rough and disordered flat phases as the second neighbor coupling, J_2, varies: (a) small J_2, showing the termination of the antiferromagnetic layering line inside the reconstructed rough phase; (b) bicritical value of J_2, showing a direct transition from the rough to antiferromagnetic phase; (c) large J_2, showing first the appearance of the DOF phase, followed by the antiferromagnetic phase.

5.2 Correspondence between microscopic and sine-Gordon theory

So far we have discussed two rather different approaches in our study of surface phase transitions.

We began our study by looking at solid-on-solid models. These are microscopic system dependent models (with parameters like the nearest and next nearest neighbour interaction strengths, lattice structure, chemical potential, substrate strength etc.). Such an approach is useful when detailed comparisons with experiment or first principles simulations are to be made.

In Chapter 4 we adopted a different point of view: Since much of the interesting physics should be amenable to a long wavelength coarse grained description, we examined a sine-Gordon (SG) Hamiltonian (4.1) with partially renormalized parameters y_0, u_0, K_0 and an effective substrate potential $V_0[h]$. It is easy to find the flow equations of this model under renormalization and one can get detailed information about the manner in which the roughening and preroughening critical points of a film approach bulk behavior as the film thickens. Moreover, simple assumptions about the behavior of $y_0(T)$ (namely that it changes sign at some temperature T_c) and about u_0 lead to phase diagrams which are qualitatively identical to the experimental data.

We have not yet made precise the connection between these two approaches. In order to use the sine-Gordon type Hamiltonian for specific microscopic systems, a method of mapping the discrete lattice based parameters of the RSOS model into the partially renormalized parameters of the SG Hamiltonian is needed. The renormalization connection between the 8-vertex model (which includes a special type of roughening model, the BCSOS model) and the Gaussian model has been studied in [64, 67]. The main goal of these studies was to find which Gausssian operators are generated by specific 8-vertex operators. While this approach yields much useful information about the relevance of specific operators and about the universality class of the Hamiltonians, it does not provide an explicit mapping between the RSOS Hamiltonian and the corresponding Gaussian Hamiltonian. The *restricted* SOS condition

further complicates attempts to find the precise correspondence between the microscopic and coarse grained models. In the mean field approximation, however, it *is* possible to find the approximate mapping between the RSOS and the SG model; we do this below.

5.2.1 Single Site Theory

We first consider the single site MFT for the bulk crystal-vapor interface (no substrate). The Hamiltonian is

$$\begin{aligned} \overline{\mathcal{H}} &= \frac{K}{2}\sum_{\langle ij\rangle}[s_i - s_j]^2 + \frac{L}{2}\sum_{(ik)}[s_i - s_k]^2 \\ &= \alpha\sum_i s_i^2 - K\sum_{\langle ij\rangle} s_i s_j - L\sum_{(ik)} s_i s_k \end{aligned} \tag{5.34}$$

where $\alpha = (q_1 K + q_2 L)/2$. The formalism of App. A leads to the single site free energy

$$f_{MF}\{g\} = -\alpha(\sigma(g) - g)^2 - \log\left[\sum_{s=-\infty}^{\infty} e^{-\alpha(s-g)^2}\right] \tag{5.35}$$

where $g = \frac{H_i}{2\alpha}$ is a more convenient variable than the H_i used in the appendix and

$$\sigma(g) = \frac{\sum_{s=-\infty}^{\infty} s e^{-\alpha(s-g)^2}}{\sum_{s=-\infty}^{\infty} e^{-\alpha(s-g)^2}} \tag{5.36}$$

results from the second saddle point equation (equation A.9). Physically $\sigma(g)$ corresponds to the equilibrium film thickness. Since the system is periodic (with period equal to the layer thickness) in the absence of a substrate, we expect that there will be an infinite number of minima in the free energy, each corresponding to a thermodynamically stable configuration of the film. The equilibrium values $\{g_0\}$ are found by finding saddle points of f_{MF} with respect to g and the equilibrium film thickness is then given by $\sigma(g_0)$. It is easy to show from equation (5.35) that $f_{MF}(g+n) = f_{MF}(g)$ for any integer n. In order to get an approximate expression for f_{MF} which retains this periodicity one must find an approximation which does not truncate the sum in equation (5.35) .

A good way to do this is to use the Poisson summation formula

$$\sum_{k=-\infty}^{\infty} f(k) = \sum_{m=-\infty}^{\infty} \int_{-\infty}^{\infty} f(x) e^{-i2\pi m x}\, dx. \tag{5.37}$$

Using this we find

$$\sum_{s=-\infty}^{\infty} e^{-\alpha(s-g)^2} = \sqrt{\pi/\alpha}\left[1 + \sum_{n=1}^{\infty} 2e^{-n^2\pi^2/\alpha}\cos(2\pi n g)\right]. \tag{5.38}$$

Because of the factor $e^{-n^2\pi^2/\alpha}$ in sum, this new series is very rapidly convergent and for most purposes it is adequate to keep the first few terms. Moreover each term in this series is manifestly periodic in g. Thus we have

$$\begin{aligned} f_{MF}(g) = -\frac{1}{2}\log(\pi/\alpha) \;&-\; y_R\cos(2\pi g) \\ &-\; u_R\cos(4\pi g) + \mathcal{O}(y_R^9) \end{aligned} \tag{5.39}$$

where $y_R = 2e^{-\pi^2/\alpha}$ and $u_R \sim \mathcal{O}(y_R^4) \ll y_R$. It is clear that in the single site mean field theory y_R is always positive so that f_{MF} is minimized for integer valued g. Neglecting higher order terms, $\sigma(g) = g - (\pi y_R/\alpha)\sin(2\pi g)$, so that the film height is always integer valued in the single site mean field approximation in the absence of a substrate and there is no possibility of a disordered flat phase. We shall see below that the plaquette MFT *does* give a DOF phase. Another thing that becomes clear is that in MFT the true rough phase is absent because the free energy remains corrugated even at high temperatures (the coefficient $y_R \sim e^{-T}$ here). One can however take care of this problem by arguing that the surface will be rough once the amplitude of the corrugation falls below some value.

5.2.2 Plaquette Theory

We have claimed earlier that the plaquette MFT is expected to be more accurate than the single site theory because additional degrees of freedom are taken into account. We shall show that for a square lattice a 2×2 plaquette is enough to ensure the presence

of a DOF phase. In our treatment of the plaquette theory we shall also include the effect of a substrate potential. This discussion will be confined to attractive coupling between nearest neighbors. Similar (but more involved) calculations can be carried out for repulsive nearest neighbor interactions and these would yield reconstructed phases.

The Hamiltonian we work with is the same as the one in equation (5.34) except that we now add a term $\frac{1}{2}\kappa\sum_i[s_i - h_o]^2$ which models the presence of a substrate. κ depends on the strength of the effective substrate potential and h_o indicates the film the height at which the potential is a minimum. 2x2 plaquettes are then laid down on the square lattice and the Hamiltonian is rewritten as $\overline{\mathcal{H}} = \sum_P[h_P + h_{\rm interplaq}]$ where P denotes a sum over plaquettes and (in the notation of Fig. 3.5),

$$\begin{aligned} h_P &= \frac{1}{2}K[(s_{P1}-s_{P2})^2 + (s_{P2}-s_{sP3})^2 \\ &\quad +(s_{P3}-s_{P4})^2 + (s_{P4}-s_{P1})^2] \\ &+\frac{1}{2}L[(s_{P1}-s_{P3})^2 + (s_{P2}-s_{P4})^2] \\ &+(K+\frac{3}{2}L)(s_{P1}^2+s_{P2}^2+s_{P3}^2+s_{P4}^2) \\ &+\frac{1}{2}\kappa[(s_{P1}-h_o)^2 + (s_{P2}-h_o)^2 \\ &\quad +(s_{P3}-h_o)^2 + (s_{P4}-h_o)^2], \end{aligned} \tag{5.40}$$

and $h_{\rm interplaq}$ contains terms which couple neighboring plaquettes such as $-(K/2)s_{P1}s_{P32}$, $-(L/2)s_{P2}s_{P24}$ etc. From App. A, the mean field free energy per site is found to be

$$\begin{aligned} f_{MF} &= \frac{1}{4N}[\langle\overline{\mathcal{H}} - \overline{\mathcal{H}}_{\rm Bog}\rangle_{\overline{\mathcal{H}}_{\rm Bog}} + F_{\rm Bog}] \\ &= -(K+(3/2)L)\sigma^2 + g\sigma - (1/4)\log Z_{\rm Bog}. \end{aligned} \tag{5.41}$$

Here N is the number of plaquettes in the system, while $Z_{\rm Bog} = \sum'_{s_1,s_2,s_3,s_4} exp[-h_P + g(s_1+s_2+s_3+s_4)]$ is an effective "partition function" and $\sigma(g) = \frac{1}{4}\frac{\partial \ln Z_{\rm Bog}}{\partial g}$ is the average film thickness. The prime on the summation in $Z_{\rm Bog}$ is a reminder that the RSOS condition must be obeyed, i.e. for all s_1, one must have $|s_1 - s_2| \leq 1$,

$|s_2 - s_3| \leq 1$, $|s_1 - s_4| \leq 1$. If s_1 is considered as an unconstrained variable, then for $s_1 = n$, the RSOS condition allows only 19 different configurations for the other variables. The energy ϵ_i of the i^{th} configuration (the labelling is arbitrary) can be written as $\epsilon_i = a_i n^2 + b_i n + c_i$ where a_i, b_i and c_i are configuration dependent constants. (For instance, for the configuration $\begin{bmatrix} n & n \\ n & n \end{bmatrix}$, $a_1 = 4K + 6L + 2\kappa$, $b_1 = -4g - 4h_o\kappa$, $c_1 = 2\kappa h_o^2$.) Hence the partition function is

$$Z_{\text{Bog}} = \sum_{i=1}^{19} \sum_{n=-\infty}^{\infty} \exp(-a_i n^2 - b_i n - c_i). \tag{5.42}$$

Each sum over n can be reexpressed in terms of periodic functions using equation (5.38) with the result

$$\begin{aligned} Z_{\text{Bog}} = \sqrt{\frac{2\pi}{\Lambda}} \exp(-2\kappa h_o^2 \;&+\; \frac{\mu^2}{2\Lambda})[A + B\cos(2\pi\mu/\Lambda) \\ &+\; C\cos(4\pi\mu/\Lambda) + \ldots] \end{aligned} \tag{5.43}$$

where

$$\begin{aligned} \Lambda &= 8K + 12L + 4\kappa \\ \mu &= 4g + 4h_o\kappa \\ A &= 1 + 4\exp\left[-(\kappa + 4K + 5L)\right] \\ &\quad +4\exp\left[-(\kappa + 4K + 5L)/2\right] \\ &\quad +2\exp\left[-(\kappa + 6K + 3L)/2\right] \\ &\quad +8\exp\left[-(3\kappa + 14K + 13L)/8\right] \\ B &= 2\exp(-2\pi^2/\Lambda)(1 + 4\exp[-(\kappa + 4K + 5L)] \\ &\quad -4\exp\left[-(\kappa + 4K + 5L)/2\right] \\ &\quad -2\exp\left[-(\kappa + 6K + 3L)/2\right]) \\ C &= 2\exp(-8\pi^2/\Lambda)(1 + 4\exp[-(\kappa + 4K + 5L)] \\ &\quad +4\exp[-(\kappa + 4K + 5L)/2] \\ &\quad +\exp[-(\kappa + 6K + 3L)/2] \end{aligned}$$

$$-8\exp[-(3\kappa+14K+13L)/8]) \tag{5.44}$$

From equation (5.41) and equation (5.42) we find

$$\begin{aligned} f_{MF}(\theta) = & - y_R\cos(2\pi\theta) - u_R\cos(4\pi\theta) \\ & + \frac{\kappa}{2}[(\theta-h_o)-d(\theta)]^2 + \text{const.} \end{aligned} \tag{5.45}$$

This free energy is now in the SG form. Here a new variational parameter $\theta = \mu/\Lambda = 4(g+h_o\kappa)/\Lambda$ has been introduced, and $d(\theta) = (2\pi y_R/\Lambda)\sin(2\pi\theta)+(4\pi u_R/\Lambda)\sin(4\pi\theta)$. The sine-Gordon parameters can be expressed in terms of K, L and κ as

$$\begin{aligned} y_R &= \frac{B}{4A} + \mathcal{O}\left(\left(\frac{B}{A}\right)^3\right) \\ u_R &= \frac{C}{4A} - \left(\frac{1}{16}+\frac{\pi^2}{8\Lambda}\right)\left(\frac{B}{A}\right)^2 \\ &\quad -\frac{1}{64}\left(\frac{B}{A}\right)^4 + \mathcal{O}\left(\left(\frac{B}{A}\right)^5\right) \end{aligned} \tag{5.46}$$

The relation between the film thickness and the variational parameter θ is $\sigma = \langle s_i\rangle_{\overline{\mathcal{H}}_{\text{Bog}}} = \theta - d(\theta)$ The equilibrium film thickness is found by determining the θ_o which minimizes the expression for f_{MF} (equation (5.45)) and using this θ_o in the expression $\sigma = \theta - d(\theta)$.

It is not hard to see that y_R is positive at low temperature (large $K = J_1/T$, $L = J_2/T$) but at high temperatures it changes sign. This is because $y_R \approx B/(4A)$ and from equation (5.44) we see that $A > 0$ always but B changes sign. Hence the plaquette theory does display the disordered flat phase. It should also be noted that the substrate potential has been changed from quadratic to a more complicated form in this expansion and that the gradient term $K_R|\nabla s|^2$ is absent in this approximation.

Chapter 6 Conclusions

In this last section we briefly compare the theoretical results we have obtained from the *RSOS* and sine-Gordon models with the results of the experiments on noble gases on graphite substrates [41, 52, 53, 54, 62] and discuss other possible interpretations of the data. We end by discussing work for the future.

6.1 Comparison with experiment

If we accept the premise that the *RSOS* model indeed captures the essential physics of the thin film equilibria, and that the experimental measurements have not missed any significant features in the phase diagram, then it is difficult not to conclude that the reentrant layering is indeed a reflection of the *DOF* phase on the bulk interface. Thus, although Figs. 2.1(h,i), which involve reconstruction, show phase diagrams remarkably similar to Fig. 2.1(d) there are also distinct differences. In Fig. 2.1(h) the experimental vapor pressure isotherms will have steps at the wrong coverages, which seems ruled out by the experimental data. Similarly in Fig. 2.1(i), although the steps in the vapor pressure isotherms now occur at the correct coverages, there is a film analogue of the transition from the rough to reconstructed rough phase at higher temperatures that is not seen in the experiments. This transition is second order, rather than first order, so it might be more difficult to see. Both these scenarios, however, leave open the question of what kind of triangular lattice reconstructed and reconstructed rough phases might replace the square lattice checkerboard phase. Direct probes of the surface structure through scattering measurements would be required to see if, in fact, the upper layer of the film has nontrivial spatial order.

On the other hand, accepting the premise that the *DOF* phase is responsible for the reentrant layering, and the fact that there is not expected to be a reconstructed phase on the triangular lattice, we have seen that the phase boundary between the

flat and DOF phases extends, in principle, to arbitrarily large J_2/J_1. However, the Kosterlitz-Thouless theory tells us that only a finite segment of this boundary can be a continuous transition. The *majority* of this boundary must therefore be first order, and in retrospect it may not be too surprising then that the experimental data show evidence of a first order preroughening transition.

One might be concerned by the fact that the real underlying lattice structure of argon on graphite is FCC rather than triangular. As mentioned in the introduction, this means that although individual layers indeed form two-dimensional triangular lattices, they do not lie directly on top of one another, but are displaced horizontally from one another so that subsequent layers lie in the interstices of the preceding ones. In principle this will affect the quantitative predictions of the RSOS model. This certainly should be checked, but all evidence so far indicates that the results are not particularly sensitive to lattice structure. In the present work we have considered both square and triangular lattices while, for example, the original work of Rommelse and den Nijs was based on a BCC lattice [2, 3].

Another possibility is that a lattice model is simply insufficient for describing the properties of the film. Such would be the case, for example, if two-dimensional melting were to occur. The lattice model cannot describe a phase where incommensurability effects occur, i.e., when the film is in a floating solid phase, with a lattice structure incommensurate with that of the substrate. Such phases indeed occur in very thin films: the data in Fig. 1 of [56] clearly show two dimensional melting lines, as well as triple points where two-dimensional liquid, vapor and solid coexist, in the first two or three layers of argon on graphite. The $RSOS$ model is clearly inadequate if such phases were to persist in the upper layers of arbitrarily thick films.

In a recent letter, Phillips, Zhang and Larese [62] (PZL) take precisely this point of view. They report a Monte Carlo simulation of up to several thousand Lennard-Jones argon atoms on a two-dimensional substrate, with an extent such that about 1000 atoms fill one layer, and studied films up to about three layers thick. They found the usual layering transitions at lower temperatures, and smooth, continuous growth of the film at higher temperatures. However, at intermediate temperatures they found,

as a function of increasing coverage (or, equivalently, increasing chemical potential) at fixed temperature, a sudden increase in the occupation of the fourth layer at the expense of the occupation of the third layer just before third layer completion. This is accompanied by a positional disordering of the third layer, which is interpreted as a melting transition. As more particles are added, the density in the third layer increases again, and at a nominal coverage of about $3\frac{1}{2}$ layers the third layer apparently resolidifies. This resolidification, apparently induced by the hydrostatic pressure of the particles above due to the binding energy of the substrate, is argued to give rise to the steps in the vapor pressure isotherms in the reentrant layering regime. This process is argued to repeat itself layer by layer as the film grows. Since their scenario involves both liquid and solid phases in the film PZL question the use [56] of the RSOS lattice model.

There are various problems with this scenario. First of all, the behavior of the third layer is rather different from that of higher layers, where our DOF phase interpretation is claimed to be valid, and is therefore not a good basis for generalization. Thus, although the first and second layers of argon have independent two-dimensional solid, liquid and gas phases, complete with critical points, triple points and melting transitions, the fourth, fifth and sixth layers behave rather differently. In particular, they do not have triple points or two-dimensional liquid-gas critical points, but they do have low temperature layering transitions at integer layer coverages, and higher temperature "reentrant" layering transitions at half-integer coverages, "zipped" to the low temperature layering transitions by a the zig-zagging line of heat capacity peaks. The third layer, on the other hand, is an intermediate case, showing both types of behavior: there is a two-dimensional triple point and a two-dimensional critical point, but there is also the first reentrant layering transition, marked by coexistence between $2\frac{1}{2}$ and $3\frac{1}{2}$ layers, which entrains the melting of the third layer. It is not surprising, then, that PZL see evidence of melting associated with that rather complicated situation, but the very different nature of the phase diagram for thicker films makes us skeptical of the generalizations they draw from that observation.

There are also two quantitative reasons for doubting the PZL scenario in third

and higher layers. First, if they were due to solidification we would expect the vertical steps in adsorption isotherms that are the signature of the phenomenon to be roughly 10% of a layer in height, the typical density difference between liquids and solids (note, in fact, that for *continuous* two-dimensional melting there is no density difference at all). Instead, all of the data, including PZL's own isotherms, consistently show steps of roughly a full layer. Second, the hydrostatic pressure that is supposed to induce the transition is negligible in the third layer and smaller yet in higher layers. This point shows up clearly in the energetics: the binding energy of the third layer is little more than $k_BT/10$, and decreases as the cube of the film thickness. The canonical ensemble simulation method used by these authors does not allow a direct reconstruction of the isotherms, so no prediction is given for the size of the discontinuous step, nor is any other direct thermodynamic evidence given for this freezing transition. The apparent absence of melting phenomena leads us to believe that the *RSOS* model provides an adequate description of the thicker films in which the physics approaches that of the bulk interface. The *DOF* phase predicted by this model then produces the *full step* reentrant layering transitions (coexistence between $n+\frac{1}{2}$ and $n-\frac{1}{2}$ layers). This, along with the natural explanation of the "zipper" in terms of a first order preroughening transition, demonstrates that the *RSOS* model has remarkable descriptive powers and the agreement of its predictions with the experimental data is striking. Its very simplicity, that is a shortcoming in thinner films, becomes a virtue in thicker films.

6.2 Future work

Given the *RSOS* model parameters J_1 and J_2 the theory developed in the present work then allows reasonable estimates of the renormalized sine-Gordon parameters y and u that determine the actual phase boundaries. Perhaps the largest gap in our theoretical understanding of the reentrant layering phenomenon is the connection between the *microscopic interparticle interactions* and these effective *RSOS* model parameters. If one models the particles, as in [62], using a Lennard-Jones potential with hard core radius σ and attractive minimum depth $-\varepsilon$, the question is whether

there is a reasonably well defined mapping $J_1 = J_1(\sigma, \varepsilon, T)$ and $J_2 = J_2(\sigma, \varepsilon, T)$, and if so what range of J_1 and J_2 the mapping covers for physically motivated ranges of σ and ε. In particular, can the effective J_2 be made small enough to produce continuous preroughening, and do any of the corresponding Lennard-Jones potentials match that of a real material? Answering this question theoretically would require extending the PZL simulations to other Lennard-Jones potentials besides that of argon and to much thicker films.

Another point is that we have seen that the one component $RSOS$ model we study does not produce a θDOF phase. The two component BCSOS model does have a θDOF phase but it there would be considerable experimental difficulty in investigating such a two adsorbate system assuming that one existed. If this phase is, in fact, experimentally realizable for a system with a single adsorbate species (as opposed to "Alloys"–see App. C) then we conclude, at the very least, that something beyond an $RSOS$ model with only first and second neighbor interactions is required. One can therefore ask: What potential would be required in order to generate a θDOF phase in a one component system?

To conclude, recent experiments have shown that there is much new interesting physics to be found in thin film and bulk interface studies. The present work will hopefully motivate future experimental efforts in search of the as yet unseen phases and phase diagrams that we have found.

Appendix A Plaquette mean field theories

In this appendix we outline the general formalism for constructing consistent mean field theories, using plaquettes of arbitrary size, based on any given Hamiltonian. By consistent we mean that the mean field free energy should obey all thermodynamic principles. We guarantee this by demonstrating that the mean field theory becomes exact for a limiting case of a certain model Hamiltonian closely related to the original given one. The formalism we present here is a fairly straightforward generalization of that described in Ref. [63].

The idea is to treat each plaquette as a single site with a set of internal variables, each of which may interact with the internal variables on other plaquettes. If we label the plaquettes by an index P, we denote the *complete set* of internal variables by $\{S_{P\alpha}\}$, $\alpha = 1, \ldots, K$. Often the different plaquettes will be identical copies of one another, but this is not assumed in general. The internal variables will include, for example, not only the height variables h_i within the plaquette P, but also all powers and products of them, h_i^2, h_i^3, $h_i h_j$, $h_i^2 h_j h_k^3$ (with i, j and k all in P), etc. We consider then a rather general reduced Hamiltonian, $\bar{\mathcal{H}} = \mathcal{H}/k_B T$, of the form

$$\bar{\mathcal{H}} = \sum_P \bar{\mathcal{H}}_P\{S_{P\alpha}\} - \sum_{P,\alpha} h_{P\alpha} S_{P\alpha} + \mathcal{A}\{S_{P\alpha}\}, \tag{A.1}$$

where $\bar{\mathcal{H}}_P\{S_{P\alpha}\}$ depends only on the internal variables in plaquette P, and the conjugate fields, $h_{P\alpha}$, should not be confused with the original height variables, h_i. If the plaquettes are identical $\bar{\mathcal{H}}_P$ will not depend on P. The potential $\mathcal{A}$ contains all interactions between different plaquettes. These interactions are forbidden from containing products of the $S_{P\alpha}$ within the same plaquette, P. Technically this means that the derivative $\partial\mathcal{A}/\partial S_{P\alpha}$ is *independent* of $S_{P\beta}$ for all $\beta = 1, \ldots, K$, and hence

that $\mathcal{A}$ is a sum of terms multilinear in the $S_{P\alpha}$. From a practical point of view this means that a term like $(h_i - h_j)^2$ must be multiplied out so that h_i^2 and h_j^2 are included in $\bar{\mathcal{H}}_P$ for their respective plaquettes, while the cross term $h_i h_j$ is included in $\mathcal{A}$ (assuming that i and j lie in different plaquettes, otherwise the entire term belongs in $\bar{\mathcal{H}}_P$). The conjugate fields $h_{P\alpha}$ are introduced in a term separate from $\bar{\mathcal{H}}_P$ and $\mathcal{A}$ for later convenience. The partition function,

$$Z\{h_{P\alpha}\} = \int DS e^{-\bar{\mathcal{H}}\{S_{P\alpha}\}} \tag{A.2}$$

is then a functional integral over some fundamental field S out of which the $S_{P\alpha}$ are constructed. The reduced free energy is $F/k_BT \equiv \bar{F} = -ln(Z)$.

We now introduce independent continuous variables $\sigma_{P\alpha}$ and their conjugate fields $H_{P\alpha}$ as follows: we first use the variables $\sigma_{P\alpha}$ to represent the variables $S_{P\alpha}$ simply by introducing appropriate delta-functions:

$$\begin{aligned} Z\{h_{P\alpha}\} &= \int DS e^{-\sum_P \bar{\mathcal{H}}_P\{S_{P\alpha}\}} \\ \times & \int D\sigma \prod_{P,\alpha} \delta(\sigma_{P\alpha} - S_{P\alpha}) e^{-\mathcal{A}\{\sigma_{P\alpha}\} + \sum_{P,\alpha} h_{P\alpha}\sigma_{P\alpha}}. \end{aligned} \tag{A.3}$$

We then introduce the $H_{P\alpha}$ by using the usual Fourier representation of the delta-function:

$$\delta(\sigma - S) = \int_C \frac{dH}{2\pi i} e^{H(\sigma - S)}, \tag{A.4}$$

where the integral is over a vertical contour C, extending from $c - i\infty$ to $c + i\infty$ in the complex H-plane, where c is an arbitrary real number, which will later be chosen for convenience to satisfy a certain saddle point condition. If we define the single plaquette reduced free energies, Φ_P, via

$$e^{-\Phi_P\{H_\alpha\}} \equiv \int DS e^{-\bar{\mathcal{H}}_P\{S_\alpha\} - \sum_\alpha H_\alpha S_\alpha}, \tag{A.5}$$

then the partition function may be written

$$Z_n\{h_{P\alpha}\} = \int DH \int D\sigma e^{-n\mathcal{F}\{H_{P\alpha},\sigma_{P\alpha};h_{P\alpha}\}} \tag{A.6}$$

where $n = 1$, but for convenience has been introduced as a free parameter, and the free energy functional is

$$\begin{aligned} \mathcal{F}\{H_{P\alpha},\sigma_{P\alpha};h_{P\alpha}\} &\equiv \sum_P \Phi_P\{H_{P\alpha}\} \\ + \sum_{P,\alpha}[\mathcal{A}\{\sigma_{P\alpha}\} &- (H_{P\alpha}+h_{P\alpha})\sigma_{P\alpha}]. \end{aligned} \tag{A.7}$$

We now consider the saddle point approximation, which becomes exact in the limit $n \to \infty$: define the mean field reduced free energy

$$\bar{F}_{MF}\{h_{P\alpha}\} = \mathcal{F}\{H^0_{P\alpha},\sigma^0_{P\alpha};h_{P\alpha}\}, \tag{A.8}$$

where $\{H^0_{P\alpha},\sigma^0_{P\alpha}\}$ satisfy the saddle point equations

$$\begin{aligned} \left(\frac{\partial\mathcal{F}}{\partial H_{P\alpha}}\right)_0 &= 0 \;\Rightarrow\; \sigma^0_{P\alpha} = \left(\frac{\partial\Phi_P}{\partial H_{P\alpha}}\right)_0 \\ \left(\frac{\partial\mathcal{F}}{\partial\sigma_{P\alpha}}\right)_0 &= 0 \;\Rightarrow\; H^0_{P\alpha}+h_{P\alpha} = \left(\frac{\partial\mathcal{A}}{\partial\sigma_{P\alpha}}\right)_0, \end{aligned} \tag{A.9}$$

where the subscript 0 indicates evaluation at the saddle point. Clearly the solutions must be real, and we may specify the number c in (A.4) to be $H^0_{P\alpha}$ for the corresponding contour. We emphasize that because the integration is over complex values of the $H_{P\alpha}$, F_{MF} is *not* in general the minimum of $\mathcal{F}$ over all $H_{P\alpha}$ and $\sigma_{P\alpha}$, not even over all real values of $H_{P\alpha}$ and $\sigma_{P\alpha}$. The direction of steepest descent through the saddle point is often a nontrivial angle in the complex plane. However, if there are multiple saddle points one must obviously choose the one with minimal free energy. We will discuss at the end how to define F_{MF} through a proper extremum principle. The first equation gives the mean field approximation for $-\frac{\partial F}{\partial h_{P\alpha}} = \langle S_{P\alpha}\rangle$ in terms the effective single plaquette free energy, Φ_P, while the second equation gives the effective fields,

$H_{P\alpha}$, acting on plaquette P due to the external field, $h_{P\alpha}$, as well as the mean fields, $\sigma_{P'\alpha'}$, on plaquettes, P', with which it interacts. The latter then serve as inputs to Φ in the first equation. Notice that

$$\begin{aligned} - \quad \frac{\partial \bar{F}_{MF}}{\partial h_{P\alpha}} &= -\frac{\partial \mathcal{F}}{\partial h_{P\alpha}} - \sum_{P'\alpha'} \left[\left(\frac{\partial \mathcal{F}}{\partial H_{P'\alpha'}} \right)_0 \frac{\partial H^0_{P'\alpha'}}{\partial h_{P\alpha}} \right. \\ + \quad & \left. \left(\frac{\partial \mathcal{F}}{\partial \sigma_{P'\alpha'}} \right)_0 \frac{\partial \sigma_{P'\alpha'}}{\partial h_{P\alpha}} \right] = \sigma^0_{P\alpha} \end{aligned} \tag{A.10}$$

where the last equality follows because the saddle point equations cause the second term to vanish identically. This proves consistency, namely that $\sigma_{P\alpha} = \langle S_{P\alpha} \rangle_{MF}$ is indeed the mean field average of $S_{P\alpha}$. Consistency is in fact guaranteed by the deeper result that the limit $n \to \infty$ may be realized as an explicit model [63]: it is straightforward to show that for general integer $n \geq 1$ the partition function, Z_n may be obtained from the Hamiltonian

$$\begin{aligned} \bar{\mathcal{H}}_n &= \sum_{l=1}^{n} \sum_{P} \bar{\mathcal{H}}_P \{ S^{(l)}_{P\alpha} \} - \sum_{P,\alpha} h_{P\alpha} \Sigma_{P\alpha} + n \mathcal{A} \{ \frac{1}{n} \Sigma_{P\alpha} \} \\ \Sigma_{P\alpha} &\equiv \sum_{l=1}^{n} S^{(l)}_{P\alpha}, \end{aligned} \tag{A.11}$$

where $\{S^{(l)}_{P\alpha}\}_{l=1}^{n}$ are n identical copies of the original $\{S_{P\alpha}\}$ with identical single plaquette Hamiltonians, $\bar{\mathcal{H}}_0$, interacting only through their mean values, $\{\frac{1}{n}\Sigma_{P\alpha}\}$, which appear in $\mathcal{A}$. The form (A.6) follows by introducing the Fourier representation of the delta functions $\delta(n\sigma_{P\alpha} - \Sigma_{P\alpha})$ and integrating out the $\{S^{(l)}_{P\alpha}\}$ as before. In the limit $n \to \infty$ the saddle point equations represent an exact solution to this model.

It is worth reemphasizing that the free energy, (A.8), depends only on the fields, $\{h_{P\alpha}\}$. Given only $\bar{F}_{MF}\{h_{P\alpha}\}$ the mean field averages $\{\sigma^0_{P\alpha}\}$ must be obtained through (A.10). It is sometimes preferable to perform a Legendre transformation and work with a free energy that depends explicitly only on the $\{\sigma^0_{P\alpha}\}$. We define then the Helmholtz free energy

$$A_{MF}\{\sigma^0_{P\alpha}\} \equiv \bar{F}_{MF} + \sum_{P,\alpha} h_{P\alpha} \sigma^0_{P\alpha} \tag{A.12}$$

in which (A.10) is used to eliminate the $\{h_{P\alpha}\}$. Equivalently, we have

$$A_{MF}\{\sigma^0_{P\alpha}\} = \sum_P \Phi_P\{H_{P\alpha}\} - \sum_{P,\alpha} H_{P\alpha}\sigma^0_{P\alpha} + \mathcal{A}\{\sigma^0_{P\alpha}\} \tag{A.13}$$

in which the *first line* of (A.9) is used to eliminate the $\{H_{P\alpha}\}$ in favor of the $\{\sigma^0_{P\alpha}\}$. The result is explicitly independent of the $\{h_{P\alpha}\}$, which are then computed from A_{MF} via

$$h_{P\alpha} = \frac{\partial A_{MF}}{\partial \sigma^0_{P\alpha}} \tag{A.14}$$

From (A.13) we see that the computation of A_{MF} from the functional $\mathcal{F}$ given in (A.7) is easier than the computation of $\bar{F}_{MF}$ since it involves solving only one of the saddle point equations, (A.9).

One might be concerned about an obvious ambiguity in the definition of $\bar{\mathcal{H}}_P$. Clearly terms like $\sum_{P,\alpha} h_{P\alpha}S_{P\alpha}$, which are linear in the $S_{P\alpha}$, could also be included in the single plaquette part of the Hamiltonian, therebye changing the form of the single plaquette free energy, Φ_P. Fortunately the saddle point equations are insensitive to this ambiguity [63], which is easily seen only to result in a corresponding shift in the $\{H_{P\alpha}\}$: the sum, $H^0_{P\alpha} + h_{P\alpha}$, is unchanged and from (A.9) one immediately sees that the physical quantities, $\{\sigma_{P\alpha}\}$, are therefore unaffected. Notice from the second line of (A.9) that if $\mathcal{A}$ is independent of a particular $S_{P\alpha}$, then one immediately has the solution $H_{P\alpha} = -h_{P\alpha}$. Therefore unless $S_{P\alpha}$ appears inside a nontrivial interplaquette interaction, one may simply include the term $h_{P\alpha}S_{P\alpha}$ in $\bar{\mathcal{H}}_P$ and set the corresponding $H_{P\alpha}$ to zero. Therefore, the number of free minimization parameters, $\{H_{P\alpha}\}$, that need to be introduced depends only on the complexity of $\mathcal{A}$ and not on that of $\bar{\mathcal{H}}_P$. For example, if interactions in the roughening model take the form $(h_i - h_j)^2$, only fields conjugate to the individual $\{h_i\}$ need be introduced since h_i^2 (as well as h_ih_j for i and j in the same plaquette) appear only in single plaquette terms.

It is worth commenting on the relation between this formalism and the intuitive idea of mean field theory where one makes a distinction between a particular plaquette of variables, S_α, which is treated exactly, and its "environment," which then

interacts with the S_α only through its average properties. In the present formalism these notions are made precise through the distinction between the plaquette free energy, Φ, which contains an explicit trace over the fluctuating internal $S_{P\alpha}$, and the interplaquette interactions, $\mathcal{A}$, which contain only the nonfluctuating $\sigma_{P\alpha}$. Now, in the intuitive picture it is not obvious precisely what aspects of the average environmental behavior are relevant. For example, suppose the fundamental field has spin j, taking values $s_i = -j, -j+1, \ldots, j$ on each site i with corresponding equilibrium probabilities $p_i(s_i)$. In principle all of these $2j$ independent probabilities on each site ought to be determined self consistently in the mean field theory. Equivalently, we may determine the mean powers, $\langle s_i^m \rangle = \sum_{l=-j}^{j} l^m p_i(l)$, $m = 1, \ldots, 2j$ ($m = 1$ corresponding to the order parameter). Within the formalism, however, the powers s_i^m must be contained in the $\{S_{P\alpha}\}$, and their averages contained in the $\{\sigma_{P\alpha}\}$. The consistency of the theory indeed demands that all of these variables (and more if the plaquettes contain more than one site) enter appropriately, though, as we have seen, great simplifications occur for those that do not appear explicitly in the interplaquette interaction term, $\mathcal{A}$.

Finally, in order to define the theory through a true extremum principle, we make the connection to the Bogoliuibov method for constructing mean field theories. The Bogoliubov inequality states that for any two Hamiltonians $\bar{\mathcal{H}}$ and $\bar{\mathcal{H}}_1$, with corresponding reduced free energies $\bar{F}$ and $\bar{F}_1$,

$$\bar{F} \leq \bar{F}_1 + \langle \bar{\mathcal{H}} - \bar{\mathcal{H}}_1 \rangle_1, \tag{A.15}$$

where the average is with respect to $\bar{\mathcal{H}}_1$. The strategy is to pick an appropriate family of exactly soluble model Hamiltonians, $\bar{\mathcal{H}}_1(\lambda)$, depending on a set of free parameters generically denoted by λ. One then defines the Bogoliubov mean field free energy via

$$F_{Bog} = \min_{\lambda} \{ \bar{F}_1(\lambda) + \langle \bar{\mathcal{H}} - \bar{\mathcal{H}}_1(\lambda) \rangle_1 \}. \tag{A.16}$$

Can one connect this procedure to the saddle point method above? The answer is

yes: F_{Bog} is precisely equal to $\bar{F}_{MF}$ with the choice

$$\bar{\mathcal{H}}_1 = \sum_P \mathcal{H}_P\{S_{P\alpha}\} + \sum_{P,\alpha} H_{P\alpha} S_{P\alpha}. \tag{A.17}$$

The minimization is over real values of the $\{H_{P\alpha}\}$. It may seem curious that the $\{\sigma_{P\alpha}\}$ do not appear explicitly anywhere. In fact, the functional being minimized on the right hand side of (A.16) is precisely $\mathcal{F}\{H_{P\alpha}, \sigma_{P\alpha}\{H_{P\alpha}\}; h_{P\alpha}\}$ in which the first line of (A.9) has already been substituted for the dependence of the $\{\sigma_{P\alpha}\}$ on the $\{H_{P\alpha}\}$. This parametric dependence of the $\{\sigma_{P\alpha}\}$ on the $\{H_{P\alpha}\}$ defines a particular trajectory which not only is guaranteed to pass through the saddle point, but for which the saddle point is actually an extremum.

The Bogoliubov procedure often produces an inconsistent free energy. The procedure above is guaranteed not to suffer from this problem. The key ingredient, as we have seen, is that a free minimization parameter, $H_{P\alpha}$, should be introduced for each and every single plaquette variable, $S_{P\alpha}$, that appears in $\mathcal{A}$. This can actually be seen directly within the Bogoliubov procedure: just as $H_{P\alpha}$ in (A.7) vanishes if the corresponding $\sigma_{P\alpha}$ does not appear in $\mathcal{A}\{\sigma_{P\alpha}\}$, it is easy to show that the same is true in (A.17). Thus (A.17) is the most general form of $\bar{\mathcal{H}}_1(\lambda)$ that one need consider.

Appendix B Free energies: interplaquette contribution

Using the formalism developed in App. A, the free energy functional corresponding to the tiling shown in Fig. 3.8 is given by:

$$
\begin{aligned}
& \mathcal{F}^{(6)}\{H_{P\alpha};\sigma_{P\alpha}\} = \sum_{P}\Phi^{(6)}\{H_{P\alpha}\} \\
- \; & \sum_{P\alpha}(H_{P\alpha}+h_{P\alpha})\sigma_{P\alpha} \\
- \; & \lambda_1 K\sum_{P}[\sigma_{P1}(\sigma_{Q_11}+\sigma_{Q_26}+\sigma_{Q_54}) \\
+ \; & \sigma_{P2}(\sigma_{Q_54}+\sigma_{Q_52})+\sigma_{P3}(\sigma_{Q_23}+\sigma_{Q_36}) \\
+ \; & \sigma_{P4}(\sigma_{Q_45}+\sigma_{Q_46}+\sigma_{Q_51}+\sigma_{Q_52})+\sigma_{P5}(\sigma_{Q_44}+\sigma_{Q_45}) \\
+ \; & \sigma_{P6}(\sigma_{Q_23}+\sigma_{Q_21}+\sigma_{Q_44})] \\
- \; & \lambda_2 L\sum_{P}[\sigma_{P1}(\sigma_{Q_13}+\sigma_{Q_23}+\sigma_{Q_52}) \\
+ \; & \sigma_{P2}(\sigma_{Q_26}+\sigma_{Q_45}+\sigma_{Q_51}+\sigma_{Q_55}) \\
+ \; & \sigma_{P3}(\sigma_{Q_11}+\sigma_{Q_25}+\sigma_{Q_21}+\sigma_{Q_44}+\sigma_{Q_54}) \\
+ \; & \sigma_{P4}(\sigma_{Q_44}+\sigma_{Q_43}+\sigma_{Q_53}+\sigma_{Q_54}) \\
+ \; & \sigma_{P5}(\sigma_{Q_23}+\sigma_{Q_42}+\sigma_{Q_46}+\sigma_{Q_52}) \\
+ \; & \sigma_{P6}(\sigma_{Q_26}+\sigma_{Q_22}+\sigma_{Q_36}+\sigma_{Q_45})] \\
- \; & \lambda_1 K\sum_{P}\sigma_{P1}\sigma_{P_46} \\
- \; & \lambda_2 L\sum_{P}(\sigma_{P1}\sigma_{P_14}+\sigma_{P1}\sigma_{P_45}+\sigma_{P2}\sigma_{P_46}) \\
+ \; & (P\rightarrow Q),
\end{aligned}
\tag{B.1}
$$

where we have defined two sublattices, P and Q, for the two different plaquette orientations, and the plaquette labels are shown in Fig. 3.8. The final term, denoted symbolically, is the interaction between plaquettes on the same sublattice, Q, and

takes the same form as the two previous terms. The scale factors, λ_1 and λ_2, have again been introduced. Notice that there is no obvious rotational symmetry to the interactions, and hence that the saddle point values of the $\sigma_{P\alpha}$ will all be different even in the unreconstructed phases.

Similarly, the free energy functional corresponding to the tiling shown in Fig. 4.1 is given by

$$\begin{aligned}
&\mathcal{F}^{(6)}\{H_{P\alpha};\sigma_{P\alpha}\} = \sum_P \Phi^{(6)}\{H_{P\alpha}\} \\
- &\sum_{P\alpha}(H_{P\alpha}+h_{P\alpha})\sigma_{P\alpha} \\
- &\lambda_1 K \sum_P [\sigma_{P1}(\sigma_{Q_24}+\sigma_{Q_36}) + \sigma_{P2}\sigma_{Q_22} + \sigma_{P3}\sigma_{Q_33} \\
+ &\sigma_{P4}(\sigma_{Q_21}+\sigma_{Q_56}) + \sigma_{P5}\sigma_{Q_55} + \sigma_{P6}(\sigma_{Q_31}+\sigma_{Q_54})] \\
- &\alpha_1 \sum_P [\sigma_{P2}(\sigma_{Q_23}+\sigma_{Q_25}+\sigma_{Q_33}+\sigma_{Q_55}) \\
+ &\sigma_{P3}(\sigma_{Q_32}+\sigma_{Q_35}+\sigma_{Q_22}+\sigma_{Q_55}) \\
+ &\sigma_{P5}(\sigma_{Q_52}+\sigma_{Q_53}+\sigma_{Q_22}+\sigma_{Q_33})] \\
- &\alpha_2 \sum_P [\sigma_{P1}(\sigma_{Q_25}+\sigma_{Q_35}) + \sigma_{P2}(\sigma_{Q_36}+\sigma_{Q_56}) \\
+ &\sigma_{P3}(\sigma_{Q_24}+\sigma_{Q_54}) + \sigma_{P4}(\sigma_{Q_23}+\sigma_{Q_53}) \\
+ &\sigma_{P5}(\sigma_{Q_21}+\sigma_{Q_31}) + \sigma_{P6}(\sigma_{Q_32}+\sigma_{Q_52})] \\
- &\beta \sum_P [\sigma_{P1}\sigma_{Q_11} + \sigma_{P4}\sigma_{Q_44} + \sigma_{P6}\sigma_{Q_66}] \\
- &\gamma \sum_P [\sigma_{P1}(\sigma_{Q_22}+\sigma_{Q_33}) + \sigma_{P2}(\sigma_{Q_21}+\sigma_{Q_24}) \\
+ &\sigma_{P3}(\sigma_{Q_31}+\sigma_{Q_36}) + \sigma_{P4}(\sigma_{Q_22}+\sigma_{Q_55}) \\
+ &\sigma_{P5}(\sigma_{Q_54}+\sigma_{Q_56}) + \sigma_{P6}(\sigma_{Q_33}+\sigma_{Q_55}) \\
- &\frac{1}{2}\delta \sum_P [\sigma_{P1}(\sigma_{P_16}+\sigma_{P_24}) + \sigma_{P4}(\sigma_{P_36}+\sigma P_51) \\
+ &\sigma_{P6}(\sigma_{P_44}+\sigma_{P_61})] - \frac{1}{2}\delta(P\to Q)
\end{aligned} \tag{B.2}$$

where the plaquette labels are shown in Fig. 4.1, and where the final term is again the interaction between plaquettes on the same sublattice, Q, and takes the same form as the immediately preceding term. We choose the coefficients α_1, α_2, β, γ,

δ in order to best mimic the interplaquette interactions on the original undistorted lattice. In order to obtain the same overall interaction between each site and the other plaquettes we require $2\lambda_1 K + 2\alpha_2 + \beta + 2\gamma + 2\delta = 4\lambda_1 K + 5\lambda_2 L$ (for the corner sites) and $\lambda_1 K + 4\alpha_1 + 2\alpha_2 + 2\gamma = 2\lambda_1 K + 5\lambda_2 L$ (for the edge sites). This also ensures the correct values of h_2^{in} and h_2^{out} quoted below (3.20). By somewhat arbitrarily matching up the various bonds in Figs. 3.8 and 4.1, we take

$$\alpha_1 = \alpha_2 = \frac{1}{2}\lambda_2 L, \quad \beta = \frac{2}{3}\gamma = \delta = \frac{1}{3}(\lambda_1 K + 2\lambda_2 L). \tag{B.3}$$

Finally specializing to the unreconstructed phases where the σ's take the value M_{out} on the corner sites and M_{in} on the edge sites, we obtain the free energy

$$\begin{aligned}
\tfrac{1}{N} \quad & \mathcal{F}^{(6)}(H_{in}, H_{out}; M_{in}, M_{out}) = \frac{1}{6}\Phi^{(6)}(H_{in}, H_{out}) \\
- \quad & \frac{1}{2}[(H_{out} + h)M_{out} + (H_{in} + h)M_{in}] \\
- \quad & (\lambda_1 K + \frac{1}{2}\beta + \delta)M_{out}^2 - (\frac{1}{2}\lambda_1 K + 2\alpha_1)M_{in}^2 \\
- \quad & 2(\alpha_2 + \gamma)M_{out}M_{in}.
\end{aligned} \tag{B.4}$$

Substituting (B.3) yields the final result, (3.21), on which we base our computations.

The seven site plaquette tiling shown in Fig. 3.9 yields the free energy

$$\begin{aligned}
& \mathcal{F}^{(7)}\{H_{P\alpha}; \sigma_{P\alpha}\} = \sum_P \Phi^{(7)}\{H_{P\alpha}\} \\
- \quad & \sum_{P\alpha}(H_{P\alpha} + h_{P\alpha})\sigma_{P\alpha} \\
- \quad & \frac{1}{2}\lambda_1 K \sum_P [\sigma_{P1}(\sigma_{P_6 5} + \sigma_{P_1 6} + \sigma_{P_1 7}) + (5 \text{ terms}) \\
- \quad & \frac{1}{2}\lambda_2 L \sum_P [\sigma_{P1}(\sigma_{P_6 7} + \sigma_{P_6 2} + \sigma_{P_1 4} + \sigma_{P_2 3}) \\
+ \quad & (5 \text{ terms})] \\
- \quad & \frac{1}{2}\lambda_2 L \sum_P \sigma_{P4}(\sigma_{P_1 7} + \sigma_{P_2 6} + \sigma_{P_3 3} \\
+ \quad & \sigma_{P_4 1} + \sigma_{P_5 2} + \sigma_{P_6 5}),
\end{aligned} \tag{B.5}$$

where the plaquette labels are shown in Fig. 3.9. Similarly, the tiling in Fig. 4.2 yields

$$\begin{aligned}
& \mathcal{F}^{(7)}\{H_{P\alpha};\sigma_{P\alpha}\} = \sum_P \Phi^{(7)}\{H_{P\alpha}\} \\
- \; & \sum_{P\alpha}(H_{P\alpha}+h_{P\alpha})\sigma_{P\alpha} \\
- \; & \frac{1}{2}\lambda_1 K \sum_P [\sigma_{P1}(\sigma_{P_65}+\sigma_{P_16}) + (5 \text{ terms})] \\
- \; & \frac{1}{2}\alpha \sum_P [\sigma_{P1}(\sigma_{P_67}+\sigma_{P_17}) + (5 \text{ terms})] \\
- \; & \frac{1}{2}\beta \sum_P [\sigma_{P1}(\sigma_{P_62}+\sigma_{P_13}+\sigma_{P_23}+\sigma_{P_52}) + (5 \text{ terms})] \\
- \; & \frac{1}{2}\gamma \sum_P [\sigma_{P1}(\sigma_{P_64}+\sigma_{P_14}) + (5 \text{ terms}) \\
+ \; & \sigma_{P4}(\sigma_{P_65}+\sigma_{P_16}+10 \text{ terms})].
\end{aligned} \tag{B.6}$$

In order to best match the overall interactions between a given site and other plaquettes in (B.5) and (B.6) we choose

$$\alpha = \frac{1}{2}(\lambda_1 K + \lambda_2 L), \quad \beta = \gamma = \frac{1}{2}\lambda_2 L. \tag{B.7}$$

Specializing to unreconstructed phases the σ's take the value M_{out} on the outer ring of six sites and the value M_{in} on the central site, we obtain

$$\begin{aligned}
\tfrac{1}{N} \quad & \mathcal{F}^{(7)}(H_{in},H_{out};M_{in},M_{out}) = \frac{1}{7}\Phi^{(7)}(H_{in},H_{out}) \\
- \; & \frac{1}{7}[6(H_{out}+h)M_{out} + (H_{in}+h)M_{in}] \\
- \; & \frac{1}{7}(6\lambda_1 K + 6\alpha + 12\beta)M_{out}^2 - \frac{12}{7}\gamma M_{out}M_{in}.
\end{aligned} \tag{B.8}$$

Substituting (B.7) yields the final result, (3.23), on which we base our computations. In fact, since the tiling in Fig. 3.9 (unlike that in Fig. 3.8) retains the rotational symmetry of the plaquette, one may also simplify (B.5) using M_{out} and M_{in}. The result is in fact *identical* to (3.23), which further supports the choice of parameters, (B.7).

Appendix C The staggered BCSOS and Ashkin-Teller Equivalence

In this appendix we show the equivalence of the staggered BCSOS model (described in section 4.8 of the text) to the Ashkin-Teller model.

We proceed as follows: We have already observed in section 4.8.1 that the staggered BCSOS model is equivalent to a staggered 8-vertex (8V) model. It is now shown that the free energy of the staggered 8V model is invariant under a certain symmetry operation and this fact is used to obtain a more convenient 8V model. We show that this modified 8V model is exactly mappable to a system of interpenetrating Ising spins with four-spin interactions. Finally we show that the isotropic AT model can be mapped onto exactly the same Ising system. Hence the desired equivalence follows, providing us with an explicit solid-on-solid model that contains a θDOF phase, and corresponding intermeshed layering phase diagram.

C.0.1 A symmetry property

Denote the partition function of the staggered 8V model by $Z(a,b,c,d \mid b,a,c,d)$, where the notation is obvious. (a,b,c and d are the boltzmann weights of Fig. 4.8.) Here we show that $Z(a,b,c,d \mid b,a,c,d) = Z(c,d,a,b \mid c,d,b,a)$. To see this we use the fact that the vertices of the 8V model can be thought of as lying on one of two sublattices L_1 and L_2. For a given configuration, on any edge of the lattice reverse the direction of the arrow only if the edge is horizontal (vertical) and there is a site of sublattice L_2 immediately at the right (bottom) of the edge. If the vertices are labeled by v_i, $(i = 1,\ldots,8)$ then under this transformation: $v_1 \leftrightarrow v_5$, $v_2 \leftrightarrow v_6$, $v_3 \leftrightarrow v_7$, and $v_4 \leftrightarrow v_8$ on both sublattices and we have generated a new configuration. The weight of each configuration of the original model can be thought of as the weight of this

resultant configuration in a different 8V model and so have:

$$Z(a', b', c', d' \mid b', a', c', d') \equiv Z(a, b, c, d \mid b, a, c, d) = Z(c, d, a, b \mid c, d, b, a).$$

and the original 8V model can be replaced by the model in Fig. C.1 instead.

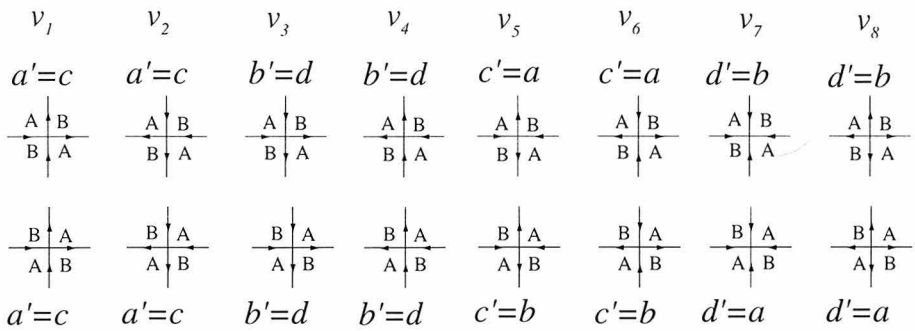

Figure C.1: A modified staggered-8V model equivalent to the original model.

C.0.2 Mapping to an Ising model

An Ising spin model with four-spin interactions is associated with the staggered 8V model introduced above as follows: On each face of this 8V model we place an Ising spin and assume that spin on one special site, S_o, is fixed so that it can only point up. A correspondence between the 8V configurations and the spin configurations is established as follows: If the arrow on an edge points to the right or up (left or down) then the product of the spins on either side of the edge is $+1(-1)$. We see that for each arrow configuration there is a unique spin configuration when we fix one spin. Thus there is a clear correspondence between an Ising spin system where interactions around a vertex (i.e. 4-spin interactions) are allowed and the staggered 8V model. If a Hamiltonian of the form (see Fig. C.2)

$$\mathcal{H} = -P \sum_{\langle ij \rangle \in A} s_{i_A} s_{j_A} - Q \sum_{\langle kl \rangle \in B} s_{k_B} s_{l_B} - R \sum_{V} s_{i_A} s_{j_A} s_{k_B} s_{l_B} \tag{C.1}$$

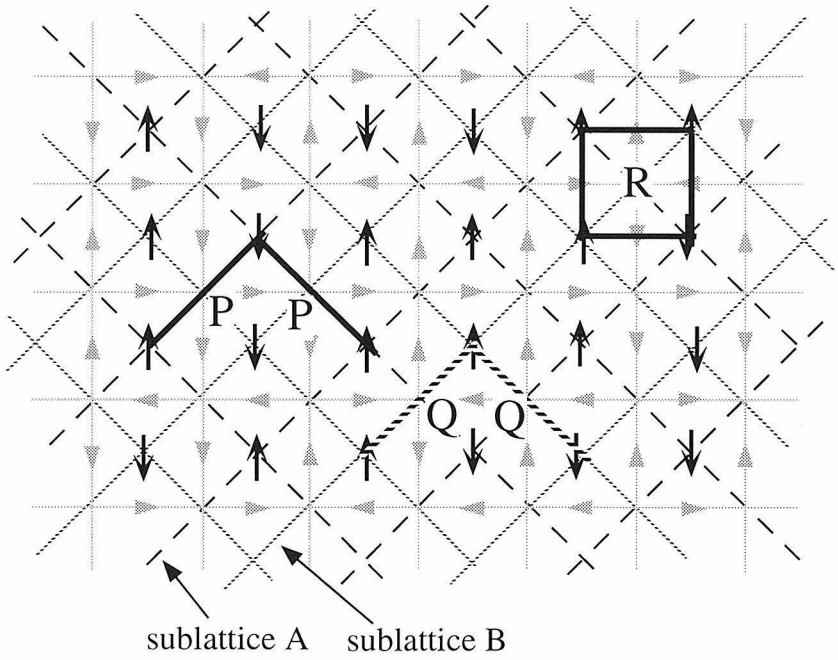

Figure C.2: Four-spin interaction Ising model isomorphic to the staggered 8V model of the preceding section. The vertices of the 8V model are shown in grey. The two spin interactions on the two sublattices are labelled by coupling constants P and Q while the 4-spin interaction is labelled by R in the figure.

is chosen and we take the staggered 8V weights to be

$$\begin{aligned} a' &= \exp(P+Q+R) \\ b' &= \exp(-P-Q+R) \\ c' &= \exp(-P+Q-R) \\ d' &= \exp(Q-P-R) \end{aligned} \tag{C.2}$$

then the spin and staggered 8V Boltzmann weights for a given set of isomorphic configurations is the same. Freeing the constraint on the one special spin we have $Z_{\text{spin}} = 2Z_{\text{staggered 8V}}$. Thus the staggered 8V model is isomorphic to this Ising model.

C.0.3 The Ashkin-Teller Model

In this section the symmetric Ashkin-Teller (AT) model [69] and an equivalent four coupled spin Ising model are described. Together with the mapping of the previous

section this will complete the mapping of the BCSOS model to the AT model.

The AT model is defined on a simple square lattice. On each lattice site i there are two Ising spins s_i and σ_i. Spins on nearest neighbor sites are coupled by two and four spin interactions:

$$\mathcal{H}_{AT} = -\sum_{\langle ij \rangle} (K s_i s_j + K \sigma_i \sigma_j + K_4 s_i s_j \sigma_i \sigma_j). \tag{C.3}$$

This defines the *isotropic* AT model. (More generally the two-spin couplings could have been different for the s and σ spins, but this is not necessary for our purposes.) If a duality transformation is performed on one set of spins (say the σ spins; see [31] for details) then the AT model can be expressed as a system of two interpenetrating square Ising lattices with 4-spin interactions precisely as in the previous section with the same Hamiltonian (C.1). The relation between P, Q and R of (C.1) and K and K_4 of C.3 is:

$$\begin{aligned}
a' &\equiv \exp(P+Q+R) = e^{2K+K_4}(1+e^{-4K})/\sqrt{2} \\
b' &\equiv \exp(-P-Q+R) = 0 \\
c' &\equiv \exp(-P+Q-R) = \sqrt{2}e^{2K+K_4}e^{-2(K+K_4)} \\
d' &\equiv \exp(Q-P-R) = e^{2K+K_4}(1-e^{-4K})/\sqrt{2}
\end{aligned} \tag{C.4}$$

The relation between the boltzman weights of two component BCSOS model and those of the staggered 8V model after use of the symmetry operation were $a' = 1$, $b' = 0$, $c' = \exp(-J_A)$, $d' = \exp(-J_B)$. (J_A and J_B are defined in section 4.8.1.) Using C.4 we find

$$\begin{aligned}
J_A &= 2K_4 + \ln\cosh(2K) \\
J_B &= -\ln\tanh(2K).
\end{aligned} \tag{C.5}$$

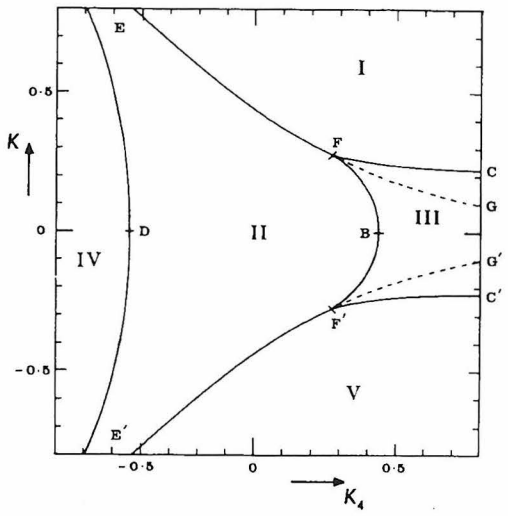

Figure C.3: Isotropic Ashkin-Teller model phase diagram; from R.J. Baxter, *Exactly Solved Models in Statistical Mechanics*, Academic, London (1982). The region around the point F is of particular interest to us. Line EF is a line of continuously varying exponents while FC and FB are Ising lines.

These equations are the main results of this appendix. This completes the mapping of the BCSOS model into the isotropic AT model. The AT model has been studied extensively. Its phase diagram is shown in Fig. C.3. The corresponding BCSOS phase diagram is shown in Fig. 4.11.

Bibliography

[1] J. V. Jose, L. P. Kadanoff, S. Kirkpatrick and D. R. Nelson, Phys. Rev. B **16**, 1217 (1977).

[2] K. Rommelse and M. den Nijs, Phys. Rev. Lett. **59**, 2578 (1987).

[3] M. den Nijs and K. Rommelse, Phys. Rev. B **40**, 4709 (1989).

[4] M. den Nijs, Phys. Rev. Lett. **64**, 435 (1990).

[5] M. den Nijs, in *Phase Transitions in Surface Films 2* (Plenum, N.Y., 1992), H. Taub *et al.* editors.

[6] G. Wulff, Z. Kristallogr. Mineral. **34**, 449 (1901).

[7] C. Rottman and M. Wortis, Phys. Rep. **103**, 59 (1984).

[8] C. Herring, Phys. Rev. **82**, 87 (1951).

[9] E.M. Lifshitz and L.P. Pitaevskii, *Statistical Physics, Part I*, Pergamon, Oxford (1980).

[10] H. van Beijeren, Phys. Rev. Lett. **38**, 993 (1977).

[11] J.D. Weeks and G.H. Gilmer, in: *Advances in Chemical Physics, Vol. XL*, eds. I. Prigogine and S.A. Rice, Wiley, New York (1979).

[12] J.D. Weeks, in: *Orderng in Strongly Interacting Condensed Matter Systems*, ed. T. Riste, Plenum, New York, (1980).

[13] W.K. Burton and N. Cabrera, Disc. Farad. Soc. **5**, 33 (1949).

[14] W.K. Burton, N. Cabrera and F.C. Frank, Phil. Trans. Roy. Soc. **243A**, 299 (1951).

[15] J. Frenkel, J. Phys. U.S.S.R. **9**, 392 (1945).

[16] V.L. Pokrovsky and A.L. Talapov, Phys. Rev. Lett. **42**, 65 (1979).

[17] M. den Nijs, in: *Phase Transitions and Critical Phenomena, Volume 12*, eds. C. Domb, M.S. Green and J.L. Lebowitz.

[18] J. Villain in: *Ordering in Strongly Interacting Condensed Matter systems*, ed. T. Riste, Plenum, New York, (1980).

[19] J.D. Weeks, G.H. Gilmer and H.J. Leamy, Phys. Rev. Lett. **31**, 549 (1973).

[20] H.J. Leamy, G.H. Gilmer and K.A. Jackson in: *Surface Physics of Materials, Volume 1*, Academic Press, New York.

[21] S.T. Chui and J.D. Weeks, Phys. Rev. B **14**, 4978 (1976).

[22] J.M. Kosterlitz and D.J. Thouless, J. Phys. C **6**, 1181 (1973).

[23] J.M. Kosterlitz, J. Phys. C **7**, 1046 (1974).

[24] J.C. Slater, J. Chem. Phys. **9**, 16 (1941).

[25] F. Rys, Helv. Phys. Acta. **36**, 537 (1963).

[26] E.H. Lieb, Phys. Rev. **162**, 162 (1967).

[27] E.H. Lieb, Phys. Rev. Lett. **18**, 1046 (1967).

[28] E.H. Lieb, Phys. Rev. Lett. **19**, 108 (1967).

[29] B. Sutherland, Phys. Rev. Lett. **19**, 103 (1967).

[30] C.P. Yang, Phys. Rev. Lett. **19**, 586 (1967).

[31] R.J. Baxter, *Exactly Solved Models in Statistical Mechanics*, Academic, London (1982).

[32] D.R. Nelson and B.I. Halperin, Phys. Rev. B **19**, 2457 (1979).

[33] A.P. Young, Phys. Rev. B **19**, 1855 (1979).

[34] K.J. Strandburg, Rev. Mod. Phys. **60**, 161 (1988).

[35] J. Villain and M. Gordon, Surf. Sci. **125**, 1 (1983).

[36] V.L. Pokrovsky and A.L. Talapov in: *Soviet Scientific Reviews, Vol. 1*, Academic Press, (1988).

[37] D.A. Huse and M.E. Fisher, Phys. Rev. B **29**, 239 (1984).

[38] P. Bak, Rep. Prog. Phys **45**, 587 (1982).

[39] A. Thomy and X. Duval, J. Chim. Phys. **66**, 1966 (1969).

[40] A. Thomy and X. Duval, J. Chim. Phys. **67**, 286 (1970.)

[41] H. S. Youn and G. B. Hess, Phys. Rev. Lett. **64**, 918 (1990).

[42] H.S. Youn, X.F. Meng and G.B. Hess, Phys. Rev. B **48**, 14556 (1993).

[43] H. Taub et al., Phys. Rev. B **16**, 455 (1978).

[44] C. Tiby and H. Lauter, Surf. Sci. **117**, 277 (1982).

[45] T.T. Chung, Surf. Sci. **87**, 348 (1979).

[46] Y. Larher, Surf. Sci. **87**, 348 (1979).

[47] J.P. McTague, J. Als-Nielsen, J. Bohr and M. Nielsen, Phys. Rev. B **25**, 7765 (1982).

[48] D.M. Butler, J.A. Litzinger, A.J. Stewart and R.B. Griffiths, Phys. Rev. Lett. **42**, 1289 (1979).

[49] E.D. Specht et al., Z. Phys. B, Cond. Matt. **69**, 347 (1987).

[50] R. Pandit, M. Schick and M. Wortis, Phys. Rev. B **26**, 5112 (1982).

[51] R. Hainsey, R. Gangwar, J. Shindler, R. Suter, Phys. Rev. B **44**, 3365 (1991).

[52] P. Day, M. Lysek, M. LaMadrid and D. Goodstein, Phys. Rev. B **47**, 10716 (1993).

[53] P. Day, M. LaMadrid, M. Lysek and D. Goodstein, Phys. Rev. B **47**, 7501 (1993).

[54] P. Day, Ph. D. Thesis (1993).

[55] M. Lysek, M. LaMadrid, P. Day, D. Goodstein, Langmuir **8**, 898 (1992).

[56] P. B. Weichman, P. Day and D. Goodstein, Phys. Rev. Lett. **74**, 418 (1995).

[57] P. B. Weichman and A. Prasad, Phys. Rev. Lett. **76**, 2322, (1996).

[58] W. Weber and D. Goodstein, private communication.

[59] D.M. Zhu and J.G. Dash, Phys. Rev. B **38**, 11673 (1988).

[60] F. Rieutord, R. Simon, R. Conradt and R. Müeller-Buschbaum, Europh. Lett. **37**, 565 (1997).

[61] D. Huse, Phys. Rev. B **30**, 1371 (1984).

[62] J. M. Phillips, Q. M. Zhang and J. Z. Larese, Phys. Rev. Lett. **71**, 2971 (1993).

[63] J. Zinn-Justin, *Quantum Field Theory and Critical Phenomena* (Oxford University Press, 1989), Chap. 21 and App. 21.

[64] H.J.F. Knops and L.W.J. den Ouden, Ann. Phys. **138**, 155 (1982).

[65] H. Knops, Phys. Rev. B **20**, 4760 (1979).

[66] G. Mazzeo,E. Carlon and H. van Beijeren, Phys. Rev. Lett **74**, 1391 (1995)

[67] L.P. Kadanoff and A.C. Brown, Ann. Phys. **121**, 318 (1979).

[68] M. Kohmoto, M. den Nijs and L. P. Kadanoff, Phys. Rev. B **24**, 5229 (1981).

[69] J. Ashkin and E. Teller, Phys. Rev. **64**, 178 (1943).